Advanced Architectures for Inkjet-Printed Organic Photodiodes and Their Integration in Multi-Device Systems

Zur Erlangung des akademischen Grades eines

DOKTORS DER INGENIEURWISSENSCHAFTEN (Dr.-Ing)

von der KIT-Fakultät für

Elektrotechnik und Informationstechnik
des Karlsruher Instituts für Technologie (KIT)

angenommene

DISSERTATION

von

M.Sc. Luis Arturo Ruiz Preciado

Tag der mündlichen Prüfung:	02.07.2024
Hauptreferent:	Prof. Dr. Gerardo Hernandez-Sosa
Korreferent:	Prof. Dr. Martijn Kemerink

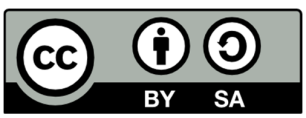

to my family,
for your encouragement and reassurance

to my friends,
for your help and for your presence

to my wife, Andrea,
for your support and for your patience

Abstract

The latest trends in technology based on revolutionary concepts such as the Internet of Things (IoT), Industry 4.0, and personalized medicine describe a level of integration between electronic devices and individuals that is yet to be seen. In this regard, optical sensor technologies, which are currently widely employed in the fields of communication, automotive industry and healthcare, are an essential component of such projected future. In particular, organic photodiodes (OPDs) are a type of organic photodetector that shows great promise for next-generation applications such as IoT and wearable electronics. The organic basis of OPDs enables them to be solution-processed which in turn allows for a fabrication that is expected to be cost-efficient, adaptable to large areas and compatible with light-weight, biocompatible and flexible substrates. Here, the idea is not to replace inorganic-based technologies, but rather to complement their properties in order to achieve a greater number of applications. However, the high-performance achieved in OPDs is still predominately based on laboratory techniques that are non-scalable and lack design flexibility. If OPDs are to be implemented in innovative fields such as IoT and wearable electronics, their development using a more versatile and industrially-relevant fabrication process is needed. Digital printing techniques are suitable for industrial production and capable of structured thin-film formation. Moreover, they offer the key feature of computerized layout design and thus provides the significant advantage of high design flexibility. By addressing the versatility of OPD devices, this thesis enables the integration of OPDs in multi-device systems and facilitates their implementation in next-generation optoelectronic applications. The first analysis presents a novel OPD architecture that features promising advantages such as high processing versatility and mechanical flexibility; and which can be integrated in pre-defined systems. The devices showed state-of-the-art performance, particularly in terms of responsivity with values above 350 mA W^{-1} at -2 V, and in terms of detection speeds with values in the MHz range. Additionally, they demonstrated to be suitable for practical applications such as data transfer receivers in communication systems with a data rate of up to 20 Mb s^{-1}. In a second analysis, the OPDs where integrated with two different matrices of organic thin film transistors (OTFTs) yielding a process capable to integrate stacks of up to 10 functional layers and up to 1024 OPD-OTFT pairs. Finally, the last study presents the development of a new active layer for near-infrared (NIR) OPDs and its adaptation into an inkjet-printed process. The results feature different device architectures for NIR applications including semi-transparent devices with a transmittance above 70% in the visible range that have the potential to enable new designs for health-monitoring devices. Overall, the work presented in this thesis demonstrates that exploiting the advantages of inkjet printing together with ad-

vanced device architectures can enable invaluable features such as fast device prototyping, increased substrate compatibility, and customized designs, allowing to truly harness all the advantages of OPDs and facilitating their integration in next-generation optoelectronic systems for real-life applications.

Kurzfassung

Die neuesten Technologietrends, die auf revolutionären Konzepten wie dem Internet der Dinge (IoT), der Industrie 4.0 und der personalisierten Medizin beruhen, beschreiben ein bisher nicht gekanntes Maß an Integration zwischen elektronischen Geräten und Menschen. In dieser Hinsicht sind optische Sensortechnologien, die derzeit in den Bereichen Kommunikation, Automobilindustrie und Gesundheitswesen weit verbreitet sind, ein wesentlicher Bestandteil einer solchen Zukunftsprojektion. Insbesondere organische Photodioden (OPDs), die eine Art organischer Photodetektoren darstellen, sind für Anwendungen der nächsten Generation wie IoT und tragbare Elektronik sehr vielversprechend. Die organische Basis der OPDs ermöglicht die Verarbeitung auf Lösemittelbasis, was wiederum eine kostengünstige Herstellung ermöglicht, die sich an große Flächen anpassen lässt und mit leichten, biokompatibel und flexiblen Substraten kompatibel ist. Dabei geht es nicht darum, Technologien auf anorganischer Basis zu ersetzen, sondern ihre Eigenschaften zu ergänzen, um eine größere Anzahl von Anwendungen zu erreichen. Derzeit beruhen die mit OPDs erzielten Leistungen jedoch noch überwiegend auf Labortechniken, die nicht skalierbar sind und denen es an Designflexibilität mangelt. Wenn OPDs in innovativen Bereichen wie IoT und tragbarer Elektronik eingesetzt werden sollen, ist ihre Entwicklung unter Verwendung eines vielseitigeren und industrierelevanten Herstellungsverfahrens erforderlich. Digitale Drucktechniken sind für die industrielle Produktion geeignet und in der Lage, strukturierte Dünnschichten zu erzeugen. Darüber hinaus bieten sie das Hauptmerkmal des computergestützten Layoutdesigns und damit den entscheidenden Vorteil einer hohen Designflexibilität. Durch die Berücksichtigung der Vielseitigkeit von OPD-Bauelementen ermöglicht diese Arbeit die Integration von OPDs in Systemen mit mehreren Geräten und erleichtert ihre Implementierung in optoelektronische Anwendungen der nächsten Generation. In der ersten Analyse wird eine neuartige OPD-Architektur vorgestellt, die vielversprechende Vorteile wie eine hohe Verarbeitungsvielfalt und mechanische Flexibilität aufweist und in vordefinierte Systeme integriert werden kann. Die Bauelemente zeigten dem heutigen Stand der Technik entsprechende Leistungen, insbesondere in Bezug auf die Responsivität mit Werten über 350 mA W^{-1} bei -2 V und in Bezug auf die Detektionsgeschwindigkeiten mit Werten im MHz-Bereich. Darüber hinaus erwiesen sie sich als geeignet für praktische Anwendungen wie Datenübertragungsempfänger in Kommunikationssystemen mit einer Datenrate von bis zu 20 Mb s^{-1}. In einer zweiten Analyse wurden die OPDs mit zwei verschiedenen Matrizen aus organischen Dünnschichttransistoren (OTFTs) integriert, was zu einem Prozess

führte, der Schichtsysteme von bis zu 10 funktionalen Schichten und bis zu 1024 OPD-OTFT-Paaren integrieren kann. Schließlich wird in der letzten Studie die Entwicklung einer neuen aktiven Schicht für OPDs im Nahinfrarotbereich (NIR) und ihre Anpassung an ein Tintenstrahldruckverfahren vorgestellt. Die Ergebnisse zeigen verschiedene Bauelementarchitekturen für NIR-Anwendungen, einschließlich halbtransparenter Bauelemente mit einer Transmission von über 70 % im sichtbaren Bereich, die das Potenzial haben, neue Designs für Gesundheitsüberwachungsgeräte zu ermöglichen. Insgesamt zeigt die Arbeit in dieser Dissertation, dass die Nutzung der Vorteile des Tintenstrahldrucks in Verbindung mit fortschrittlichen Bauelementarchitekturen wertvolle Eigenschaften wie schnelles Erstellen von Bauteilprototypen, erhöhte Substratkompatibilität und kundenspezifische Designs ermöglichen kann.

Publications and Conferences

Peer-Reviewed Publications

1. **Luis Arturo Ruiz-Preciado**, Petr Pešek, Carlos Guerra-Yánez, Zabih Ghassemlooy, Stanislav Zvánovec, Gerardo Hernandez-Sosa: *Inkjet-printed high-performance and mechanically flexible organic photodiodes for optical wireless communication.* Sci. Rep. 14, 3296 (2024).

2. **Luis Arturo Ruiz-Preciado**, Sanghoon Baek, Noah Strobel, Kai Xia, Mervin Seiberlich, Sung-min Park, Uli Lemmer, Sungjune Jung, Gerardo Hernandez-Sosa: *Monolithically printed all-organic flexible photosensor active matrix.* npj Flex. Electron. 7, 6 (2023).

3. Mervin Seiberlich, Qiaoshuang Zhang, Ali Veysel Tunc, Kai Xia, **Luis Arturo Ruiz-Preciado**, Stefan Schlisske, Konstantinos Falis, Noah Strobel, Uli Lemmer, Gerardo Hernandez-Sosa: *Inkjet-Printed Microlenses Integrated onto Organic Photodiodes for Highly Accurate Proximity Sensing.* Adv. Sensor Res., 2: 2300004.

4. Aleksandr Perevedentsev, Hadhemi Mejri, **Luis A. Ruiz-Preciado**, Tomasz Marszalek, Uli Lemmer, Paul W. M. Blom, Gerardo Hernandez-Sosa: *Polarization-Sensitive Photodetectors Based on Directionally Oriented Organic Bulk-Heterojunctions.* Adv. Optical Mater. 2022, 10, 2102397.

5. Peter Krebsbach, Stefan Schlisske, Noah Strobel, Mervin Seiberlich, **Luis A. Ruiz-Preciado**, Christian Rainer, Xiaokun Huang, Uli Lemmer, and Gerardo Hernandez-Sosa: *Inkjet-Printed Tin Oxide Hole-Blocking Layers for Organic Photodiodes.* ACS Appl. Electron. Mater. 2021, 3, 11, 4959–4966.

6. Stefan Schlisske, Sebastian Raths, **Luis A. Ruiz-Preciado**, Uli Lemmer, Kai Exner, Gerardo Hernandez-Sosa: *Surface energy patterning for ink-independent process optimization of inkjet-printed electronics.* 2021 Flex. Print. Electron. 6 015002.

7. Ngei Katumo, **Luis Arturo Ruiz-Preciado**, Vinay Kumar, Gerardo Hernandez-Sosa, Bryce S. Richards, Ian A. Howard: Anticounterfeiting Labels with Smartphone-Readable Dynamic Luminescent Patterns Based on Tailored Persistent Lifetimes in $Gd_2O_2S:Eu^{3+}/Ti^{4+}$. Adv. Mater. Technol. 2021, 6, 2100047.

8. Mervin Seiberlich, Noah Strobel, **Luis Arturo Ruiz-Preciado**, Marta Ruscello, Uli Lemmer, Gerardo Hernandez-Sosa: *Aerosol-Jet-Printed Donor-Blocking Layer for Organic Photodiodes.* Adv. Electron. Mater. 2021, 7, 2000811.

Conference Presentations

1. Luis Arturo Ruiz-Preciado, Sanghoon Baek, Noah Strobel, Kai Xia, Mervin Seiberlich, Sung-min Park, Petr Pesek, Carlos Guerra-Yánez, Zabih Ghassemlooy, Stanislav Zvánovec, Uli Lemmer, Sungjune Jung, Gerardo Hernandez-Sosa: *Fully Inkjet Printed Organic Photodiodes for Flexible Electronics: Integration on All-Organic Active-Matrix Arrays and VLC Applications.* ICAE 2023, Jeju, Korea (oral presentation).

2. Luis Arturo Ruiz-Preciado, Sanghoon Baek, Noah Strobel, Youngmin Jo, Jimin Kwon, Mervin Seiberlich, Karl-Philipp Strunk, Sebastian Raths, Sebastian Stehlin, Stefan Schlisske, Peter Erk, Uli Lemmer, Kai Exner, Christian Melzer, Sungjune Jung, Gerardo Hernandez-Sosa. *Integration of High Performance, Fully Printed Organic Photodiodes onto Flexible Arrays of Solution-Processed Organic Thin Film Transistors.* MRS spring meeting 2022, Honolulu, Hawaii, U.S.A. (oral presentation).

Table of Contents

List of Figures

List of Tables

List of Abbreviations

Abbreviation	Meaning
IoT	Internet of Things
OPDs	Organic Photodiodes
OTFTs	Organic Thin Film Transistors
NIR	Near Infrared
NFA	Non-fullerene Acceptor
OSCs	Organic Solar Cells
VLC	Visible Light Communication
OWC	Optical Wireless Communication
PPG	Photoplethysmography
LUMO	Lowest Unoccupied Molecular Orbital
HOMO	Highest Occupied Molecular Orbital
FOM	Figures of Merit
CT	Charge Transfer
I-V	Current-Voltage
J-V	Current Density-Voltage
ITO	Indium Tin Oxide
HBLs	Hole-Blocking Layers
EBLs	Electron-Blocking Layers
PHJs	Planar Heterojunctions
BHJs	Bulk Heterojunctions
LDR	Linear Dynamic Range
SR	Spectral Responsivity
Sn	Spectral Noise Density
D^*	Specific Detectivity
f_{-3dB}	cut-off frequency
λ	Wavelength
V_{TH}	Threshold Voltage
I_{DS}	Drain Current
V_{GS}	Gate Voltage
V_{DS}	Drain Voltage

Abbreviation	Meaning
$\Delta I/I_0$	Relative Change in Current
ΔI	Difference between the values of current in dark and under illumination
I_0	Current in the dark
V_{DD}	Driving Voltage
I_{DD}	Current between the OPDs' anode and the OTFTs' source
V_{diode}	Voltage between anode and cathode of diode
ADC	Analog-to-Digital Converters
FETs	Field Effect Transistors
LEDs	Light Emitting Devices
OLEDs	Organic Light Emitting Diodes
BER	Bit Error Rate
m-CAP	Multi-band Carrierless Amplitude and Phase
rpm	Rotations per Minute
DoD	Drop-on-Demand
dpi	Drops Per Inch
DS	Drop-Spacing
SFE	Surface Free Energies
Re	Reynolds
We	Weber
Oh	Ohnesorge
UV-Vis	Ultraviolet-Visible
PEN	poly(ethylene 2,6-naphthalate)
P3HT	poly(3-hexylthiophene)
SnO_2	Tin Oxide
IDTBR	5,5′-[[4,4,9,9-Tetraoctyl-4,9-dihydro-s-indaceno[1,2-b:5,6-b′]dithiophene-2,7-diyl]bis(2,1,3-benzothiadiazole-7,4-diylmethylidyne)]bis[3-ethyl-2-thioxo-4-thiazolidinone]
BTP-4Cl	2,2′ ((2Z,2′Z) ((12,13 bis(2 ethylhexyl) 3,9 diundecyl 12,13 dihydro [1,2,5]thiadiazolo[3,4 e]thieno[2″,3″:4′,5′]thieno[2′,3′:4,5]pyrrolo[3,2 g]thieno[2′,3′:4,5]thieno[3,2 b]indole 2,10 diyl)bis(methanylyli dene))bis(5,6 dichloro 3 oxo 2,3 dihydro 1H indene 2,1 diyli-dene))dimalononitrile

Abbreviation	Meaning
PEDOT:PSS	poly(3,4-ethylenedioxythiophene) polystyrene sulfonate
ZnO	Zinc Oxide
MoO_3	Molybdenum Oxide
DEG	Diethylene Glycol
DCB	1,2-Dichlorobenzene
CB	Chlorobenzene
DPP-DTT	poly(N-alkyl diketopyrrolopyrrole dithienylthieno-[3,2-b]thiophene)
TPBT	dithienothiophen[3.2b]-pyrrolobenzothiadiazole
PIF8-TAA	polyindenoflurorene-8-triarylamine

1 Introduction

1.1 Motivation

To this day, electronic devices continue to find their way into all types of commercial markets, constantly shaping our society by strongly influencing not only our economy but also our environment and our personal interactions[1]. Yet, in some sense, their integration to our lives has just begun. The latest trends in technology based on revolutionary concepts such as the Internet of Things (IoT), Industry 4.0, and personalized medicine describe a level of integration between electronic devices and individuals that is yet to be seen[1]. In this regard, sensor technologies are an essential component in the achievement of such technological developments. Optical sensors in particular, are currently widely employed in many important fields, including communication systems, healthcare, automotive industry and security[2,3]. At the same time, scientific advances such as virtual and augmented reality, artificial intelligence, wearable electronics and the ever-growing use and exchange of data, further point in the direction of a stronger integration of optical sensors in society[1]. For example, in their industry report for optical sensors with the forecast period of 2024-2030, Grand View Research estimates an optical sensor market size of 25 billion USD in 2023 with a revenue forecast of 54.83 billion USD in 2030[4]. On the other hand, the integration of optical sensors to innovative systems such as those envisioned in IoT applications is not straightforward. The requirements for a successful integration puts strong demands on the performance, costs, fabrication methods and physical characteristics of the devices[1]. While standard semiconductor technologies based on inorganic materials are accurate detectors and reliable devices, they often suffer disadvantages in terms of their costs, fabrication complexity and mechanical characteristics such as lack of flexibility[5]. A possible solution lies in organic semiconductors which show characteristics that are particularly suitable for those scenarios[5–8]. One important distinction of organic materials is that they can be solution-processed. This allows for a fabrication that is not only expected to be cost-efficient, but that also facilitates their deposition in larger areas, is adaptable to pre-fabricated systems and is compatible with stretchable, light-weight, bio-compatible and flexible substrates[5,9]. The idea is not to replace inorganic-based technologies, but rather to complement their properties in order to achieve a greater number of applications, covering existing, as well as new device-functions. In this re-

spect, organic photodiodes (OPDs) are a type of organic photodetector that has shown great promise in device performance in recent years and due to their valuable characteristics such as color-selectivity, low-cost and flexibility[10–16] they are also promising candidates for different commercial products such as compact spectrometers, biometric sensors, and flexible image sensors[17–20]. However, on the majority of cases, their achieved high-performance is still based on non-scalable fabrication techniques that also lack design flexibility, like e.g. lab-scale techniques such as spin-coating deposition[6,21]. Other coating techniques such as blade coating and spray coating offer a good compatibility with industrial settings and show valuable advantages such as low complexity and high reproducibility, however, they are incapable of a structured deposition of materials and therefore they remain limited in their applicability in customized systems and fast prototyping[21]. If OPDs are to be implemented in innovative fields such as IoT and wearable electronics, their development and the achievement of high performance using a more versatile and industrially-relevant fabrication process is needed. In this regard, printing techniques are solution-processed fabrication methods suitable for industrial production that are capable of structured thin-film formation, with reproducible feature sizes typically in the range of 10 to 100 µm[21]. Furthermore, a subset of printing techniques known as digital printing offers the key feature of computerized layout design and thus provides the significant and much needed advantage of high design flexibility and fast prototyping[13,21]. Among the possible options, inkjet printing represents one of the most promising and established technologies with several literature reports demonstrating its applicability for organic electronics[22–31]. Moreover, in a direct comparison with the other industrially-relevant coating and printing techniques, inkjet printing has been found to be among the most applied methods in the development of OPD layers, particularly for active layers and electrode materials[13,18,21,32–45]. Overall, a well-established process development for high-performing OPDs by inkjet printing would allow to truly harness all the advantages of OPDs and facilitate their integration in next-generation optoelectronic systems. The motivation of this thesis is therefore the possibility to contribute to the achievement of this projected future.

1.2 State-of-the-art

In recent years the focus of OPD development has been mainly oriented towards the topics of: narrow band OPDs[11,17,46,47], the development of new photo-active materials[48–50], large area image sensors[11,51], the use of different coating and printing techniques[6,21] as well as the understanding of charge-trapping effects in OPDs and practical techniques for dark current suppression[52,53]. As a result, OPDs have seen great progress in terms of their device performance with their improvement being notably marked by extensive reports of OPDs showing characteristics such as responsivity, linear dynamic range and detection speed being on-par with those of commercially available inorganic photodetectors [32–35,54,55]. Examples of those reports demonstrate values of 440 mA W^{-1} in terms of responsivity, and 180 dB in linear dynamic range[54,55]. At the same time, OPDs seem to still lack behind in terms of their detectivity, particularly when it comes to narrow bandgaps, due to their reduced charge generation and increased recombination[52]. Thus, the understanding of such device physics are currently active research topics[52,53,56]. In terms of new functionalities, the intrinsic advantages of OPDs, which allow for improved designs and applications, have already proved to be more favorable alternatives for certain scenarios. For example, the complex design requirements needed in inorganic devices in order to implement optical filters is effectively eliminated in OPDs, since they can be tailored for specific wavelength detection[17]. Despite the remarkable progress, some problems still need to be addressed in greater depth. Examples include the need for an increased number of photo-active materials,[17] understanding of the intrinsic limits of device operation[17,52,53,57,58], the integration of OPDs with organic transistors[17,51,59], OPDs with higher detection speeds[17], high-performing OPDs with spectral responses in the NIR and IR[17,48–50], and the development of materials and devices based on industrially-relevant, scalable and adaptable fabrication methods[6,21,59]. Besides these major topics, other areas of interests include OPDs in flexible substrates as well as bio-compatible and biodegradable components[17,48–50], long-term device stability[17,48–50], and innovative OPD designs, applications and architectures[13,32,48,60].

In particular, this thesis addresses those areas of interests related to the versatility of OPD devices. It does so by targeting different challenges of OPD development, such as, OPD processing based on industrially-relevant techniques, innovative device designs, the integration of OPDs with organic transistors, the use of substrates with mechanical flexibility, the transparency of the devices, and the development of new systems for NIR detection.

Moreover, the work presented in this thesis specifically incorporates the use of non-fullerene acceptor (NFA) materials, which, fueled by its introduction in the field of organic solar cells (OSCs)[61–63] continue to show some of the most promising results for OPD development in terms both figures of merit as well as increased device stability[34,49,64–66]. Additionally, during the complete thesis, the focus is in the use of the versatile and industrially-relevant inkjet printing deposition technique with the aim of optimizing the design flexibility and potential application of the OPD devices while maintaining a high device performance.

1.3 Structure of the Thesis

The introduction presented here as Chapter 1, aims to provide the reader with the motivation behind this thesis, with the research focus, trends, state-of-the-art as well as remaining challenges in the topic of OPD devices, and finally, with the topics and challenges which this thesis aims to address. Then in Chapter 2, the fundamental background understanding of the organic semiconductor devices employed in this thesis as well as the working principle of potential applications that were tested, are presented. Similarly, Chapter 3 presents the working principle of the different techniques employed to deposit the materials and fabricate the devices presented in this thesis. Chapter 4 presents the background knowledge of the different characterization methods that were employed to evaluate the materials and devices presented in this thesis. In order to address the characterization procedures for different types of samples the methods are divided into the characterization of substrates and functional inks, thin-film characterization, and device characterization. The main results of this thesis start in Chapter 5, where a novel fully inkjet-printed OPD stack that is able to conform to varied and complex surfaces and which can be integrated in pre-defined systems, is presented. At the same time, the focus is to maintain a high-performance, therefore the devices are compared to similar devices that are either spin-coated or partially printed. Finally, the developed OPDs are applied as receivers in a visible light communication (VLC) system to test their potential in systems employing wireless data exchange. In Chapter 6, the challenge of integrating OPDs with other electronic devices is addressed. In specific, inkjet printing is applied to monolithically integrate the OPDs with two different technologies of organic thin film transistor devices to form all-organic photo sensor matrices in thin and flexible substrates. In Chapter 7, a novel material system in terms of a new donor-acceptor combination is studied with the goal to

apply it as active layer in OPDs with NIR response. Additionally, the material is tested in different OPD architectures including fully-transparent stacks. Finally, Chapter 8 provides a summary and a conclusion of the results presented in this thesis, with a discussion about the different challenges addressed and an outlook for the future.

2 Fundamentals of Organic Semiconductor Devices and Selected Applications

This chapter presents the fundamental background knowledge behind the devices presented in this thesis, including a general introduction to organic semiconductors, the basic principles and metrics of the different types of organic devices developed as well as a selected group of potential applications where the devices have been tested. The principles presented here are well described in the literature. Therefore, the readers can expand their knowledge further by consulting the sources provided in the different sections, including the following books[67–70]*.*

2.1 Organic Semiconductors

Organic semiconductors are materials with electrical characteristics resembling those of conventional semiconductors. They are referred to as organic because of their organic, carbon-based chemistry. Thanks to their organic nature they also possess certain characteristics that are not available to conventional semiconductors such as mechanical flexibility and low weight, or increased absorption coefficients and an easier achievement of narrowband performances via low-complexity material synthesis[17]. Moreover, of special interest for this work is their distinct chemical processing that allows for different deposition techniques and processing parameters based on their solution-processability. However, not everything is advantageous in organic semiconductors, given that their material properties tend to be remarkably different from inorganic semiconductors. For instance, the charge carrier mobility and diffusion length can be important limiting factors in organic devices[71]. Therefore, devices based on organic semiconductors need to be engineered taking into consideration all the advantages and disadvantages of organic semiconductor materials in order to obtain a relevant and valuable output.

2.1.1 The Hybridization of Carbon Atoms and the Concept of Conjugated Molecules

In order to understand how organic materials can be semiconductors, it is necessary to understand the bonding of carbon atoms and the concept of conjugated molecules. In general, the science of quantum mechanics describes the properties of molecules and atoms as well as their interactions. As part of its description, it defines the electron distributions in atoms. **Figure 2.1a** shows the electronic distribution of carbon at ground state. This corresponds to two electrons in 1s, two electrons in 2s, one electron in $2p_x$, and one electron in $2p_y$, leaving $2p_z$ free (**Figure 2.1b** top). This electronic distribution allows carbon to form a maximum of two covalent bonds. However, when describing complex systems, such as molecules, the concept of hybridization is also employed, and in the case of carbon, this means that by re-locating one electron from 2s into $2p_z$ in order to be able to form a maximum of four covalent bonds instead of two, then a more energetically favorable state can be achieved[67].

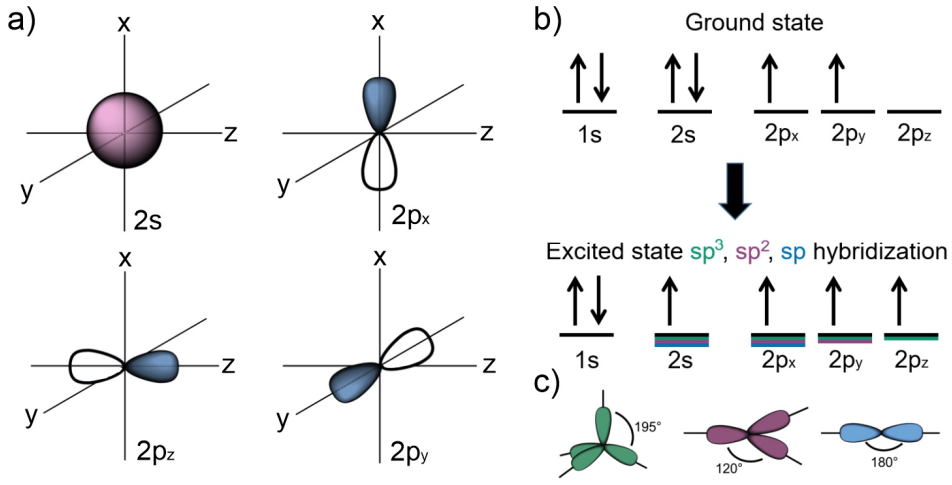

Figure 2.1 Electronic Distributions of Carbon at Ground State and at Different Hybridizations.
a) Schematics of the electronic distributions of carbon in the s and p atomic orbitals. b) Electron configuration of carbon in the ground state (top) and in excited state for the different types of hybridization (bottom). c) Schematics of the hybrid orbitals sp^3, sp^2 and sp. Schematics based on[67].

As seen in **Figure 2.1b** bottom, carbon can present three different types of hybridization, sp^3 hybridization, sp^2 hybridization, and sp hybridization for the cases where there is a

combination between four, three and two orbitals, respectively. Finally, **Figure 2.1c** shows an schematic of the orbitals resulting from the 2s and 2p combination which are known as hybrid orbitals[67]. Such hybridized atoms can then merge with other atoms, whereas also hybridized or not, to form new molecules. When this happens, the electrons being shared between the different atoms are now part of so-called molecular orbitals instead of atomic orbitals, because the probability of the electron location being at a given atom is the same. When there is a constructive or in-phase interaction, two types of molecular orbitals can be distinguished, σ- and π-orbitals. On the other hand, when the interaction is destructive or out-of-phase, the states are known as σ*- and π*-antibonding orbitals[67]. **Figure 2.2a** shows the schematic representation of σ- and π-orbitals. In the case of a σ-orbital, there is a constructive interaction between two p_z orbitals whereas in the case of the π-orbital the interaction occurs between two p_x orbitals. The corresponding bonds are known as σ-bond and π-bond. As seen in the schematic, σ-bonds are in line with the molecular plane and π-bonds are projected out of the plane.

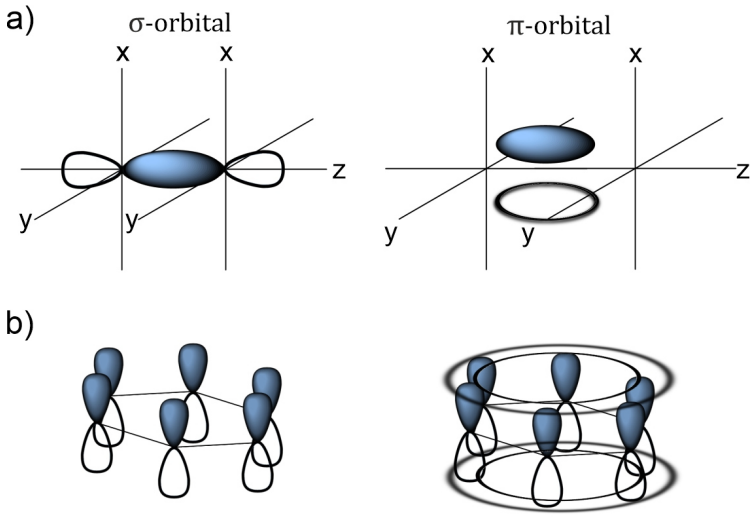

Figure 2.2 Molecular Orbitals and Benzene.
a) Schematics of the σ and π molecular orbitals. b). Schematic of a benzene molecule illustrating the de-localization of electrons. Schematic in panel a) based on[67]. Schematic on panel b) based on[68].

In terms of the electronic properties of the molecules, electrons in π-bonds are considered to be de-localized and free to move, contrary to σ-bonds which are considered to be strong bonds. Molecules that present this phenomenon are known as conjugated molecules and are typically recognized by the alternation of multiple single and double bonds that alter-

nate between each other[68]. A classic example is benzene, which has 6 p-orbitals as illustrated in **Figure 2.2b**. In this case the electrons are considered to be de-localized over the 6 carbon atoms[68]. Finally, the energy levels of conjugated molecules will depend on the size of the molecule where longer molecules will have an increased delocalization and lead to smaller bandgaps[67]. Based on this, the tuning of the molecular structure can allow a tuning of the wavelength of light being absorbed in order to be applied for example, into optoelectronic devices.

2.1.2 Energy Levels and Charge Carrier Transport

Based on the concepts of molecular orbitals presented in the previous section, the energy levels of organic semiconductors can become clear. The stacking and interaction of several molecules will eventually lead to a broadening of energy states that results in so-called energy bands[68]. In organic semiconductors, the main energy levels describing their optoelectronic properties are the lowest unoccupied molecular orbital (LUMO), corresponding to the conduction band in their inorganic counterparts, and the highest occupied molecular orbital (HOMO), corresponding to the valence band in their inorganic counterparts[68]. **Figure 2.3a** shows a schematic representation of the LUMO and HOMO levels which are also represented by π*- and π-orbitals, respectively.

In terms of their interaction with light, organic semiconductors can undergo multiple processes[68]. Based on the focus of this thesis, the explanation of such basic principles will be focused on organic devices and in particular to OPD devices. The corresponding discussion can be found in Section 2.2. In terms of their charge carrier transport, just as in inorganic materials, the charge carriers correspond to electrons and holes[68]. However, due to the low dielectric constant of organic materials, electrons and holes tend to be linked by electrostatic forces into a bound state known as exciton[71]. This binding is strong and therefore in order to dissociate it back into electrons and holes, an energy with typical values in the meV, and thus much larger than the one found in inorganic materials, is needed[71]. Moreover, most organic semiconductors show a mechanism known as hopping mechanism consisting of movement of charges from one localized energy state to another and caused by the weak interactions among the molecules that form the system[68]. **Figure**

2.3b shows a schematic of charge hopping. In this case, a carrier overcomes the potential energy required to move into empty and neighboring energy states.

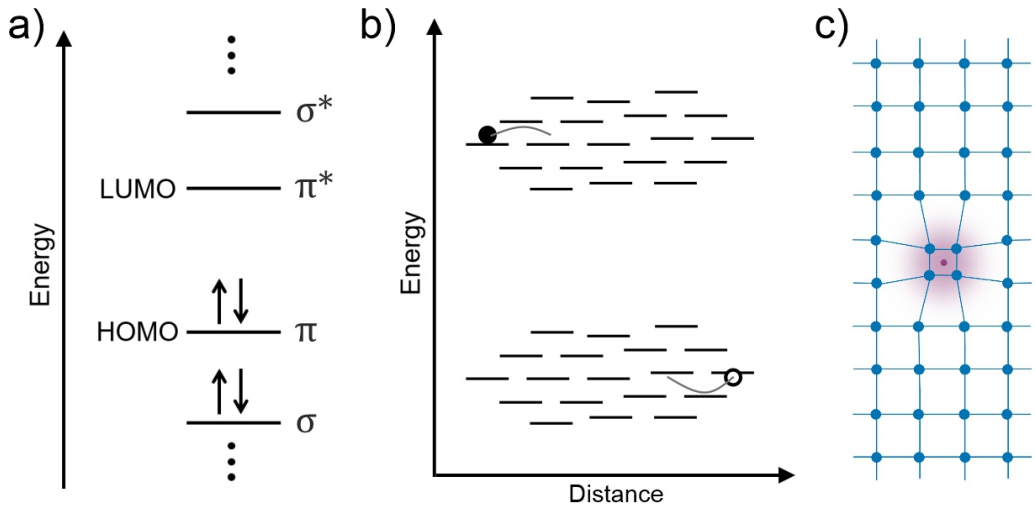

Figure 2.3 HOMO-LUMO Levels, Hopping Mechanism and Polaron Formation.
a) Schematic representation of the HOMO and LUMO levels of organic semiconductors. b) Schematic representation of the hopping mechanism in organic semiconductors. c) Schematic representation of the formation of a polaron state. Schematic panel a) based on[67], Schematics panel b) and c) based on[68].

Besides this, the weak interactions among molecules can also lead to a phenomenon known as polaron, as depicted in **Figure 2.3c**, on which a charge carrier and the surrounding chargers interact resulting in a deformation of the lattice. Both polaron effects and hoping mechanisms can influence the charge carrier transport in organic semiconductors and limit their performance in comparison to inorganic semiconductors.

2.2 Organic Photodiodes

This section aims to provide the reader with the essential background knowledge in the working principles of OPDs. In the following, the components, device architecture and principles of operation of OPDs are presented. It is worth noting that the basic structures and physical principles of OPDs are very similar to those of solar cells. However, their respective functions as optical sensor and power generator lead to important differences in device operation as well as in the optimization of their device architecture. Additionally, their different intended functionalities also lead to a difference in their relevant figures of merit (FOM).

2.2.1 Basic Structure and Working Principle

OPDs are a class of organic-based optical sensor on which the basic structure consists of a so-called active layer material deposited between two electrodes. The active layer is composed by two different semiconductor materials known as electron donor and acceptor. Based on this, the working principle of an OPD that leads to the conversion of absorbed light into an electrical signal is depicted in **Figure 2.4a**. It consists of the absorption of photons with an adequate energy that leads to the generation of excitons at the active layer, is followed by the dissociation of charge transfer (CT) excitons at the interfaces of the donor and acceptor materials into electrons and holes, to be finally collected at the electrodes leading to a current-voltage (I-V) response[71].

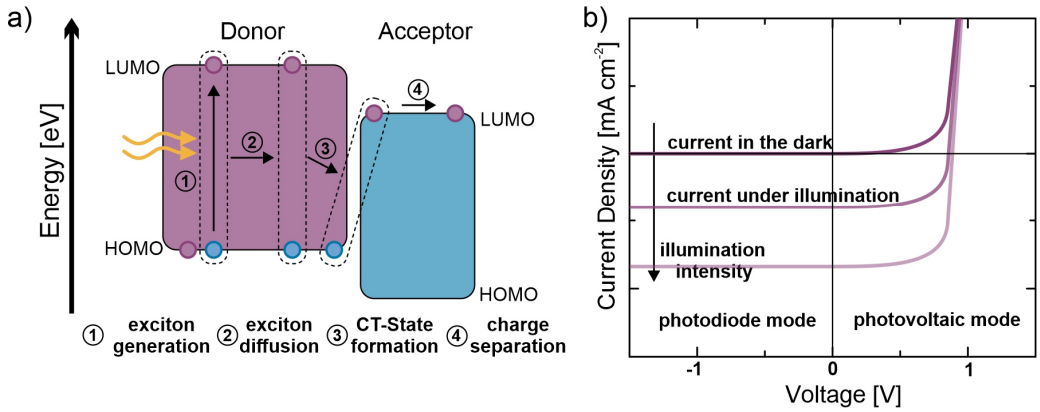

Figure 2.4 Working Principle and IV Characteristics of OPDs.
a) Schematic of the working principle of an OPD from exciton generation to charge separation. b) Exemplary schematic of the I-V characteristics of an OPD showing the contrast between currents in the dark and under different illuminations of increasing intensity as well as the different modes of operation. Figure adapted from[72], CC-BY.

The characteristic I-V response of an OPD is depicted in **Figure 2.4b**. As it can be observed, the current increases with the illumination intensity. Moreover, in contrast to OSCs, OPDs are typically operated in the reverse bias. This allows for a more efficient carrier extraction, reduces the response time and yields an enhanced functionality for signal detection[71,72]. Nevertheless, OPDs can also be operated at a bias equal to 0 V, for example in order to operate with a lower dark current which in non-ideal diodes tends to increase at higher reverse bias[71]. Finally, **Figure 2.5** shows a schematic of a photodiode equivalent circuit. The electronic operation of an OPD is better understood by employing such equivalent circuit model. In this case, the circuit is formed by an ideal diode that

represents the diode behavior, a capacitance *C* that dictates the frequency response of the diode, and a current source that represents the illumination-based current and thus defines the photocurrent. Moreover, it contains two resistances, the parallel resistance R_{shunt} and the series resistance R_{series}. R_{shunt} must be large to avoid current to flow through the device and R_{series} must be low in order to avoid a limited output current.[71–73].

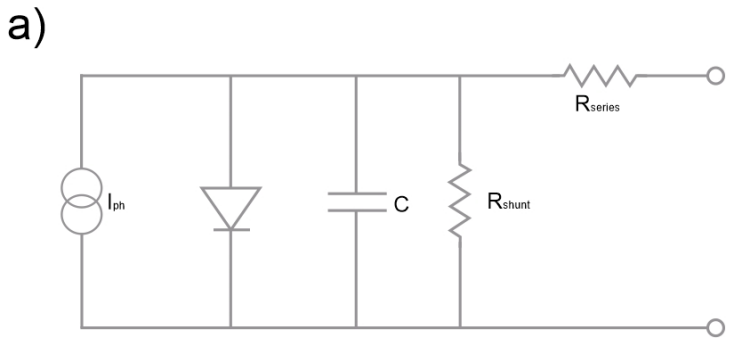

Figure 2.5 Photodiode Equivalent Circuit.
a) Photodiode equivalent circuit. The electronic operation of an OPD is better understood by employing such equivalent circuit model. Figure based on[71,72].

2.2.2 Improved Device Architecture and its Constituents

Currently, a typical device architecture of an OPD tends to be more elaborate than the basic electrode/active layer/electrode structure. This can be observed in **Figure 2.6** which shows a schematic of a typical OPD device architecture. In general, the type of OPD architecture is referred to as normal architecture when the cathode is located at the top, or as inverted architecture when the cathode is located in the bottom.[16,74]. Moreover, there are also different types of active layer technologies that can be implemented into OPDs. In the following, a more detailed explanation of the constituents of an OPD stack as well as their intended functions are presented.

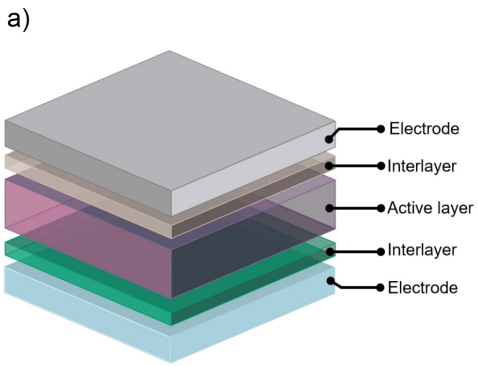

Figure 2.6 Exemplary Schematic of an OPD Device Architecture.
a) A typical device architecture of an OPD tends to be more elaborate than the basic electrode/active layer/electrode structure containing complementary materials such as interlayers. Figure adapted from[32], CC-BY.

2.2.2.1 Electrode and Interlayer Materials

This subsection discusses the function of the electrodes and interlayer components of a typical OPD architecture. The role of the electrodes within an OPD architecture is straightforward, they are used to collect the generated charge carriers. Therefore, effective electrodes should have a high conductivity where common materials are metals such as silver, aluminum and gold. Additionally, since light must reach the active layer, one of the electrodes must also be transparent. In this case, common options are indium tin oxide (ITO), and metals deposited in layers of ultrathin thickness in the range of a few nm. Moreover, when an OPD is operated in reverse bias, charge carrier injection from the electrodes occur leading to an increase in the dark current of the device which in turns lowers the capacity of the device to detect a signal[75]. Based on this, the function of the interlayers is to improve the device performance by blocking the injection of those charge carries. This is depicted in **Figure 2.7**. As it can be appreciated, the interlayers act as energy barriers that block charge carriers coming from the electrodes[75]. If these hole blocking layers (HBLs) and electron blocking layers (EBLs) were not used, or if they were inefficient for example due to an energy mismatch, then the injected carriers could interact with other charge carriers leading to recombination and lowering the device performance.

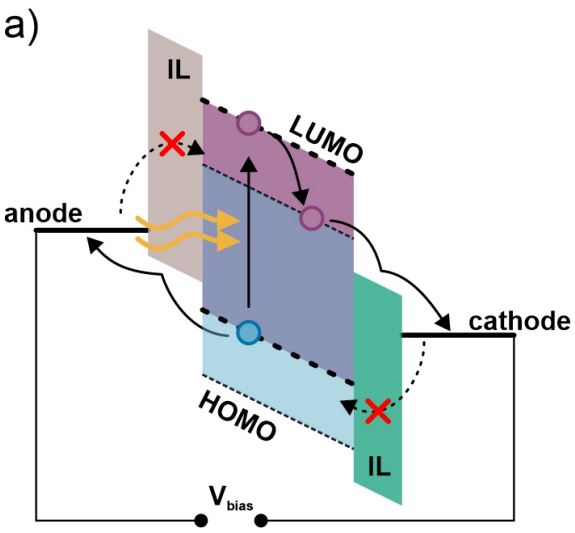

Figure 2.7 Working Principle of Charge Blocking Interlayers in OPDs.
a) Interlayers in OPDs improve the device performance by blocking the injection of charge carries from the electrodes. Figure adapted from[72], CC-BY.

2.2.2.2 Bulk Heterojunction Active Layers

This subsection discusses two different types of active layer concepts that are possible in OPD devices. The performance of an OPD is strongly influenced by the choice of materials and architecture employed. In this regard, one of the most relevant differences depends on the type of active layer employed. **Figure 2.8** shows a schematic of two different active layer structures. In active layers with planar heterojunctions (PHJs) (**Figure 2.8a**), the donor and acceptor materials are deposited individually one over the other. On the other hand, in bulk heterojunctions (BHJs) (**Figure 2.8b**), the donor and acceptor materials are blended together and deposited as a single layer.

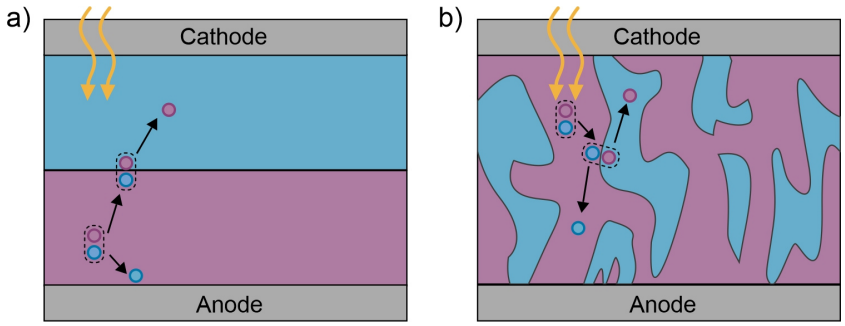

Figure 2.8 Planar- and Bulk-Heterojunctions for OPDs.
a) Schematic of a planar heterojunction. b) Schematic of a bulk heterojunction. In BHJs the probability of an exciton reaching an interface is higher due to the shorter distances. Figure adapted from[72], CC-BY.

Since excitons, which have a small diffusion length, need to reach the donor-acceptor interface in order to dissociate, the distance that they travel before reaching an interface becomes very important[71]. Therefore, an active layer using a PHJ tends to be limited. On the other hand, the intermixing of the donor and acceptor materials in BHJs shortens the distance that excitons need to travel before dissociation while maintaining an efficient photon absorption[17]. For this reason, BHJs are the dominant active layer concept employed and are also the type of active layer used in this thesis.

2.2.3 Figures of Merit

This section presents the fundamental background knowledge for the main performance metrics of OPD devices. The different FOM of OPDs allow a direct and quantified comparison between different OPD devices. In the frame of this work, this includes not only a comparison between the different OPD devices developed in this thesis, but also their comparison to the performance of other OPD devices reported in the literature. Additionally, the understanding of the different metrics also allows to assess the different possible applications of a given device. As mentioned before, the basic structures and physical principles of OPDs are very similar to those OSCs. However, their intended functionalities lead to important differences in device operation as well as in the optimization of their device architecture. Similarly, when comparing different OPD devices, their strengths and weaknesses in terms of their FOMs can lead to different intended functionalities. In other words, depending on the desired OPD application, different OPD characteristics are more relevant than others.

2.2.3.1 Static Characteristics

This subsection presents the static characteristics of OPDs. **Figure 2.9** depicts schematic examples of the J-V characteristics, linear dynamic range (LDR), and spectral responsivity (SR) of OPDs. In the following, their theoretical basis and calculations are introduced.

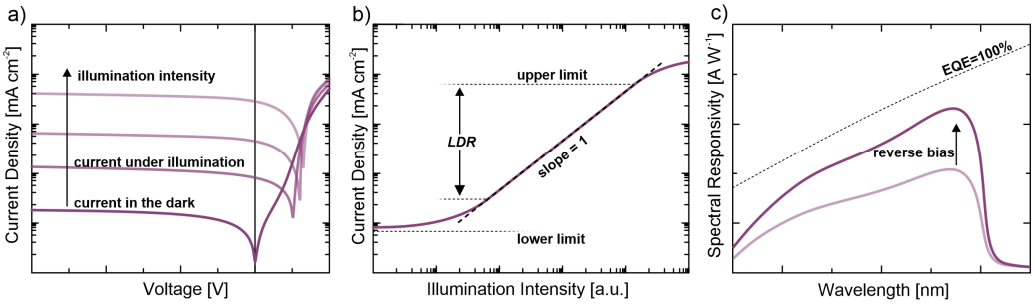

Figure 2.9 Schematics of the Static Characteristics of OPDs.
a) Exemplary schematic of the J-V characteristics of an OPD showing the contrast between currents in the dark and under different illuminations of increasing intensity. b) Exemplary schematic of the linear dynamic range of an OPD showing the methodology for its determination. c) Exemplary schematic of the spectral responsivity of an OPD showing the contrast between responsivities under different bias voltages. The responsivity for an EQE= 100% is represented by the dotted line. Figure adapted from[21], CC-BY.

2.2.3.1.1 I-V Characteristics and Linear Dynamic Range

During the analysis of OPD devices, it is common practice to look at the I-V characteristics with the current being plotted in a logarithmic scale as depicted in **Figure 2.9a**. As it can be observed, this representation allows a more accurate distinction of the device behavior in the reverse bias. Moreover, when seeking to obtain a reliable detection of light that can be implemented in different applications, the OPD photo-response over a wide range of light intensities becomes relevant. The LDR defines the range of light intensities at which the photo-response remains linearly proportional to the intensity of the incident light[21,76]. It is defined by equation 2-1.

$$LDR = 20 \times log \frac{i_{max}}{i_{min}} \qquad 2\text{-}1$$

where i_{max} and i_{min} are the upper and lower current values where a deviation from linearity occurs. The factor 20 takes into account the relation of proportionality between power (P)

and current as given by $P \sim i^2$[21]. **Figure 2.9b** shows a schematic representation of the LDR of a photodetector. As it can be seen, the LDR is plotted in a double logarithmic plot with a linear function with slope of 1. Deviation from the slope of 1 determines the limits of the LDR. At the upper limit the LDR is constrained by recombination phenomena, particularly, by so-called bimolecular recombination due to high carrier densities that are generated by the high light intensities reaching the device[76–78]. At the lower limit, the LDR is theoretically limited by the noise current[76], although in practice it is often limited by the sensitivity of the measurement equipment. The LDR of a photodetector is relevant for practical applications since it defines the range at which light detection can happen even at varying light intensities and without inaccuracies[76]. Based on this, a photodetector with a high LDR might be useful for a broad range of applications including complex systems such as communication and imaging or if the LDR is inadequate for such applications then it might be useful only for more basic sensing tasks.

2.2.3.1.2 Spectral Responsivity

The SR of an OPD defines the range of wavelengths on which an OPD can respond to a light-stimulus and serves to quantify the given response for each wavelength[21]. Therefore, SR, which is mainly influenced by the active layer's morphology[21,79], strongly influences the range of applications that can be achieved with a given photodetector. The calculation of SR is described in equation 2-2.

$$SR\ (\lambda) = \frac{I_p}{P_0} = EQE\,\frac{q\lambda}{hc} \qquad 2\text{-}2$$

where I_p is the photocurrent, P_0 is the input power and λ is the wavelength of light. Moreover, EQE is the external quantum efficiency, q is the elementary charge, h is Planck's constant, and c is the speed of light in vacuum. **Figure 2.9c** shows a schematic representation for the SR of a broadband OPD. As depicted in the image, the response of an OPD can be enhanced by applying a negative bias to the device. Devices tend to see an increase in SR thanks to the faster extraction of charge carriers at higher electric fields which is given by the increased biases.

2.2.3.2 Dynamic Characteristics

This subsection presents the dynamic characteristics of OPDs. **Figure 2.10** depicts schematic examples of the 3_{dB} bandwidth, spectral noise density (Sn), and specific detectivity (D^*) of OPDs. In the following, their theoretical basis and calculations are introduced.

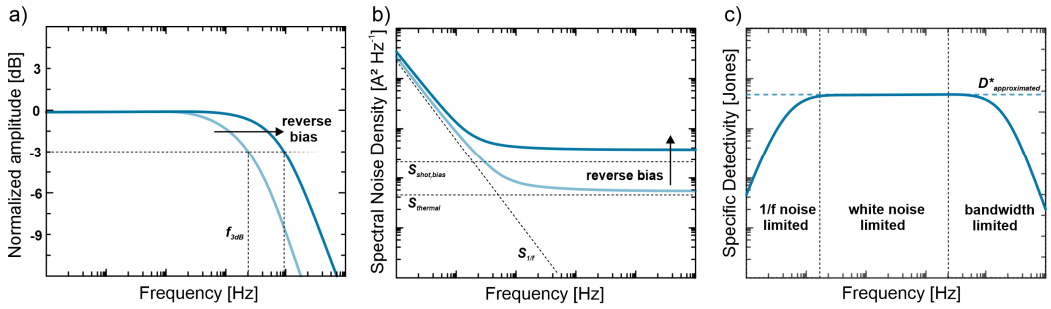

Figure 2.10 Schematics of the Dynamic Characteristics of OPDs.
a) Exemplary schematic of the normalized amplitude of an OPD response against the frequency of light used during illumination from where the -3_{dB} cut-off frequency is obtained. The plot highlights the contrast between cut-off frequencies achieved at different bias voltages. b) Exemplary schematic of the spectral noise density of an OPD showing the different types of noise as well as the contrast of electronic noise achieved at different bias voltages. c) Exemplary schematic of the specific detectivity of an OPD showing the different limiting regimes at different frequency ranges. Figure adapted from[21], CC-BY.

2.2.3.2.1 3 dB Bandwidth

Besides the aforementioned FOMs, certain photodetector applications also need to consider the detection speed of the device. This is particularly important for applications such as communication systems, where the data transmission rates involved require bandwidths within, or even above, the MHz range[21]. **Figure 2.10a** shows a schematic representation for the 3_{dB} bandwidth of an OPD. The detection speed is characterized by the cut-off frequency (f_{-3dB}) of the device which corresponds to the frequency of the input light signal at which the photodiode's output power response goes down 50%[21], as described in equation 2-3:

$$-3\,dB = 20 * log\frac{i(f_{-3dB})}{i_0} \qquad 2\text{-}3$$

where $i(f_{-3dB})$ is the current at the cut-off frequency, i_0 is the current at steady-state, and 20 is the gain factor that accounts for the power-current relationship[72]. Moreover, the total f_{-3dB} of a photodiode is defined by equation 2-4:

$$\frac{1}{f_{-3dB}{}^2} = \frac{1}{f_t{}^2} + \frac{1}{f_{RC}{}^2} \qquad 2\text{-}4$$

where f_t corresponds to the charge carrier transit-time-limited cut-off frequency and f_{RC} is the RC-time-limited cut-off frequency[21,80]. The charge carriers' transit time refers to the time needed for charge carriers to travel from its point of generation to its point of extraction and it is therefore influenced by the charge carriers' mobility μ and the thickness of the active layer on the device. The RC-time constant is given by equation 2-5:

$$t_{RC} = RC = R\varepsilon\frac{A}{d} \qquad 2\text{-}5$$

where R is the total series resistance composed of the diode's series resistance, as well as the resistance of the readout circuit; C is the capacitance of the photodiode, ε is the permittivity of the active layer, A is the active area of the device and d the thickness of the active layer. Based on equation 2-5, active layers of high thickness and smaller active areas should be used. However, this would increase the transit time of the chargers and thus an optimization must be performed in order to enhance device performance.

2.2.3.2.2 Spectral Noise Density and Specific Detectivity

Electrical noise refers to unwanted, spontaneous fluctuations in the measured response of an electronic system[76]. In the case of OPDs, noise makes it more difficult to distinguish the response signal to incident light and thus influences the sensitivity and reliability of light detection. The current measured in a photodetector fluctuates over time. The noise current (i_{noise}) represents the root mean square (RMS) value of these fluctuations around the average measured current (i_{mean})[21]. Moreover, noise sources can be frequency dependent or frequency-independent (i.e. white noise)[21,76]. For cases when white noise dominates, i_{noise} in units of A can me approximated by equation 2-6.

$$i_{noise} = \sqrt{2qi_{dark} + 4k_BTR_{shunt}^{-1}}\sqrt{\Delta f} \qquad 2\text{-}6$$

where q is the elementary charge, i_{dark} the dark current, k_B is Boltzmann's constant, T is the temperature, R_{shunt} the shunt resistance of the OPD, and Δf is the electrical bandwidth. Although widely used in literature, the use of this approximation often leads to underestimations of the value of i_{noise} and must therefore be avoided whenever possible, moreover it should be used with prudence by clarifying the methodology employed[21,76]. Moreover, i_{noise} depends on the electrical setup where the OPD is used. In order to obtain an accurate description of i_{noise}, the frequency dependency of i_{noise} should be taken into consideration. This is expressed for different frequencies f by the spectral noise density $S_{noise}(f)$ in units of A $Hz^{-1/2}$ as shown in equation 2-7:

$$S_{noise}(f) = \sqrt{S_{shot}^2 + S_{thermal}^2 + S_{1/f}^2(f)} \qquad 2\text{-}7$$

where, $S_{thermal}$ is the thermal spectral noise density given by equation 2-8:

$$S_{thermal} = \sqrt{4K_B T R_{shunt}^{-1}} \qquad 2\text{-}8$$

S_{shot} is the shot spectral noise density given by equation 2-9:

$$S_{shot} = \sqrt{2qi_{dark}} \qquad 2\text{-}9$$

and, $S_{1/f}$ is the flicker spectral noise density contribution given by equation 2-10:

$$S_{1/f} = \propto \frac{1}{f} \qquad 2\text{-}10$$

The three spectral noise densities composing the total spectral noise density represent the main sources of noise. $S_{thermal}$ represents the contribution from thermal noise due to the thermal excitation of charge carriers[21]. S_{shot} represents the contribution from shot noise which results from the quantized nature of charges that leads to fluctuations in their distribution over space and over time[21]. $S_{1/f}$ represents the contribution from so-called flicker noise which is strongest for low frequencies and results from frequency dependent sources such as the recombination and generation of electron-hole pairs[21]. **Figure 2.10b**

shows the schematic representation of the spectral noise density for a hypothetical OPD. As depicted, $S_{1/f}$ is strongest at low frequencies, $S_{thermal}$ dominates at 0V and S_{shot} dominates at higher reverse bias with the increase of i_{dark}.

In relation to this context, the sensitivity of a photodetector can be described by the noise equivalent power (NEP). NEP is defined as the power of incident light needed to obtain a signal to noise ratio (SNR) equal to 1[21,72,76]. This is shown in equation 2-11.

$$NEP = \frac{S_{noise}(f)}{SR(\lambda)} \qquad 2\text{-}11$$

where S_{noise} is the spectral noise density and SR the spectral responsivity. Although NEP can be used to assess the sensitivity; the specific detectivity (D^*) represents a more intuitive and practical description for the sensitivity of a photodetector[21]. It corresponds to the inverse of NEP normalized to the square root of the OPD active area (A)[76]. Thus, D^* is defined as the SNR obtained under 1 W of incident power and electrical bandwidth of 1 Hz for a photodetector with an active area equal to 1 cm^2[76]. D^* in units of Jones (cm Hz$^{-1/2}$ W^{-1}) can be derived from equation 2-12:

$$D^*(f,\lambda) = \frac{SR(\lambda)\sqrt{A}}{S_{noise}(f)} \qquad 2\text{-}12$$

Figure 2.10c shows the schematic representation of the specific detectivity for a hypothetical OPD. As depicted, flicker $1/f$ noise limits D^* at low-frequencies. At mid-frequency range, the curve flattens out and then becomes limited again at high-frequencies by the decay in response, which in turn is caused by a limited speed of response on the device[21,72]. For cases when white noise dominates, the frequency-independent D^* can be approximated by 2-13:

$$D^*(\lambda) \approx \frac{SR(\lambda)\sqrt{A}}{\sqrt{2qi_{dark} + 4k_BTR_{shunt}^{-1}}} \qquad 2\text{-}13$$

As mentioned before, even if widely used in literature, the use of such approximations often leads to important underestimations, in this case for D^*, and must therefore be avoided whenever possible, moreover it should be used with prudence by clarifying the methodology employed[21,76].

2.3 Organic Thin Film Transistors

This section aims to provide the reader with essential background knowledge in the working principles of OTFTs. In the following, the components, device architecture and principles of operation of OTFTs are presented.

2.3.1 Device Architecture and Working Principle

The transistors employed in this work are thin-film transistors belonging to the category of field effect transistors (FETs). **Figure 2.11** shows a schematic of a typical device architecture. FETs are composed by a semiconductor, an insulator, a source, a drain, and a gate.

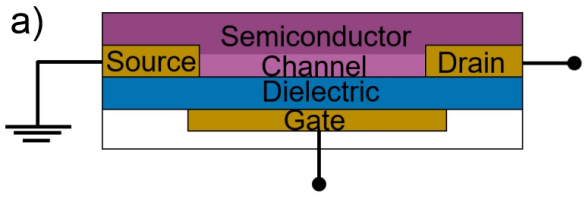

Figure 2.11 Exemplary Schematic of an OTFT Device Architecture.
a) Schematic of a transistor showing its different components including the source, drain and gate terminals. During operation a so-called channel forms between source and drain. Figure based on[81].

To operate the device, a voltage (V_G) is applied to the gate electrode while the source is grounded. At the same time, a voltage (V_D) is applied to the drain. Eventually, this allows a current to move between source and drain while the gate is used to modulate it. However, certain requirements need to be fulfilled. First of all, both V_D and V_G need to be applied, and V_G needs to be above a threshold value known as the threshold voltage (V_{TH}). This occurs because as V_G is applied, charges start to accumulate at the interface between the dielectric and the semiconductor materials in order to travel between source and drain. However, the initial charges are used to fill trap states in the material and therefore do not contribute to the current[81]. In the case when only V_D is applied, the device will remain in an off state. Once V_G is applied the accumulation of charges leads to the formation of the so-called channel between the source and the drain where current will eventually flow. Moreover, depending on the magnitude of V_D different regimes of operation will be achieved. A regime known as linear regime is achieved when $V_D << V_G - V_{TH}$[81]. In the linear regime, the current between source and drain (I_D) is given by equation 2-14:

$$I_{D,lin} = \mu Ci \frac{W}{L}(V_G - V_{TH})V_D \qquad 2\text{-}14$$

where μ is the mobility, C_i is the capacitance of the dielectric or insulator, W is the width of the transistor and L is the channel length. Moreover, when $V_D = V_G - V_{TH}$ a regime known as saturation regime is achieved[81] with I_D given by equation 2-15:

$$I_{D,sat} = \mu Ci \frac{W}{2L}(V_G - V_{TH})^2 \qquad 2\text{-}15$$

2.3.2 Figures of Merit

Figure 2.12 shows the I-V characteristics of a transistor. As it can be seen, the I-V characteristics are further divided into output and transfer characteristics. In the output characteristics, shown in **Figure 2.12a**, I_D is plotted against V_D at a given V_G. In this case, the linear regime, where I_D increases linearly with V_D, can be appreciated at low V_D values while the saturation regime, where I_D saturates, can be appreciated at high V_D values. **Figure 2.12b** shows the transfer characteristics where I_D is plotted both in linear scale and in log-scale against V_G at a given V_D. From the transfer characteristics the on/off ratio of the devices can be obtained for a given gate voltage by dividing the drain current by the off current (I_{off}), meaning the current measured when the device is off[81].

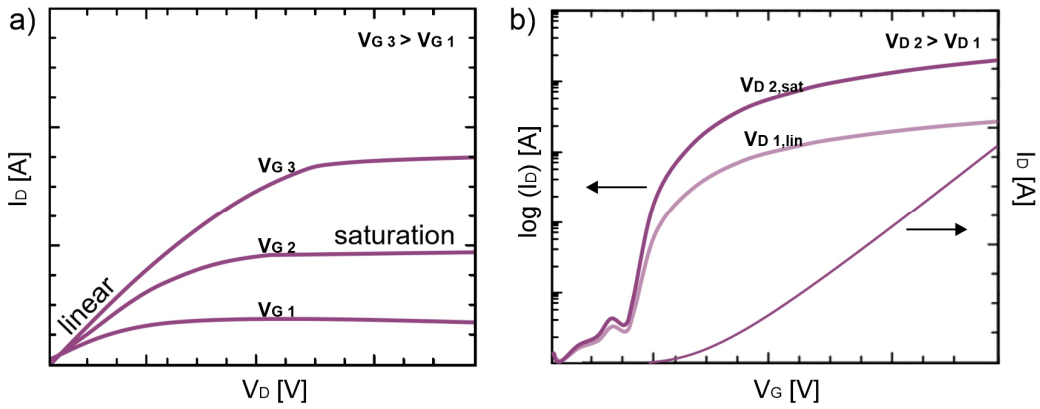

Figure 2.12 Schematics of the Output and Transfer Characteristics of Transistors.
a) Exemplary schematic of the output characteristics of an OTFT. The plot highlights the contrast between the linear and saturation regimes as well as the currents achieved at increasing gate voltages. b) Exemplary schematic of the transfer characteristics of an OTFT with the current plotted in both linear and log-scale. The plot highlights the contrast between the linear and saturation regimes which are achieved at different drain voltages. Figure based on[81].

Moreover, V_{TH} can be extracted from the linear-scale representation of the current in the saturation regime by extrapolating its linear fit to zero[81]. Finally, the field effect mobility of a transistor can also be obtained by measuring the transfer characteristics. In the saturation regime and for a V_G-independent mobility, the mobility is proportional to I_{Dsat} with V_G being proportional to the square root of I_{Dsat} following equation 2-15. However, if the mobility is V_G-dependent, equation 2-16 can be used[81]:

$$\mu_{sat}(V_G) = \frac{\partial I_{D,sat}}{\partial V_G}\frac{L}{WCi} \qquad 2\text{-}16$$

From the transfer characteristics in the linear regime, the mobility can be obtained with a linear fit to the changes of I_D with respect to V_G and based on equation 2-17[81]:

$$\mu_{lin} = \frac{\partial I_D}{\partial V_G}\frac{L}{WCiV_D} \qquad 2\text{-}17$$

Other methods and details about mobility calculation can be found in[82].

2.4 Indoor Visible Light Communication

Visible light communication (VLC) is a technology that uses the visible part of the electromagnetic spectrum to transmit data. Based on this, it offers specific, complementary advantages over standard technologies such as those based on radio communications systems. For example, the fact that light can be confined to a specific area simply by the walls forming a room, or by using focused light spots, it makes it possible to avoid the interference with other communication signals, it allows re-using the same light spectrum without problems, and it gives a higher degree of security in certain scenarios when considering that signals are difficult to interfere if they cannot leave the confined area[69]. Moreover, it is a wireless technology that can be used in places where standard radio communication is not allowed, for example, for safety reasons. Additionally, it can make use of existing infrastructure based on the fact that light emitting devices (LEDs) are widely available and finally, it can also be combined with other technologies such as solar cells in order to achieve a simultaneous data transfer and power generation. Some of the envisioned applications for VLC include communication between vehicles both in the streets as well as underwater, communication for wearable devices, communication using street lights, and indoor light-based communication in places such as hospitals, airplanes, industries or people's homes. On the other hand, some limiting factors affecting VLC technology are the illumination interference coming from common light sources such as standard building or city lighting, car lights, and sunlight[69]. Another important factor is the constrained rate of data transmission that can be achieved in VLC for example due to the limited bandwidth capacity of typical LED devices found in the market or around the cities[69].

Some relevant definitions in a VLC system are related to the amount of data being transmitted and to the efficiency and accuracy with which the data was transmitted. In this regard, the data rate in units of b s^{-1} is defined as the number of bits transmitted per second. The spectral efficiency in units of b s^{-1} Hz^{-1} corresponds to the rate that can be transmitted over a given bandwidth. In terms of accuracy or transmission reliability, the bit error rate (BER) expressed as a percentage corresponds to the ratio of received bits containing an error over the total number of bits transmitted[70]. In addition, the basic steps of a VLC system are composed by the encoding of data, the modulation of the light source or transmitter, the passage of the signal through an optical channel such as free space, then the detection of the light by the photodetector or receiver and a decoding of the signal to

obtain the original data[69,70]. In order to modulate the light projected by the transmitter, a modulator is used to convert the data bit stream into an analog waveform that can be applied to the transmitter. In this regard, there are many modulation methods which can be used depending on the objectives and constraints of the system[69]. In this work, a popular modulation scheme known as multi-band carrierless amplitude and phase (m-CAP) modulation scheme is employed[83,84]. This modulation scheme allows to overcome certain data transmission limitations in the system such as those related to the limited bandwidth of the LED and OPD employed. In particular, m-CAP consist of a division of the occupied bandwidth into several narrower subbands that allow to load data separately and to transmit data in bandwidths above the bandwidth limit of the transmitter and receiver[32,69,84].

2.5 Photosensor Matrices in Passive and Active Configurations

Depending on the intended application, OPDs can be used as individual sensors or as system formed by multiple OPDs. For example, in cases where spatial sensing or multi-channel sensing are desired, OPDs can be operated as a group by forming arrays of devices. Such arrays or matrices of devices can be of two types: Passive matrices or active matrices. In the context of this work, the case of active matrices refers to arrays containing both OPDs and OTFT devices. On the other hand, passive matrices refer to arrays containing only OPD devices. **Figure 2.13** shows a schematic example of an array of pixel components for each scenario. As it can be seen, in the case of passive matrices (**Figure 2.13a**), a pixel element corresponds to a single OPD device and in the case of active matrices (**Figure 2.13b**), a pixel element is formed by an OPD-OTFT combination. In both cases the process consist of a photoexcitation and charge generation by means of the OPD, followed by the discharge of the generated charge from the pixel into the reading lines, and ending with the reading of the signal at the readout electronics[59].

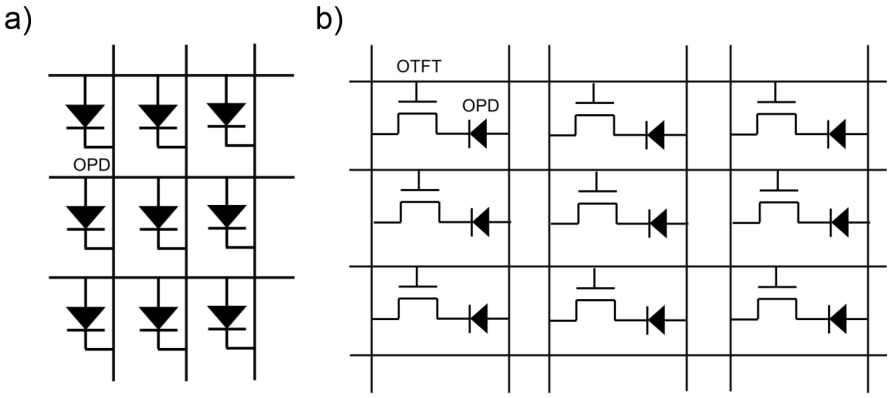

Figure 2.13 Schematics of Photosensor Matrices
a) Exemplary schematic of a photosensor passive matrix formed only by OPD devices. In this case a pixel is formed by an OPD. b) Exemplary schematic of a photosensor active matrix formed by OPD devices in combination with OTFT devices which allow for an active-switching. In this case a pixel is formed by an OPD-OTFT pair.

The main difference between both technologies is that the charge generated in the passive matrix will be directly transferred into the circuit reading lines while in the active matrix the signal can be hold by means of the controlled switching of the transistors and therefore it can be accumulated and selectively released before being transferred into the readout electronics[59]. Based on this, active matrices are capable of improving the signal to noise ratio when compared to signals acquired using passive matrices[51,59]. Additionally, different active matrix architectures are also possible. In some cases, the number of transistors employed could also be increased, for example, in order to add local signal amplification at each pixel. Possible sources of performance limitation within the operation of a given matrix can arise from leakage between pixels, parasitic capacitances either from transistors or from overlapped reading lines, a low photoresponse, a high dark current as well as dark current inhomogeneity in the OPDs[59]. In addition to this, other electronic components such as amplifiers, voltage drivers and readout electronics are necessary components of for both active and passive matrices.

3 Deposition Techniques

This section presents fundamental background knowledge of the different deposition techniques employed to deposit the materials and fabricate the devices presented in this thesis. The techniques are utilized to deposit functional layers in a layer-by-layer approach, until a complete device architecture is achieved. Most commonly, the different techniques are used in combination with each other, however, they can also be used individually by depositing all layers with a single technique. Although the deposition techniques have different operation principles, a part of the fabrication process remains similar in all cases. In particular, cleaning procedures for sample substrates, plasma treatments for surface energy modifications, as well as post-annealing steps for solvent evaporation and layer morphology are commonly used with all techniques. Details about the different processing treatments such as plasma and annealing steps are mentioned at the appropriate locations throughout the text.

3.1 Spin-coating

Spin-coating is a technique used to deposit solution-processed materials and that allows for a quick and reproducible processing of functional layers. Thus, it is particularly useful for a fast material screening and device development at the laboratory scale. In spin-coating, the sample substrate is first placed over a sample holder. The holder can either be custom-designed to match the sample layout or be a flat surface employing vacuum to keep the substrate in place. Subsequently, a volume of functional ink, typically in the micro-liter range, is placed at the center of the substrate to be spread along the complete surface area. The ink spreading is performed by rotating the sample holder at a defined speed, expressed in rotations per minute (rpm), and an acceleration, expressed in rpm per second. Depending on the input parameters different layer thicknesses can be obtained. Generally, lower deposition speeds (low rpm) will lead to thicker deposited layers and faster deposition speeds (high rpm) will lead to thinner layers. At the same time, the acceleration can be used to achieve a homogenous spreading of the ink, which is more likely achieved by starting with a low acceleration.

3.2 Inkjet Printing

As mentioned before, one of the main advantages of organic semiconductors is their solution processability, however, digital printing technologies can take this advantage one step further by adding great versatility in terms of design, efficient use of solution-material and an accurate control of material deposition with reproducible feature sizes in the range of 20 μm[21]. In this regard, inkjet printing is a widely applied and proved technique for the deposition of solution-processed materials. It has been proven to be successful in the deposition of complex material configurations including multilayer and multi-device systems[13,22–24]. In inkjet printing, the sample substrate is first placed over a substrate holder corresponding to a flat surface that employs vacuum to keep the substrate in place. As part of the process, the desired deposition layout is designed using a computer drawing software which is then used as input to the printer software to be finally translated into a 2D pattern of droplets deposited into the substrate. The deposition of the droplets is performed by an ink-ejecting print-head over the substrate holder. The possible displacement of the substrate holder and/or print-head as well as the angle-rotation capabilities of the print-head setup allow to adjust the printing resolution of the final pattern. Additionally, different inkjet printing technologies exist and during printing, droplet formation is induced by either continuous or drop-on-demand (DoD) technologies[85]. Generally, DoD is preferred over continuous-inkjet technologies because a wider range of materials can be used and a lower amount of material is wasted[85]. Similarly, within DoD inkjet printers, there is also subsets of technologies based on the technique used for droplet ejection, namely, thermal or mechanical techniques. In this case, due to greater flexibility on choice of ink and droplet tunability, most industrial and scientific reports based on inkjet printing use mechanical methods based on piezoelectric actuators[85]. Correspondingly, in this thesis, inkjet printers based on piezoelectric actuators are used. In particular, cartridges of 10 pL from Fujifilm, with a nozzle diameter of 21 μm, were utilized. **Figure 3.1** shows a schematic of the inkjet printing process using a piezoelectric-based print-head. In this case, an electrical signal is used to activate the piezoelectric material and trigger the ejection of droplets[85].

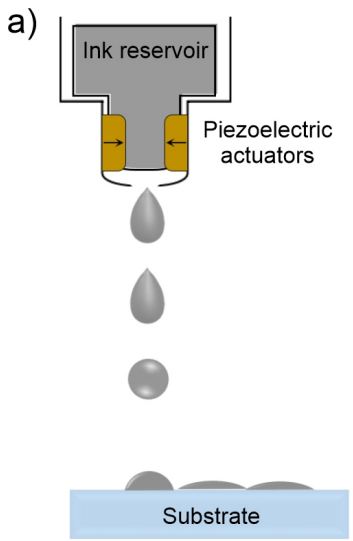

Figure 3.1 Working Principle in a Piezoelectric Inkjet Printer
a) Schematic of droplet ejection in a piezoelectric-based inkjet printer. The piezoelectric actuators are controlled by a waveform signal that must be optimized for each functional ink. Figure based on[85].

Moreover, the velocity and the size of a droplet can be adjusted by the fine-tuning of the electrical signals used as input. Such electrical inputs are optimized in terms of the shape and amplitude of a waveform. Each material to be deposited requires the definition of an appropriate waveform and the viscoelastic properties of the ink become relevant for a successful droplet ejection. In order to avoid clogging of the nozzles, the ink must have a low evaporation rate and therefore higher boiling point materials are better suited[85]. The viscosity of the ink is also important. Moreover, the viscosity is temperature dependent thus, if the ink is too viscous, the function of print-head heating can be used to lower the viscosity, as long as the components of the ink can resist these temperatures (up to 70°C) without degradation[86]. Ideal viscosity values at which droplet ejection can be achieved are in the range of 10 to 12 cP[86]. However, achieving droplet ejection is not enough since the velocity of the droplets is also important. If the drop velocity is too slow, it might be difficult to achieve optimal layer formation[85]. Similarly, too low viscosity can lead to a very high droplet ejection or to unwanted ejection with lack of control[85]. Finally, after the ink reaches the substrate, the substrate-ink interactions become relevant for the wettability and pattern formation where an optimal interaction will allow the merging of the individual droplets into a sharp pattern with the desired layout and free of holes[85]. In this regard, the printing resolution expressed in drops per inch (dpi) must also be optimized since an

excessive drop spacing (DS) will not allow the merging of the individual droplets and thus lose all possibility of achieving a closed layer while an excessively low DS can lead to a shapeless pattern with high ink agglomeration.

3.3 Thermal Evaporation

Thermal evaporation is a deposition technique using heat to evaporate a source material and that allows for layer deposition with a highly precise thickness and pre-defined structures. In thermal evaporation, the sample substrate is first placed over a sample holder which contains a pre-fabricated patterning mask. The layout of the mask serves to define the final structure of the deposited layers onto the sample surface. The sample holder is then placed on top of the source material where it remains unexposed to any material flow thanks to protective shutters. The material, typically in powder form or as a metallic pellet, is placed inside a crucible container. The container is then annealed under vacuum leading to the evaporation of the material, through the patterning mask and into the sample's surface. The power applied for annealing and the level of vacuum pressure vary depending on the material being deposited. During deposition the sample holder is in constant rotation in order to achieve a homogenous layer deposition. After the onset of evaporation, the protective shutters are removed and the sample holder is exposed to the evaporated material. The process continues at a pre-defined evaporation rate until the desired final layer thickness is achieved. The thickness is measured in real-time with quartz crystal sensors.

3.4 Substrate Cleaning and Device Encapsulation

Substrate cleaning is performed covering the samples with acetone and then with isopropanol, at different steps. In each case, the substrates are ultra-sonicated for 10 minutes before drying with nitrogen gas. Moreover, during OPD processing, an encapsulation of the devices is employed in order to maintain the stability of the devices. This consists of a liquid epoxy being placed on top of the OPD devices and cured with UV light in order to protect them from degradation by oxygen and water molecules present in the environment. In this work, a device encapsulation is present unless stated otherwise.

4 Characterization Methods

This section presents fundamental background knowledge of the different characterization methods employed as well as the methodologies followed to evaluate the materials and devices presented in this thesis. The techniques are utilized to characterize different types of samples such as substrates, materials in solution, materials in thin-film form and complete devices. The different analyses allow to gain insight into relevant physicochemical and mechanical properties of the materials to determine potential applications or to assess their compatibility with other components. Furthermore, they allow to characterize device performance and execute screening of potential materials. Additionally, they also help to understand the potential causes for either positive or negative device performance.

4.1 Characterization of Substrates and Functional Inks

In the following, the different methods employed to characterize functional inks and substrates in the context of this thesis, are introduced. In order to estimate if a functional ink can be successfully inkjet-printed into a given substrate and to ensure that the resulting pattern will match the expected outcome, the substrate and the ink must have a compatible interaction. To better understand the process of substrate-ink interaction and to estimate the likelihood of a successful deposition, both components need to be characterized in terms of their surface energy and in the case of the ink, also in terms of its viscoelastic properties.

4.1.1 Contact Angles, Surface Energies and Surface Tensions

When a liquid and a solid make contact, the surface of the solid will exhibit an affinity or a repulsion of the liquid. This occurrence is typically referred to as wettability[87]. The wetting properties in the interaction between a solid (e.g. a substrate) and a liquid (e.g. a functional ink) can be described in terms of their surface free energies (SFEs)[88] and their description is based in the work of Thomas Young and the measurement of contact angles. **Figure 4.1a** shows a schematic of the description given by Young. In specific, his work describes the physics between a solid surface and a liquid in terms of the interactions that occur at their interface and which are constituted by the solid-liquid (σ_{SL}), solid-gas (σ_{SG}) and

liquid-gas (σ_{LG}) SFEs from where a liquid to surface contact angle (θ_{CA}) is also obtained[72]. This is described in equation 4-1, known as Young's equation:

$$\sigma_{SG} = \sigma_{SL} + \sigma_{LG}\, cos\, \Theta_{CA} \qquad 4\text{-}1$$

In order to solve this equation, θ_{CA} can be obtained by contact angle measurements and the value of σ_{LG} can also be obtained experimentally by performing a pendant-drop measurement. On the other hand, the value of σ_{SL} cannot be measured directly[72,88,89]. Therefore, unless σ_{SL} is known, the SFE of a substrate can be calculated with an alternative methodology, particularly, from contact angle measurements where the substrate of interest is studied together with a group of solvents of different properties[89]. At first, a suitable set of liquids with known surface tensions must be selected, followed by the selection of a model that uses the contact angle measurements data as input to calculate the SFE values[89]. It is worth noting that various methods exist, and thus, the availability of different models as well as the option to select among different test liquids means that the SFE of a substrate will not be an exact value, but rather it will depend on the chosen parameters where a proper methodology must be used and specified[89]. In this work, the Owens/Wendt model was utilized. The model uses a polar and a dispersive component to describe the fluid/solid interactions where the polar and dispersive parts are meant to account for dipole-dipole interactions and van der Waals interactions[89], respectively. The model is described by equation 4-1 and equation 4-2:

$$\sigma_{SL} = \sigma_{SG} + \sigma_{LG} - 2\,(\sigma_{SG}{}^{P}\sigma_{LG}{}^{P})^{1/2} - 2\,(\sigma_{SG}{}^{D}\sigma_{LG}{}^{D})^{1/2} \qquad 4\text{-}2$$

which when combined, form equation 4-3 which represents a linear relation of the form $y = m \cdot x + c$,[89] as shown here:

$$\frac{\sigma_{LG}(cos\, \Theta_{CA} + 1)}{2(\sigma_{LG}^{D})^{1/2}} = (\sigma_{SG}^{P})^{1/2}\frac{(\sigma_{LG}^{P})^{1/2}}{(\sigma_{LG}^{D})^{1/2}} + (\sigma_{SG}^{D})^{1/2} \qquad 4\text{-}3$$

Based on its linear relation, equation 4-3 can be used together with the surface tensions of test liquids as well as their measured contact angles to determine the dispersive and polar components of a solid's surface energy, given respectively, by the intercept and the slope of the optimal fit line on the plotted data[89].

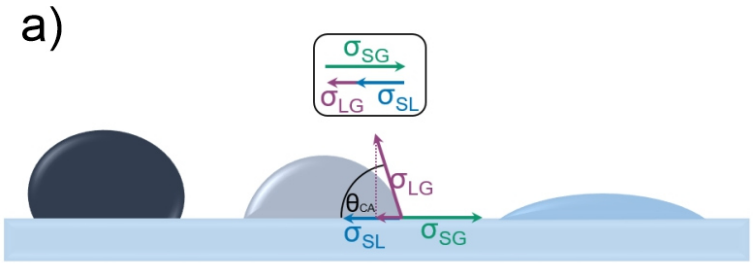

Figure 4.1 Exemplary Schematic of Different Contact Angles.
a) The interaction between a functional ink and a substrate as described by their SFE. The diagram exemplifies Young's description at equilibrium. Schematic based on[72,90].

4.1.2 Physical Properties of Printable Functional Inks

The characterization of the fluid mechanics of functional inks is another important component in the development process of new materials for inkjet printing. In the context of inkjet printing, their behavior is commonly described by the use of four dimensionless parameters. Namely, Reynolds (*Re*), Weber (*We*), Ohnesorge (*Oh*) and *Z*[85] as given by equations 4-4, 4-5, 4-6, and 4-7, respectively:

$$Re = \frac{\upsilon \rho a}{\eta} \tag{4-4}$$

$$We = \frac{\upsilon^2 \rho a}{\sigma} \tag{4-5}$$

$$Oh = \frac{\sqrt{We}}{Re} = \frac{\eta}{(\sigma \rho a)^{1/2}} \tag{4-6}$$

$$Z = \frac{1}{Oh} \tag{4-7}$$

where υ is the droplet velocity, ρ is the density, a is a characteristic length corresponding here to the nozzle diameter, η is the dynamic viscosity, and σ is the surface tension.

In this thesis, the viscosity was characterized by employing a RheoSense viscometer (VROC) which after measurement of a given ink, it utilizes equation 4-8 to calculate the viscosity[91]:

$$\eta = \frac{\tau}{\gamma} \tag{4-8}$$

with

$$\tau = -slope\ \frac{wh}{(2w + 2h)} \qquad 4\text{-}9$$

and

$$\gamma = \frac{6Q}{wh^2} \qquad 4\text{-}10$$

where τ is the wall shear stress, γ is the shear rate, w is the width of the channel, h is the channel depth, and Q is the flow rate. In specific, the ink to be analyzed is introduced into a channel and pushed while the pressure is measured and different points leading to a plot with linear behavior from where τ is extracted from the slope and all other required parameters are known[91].

Based on the parameters described above, the definition of ink characteristics suitable for droplet ejection in inkjet printing can be achieved[85], as shown in **Figure 4.2**. The figure shows an example of a commonly used representation for printable inks based on the *Re, We and Z* numbers. Depending on the measured properties of the ink being studied, the ink will fall into one of the defined zones such as printable, too viscous, or satellite droplet zones. Although this represents an important tool in the estimation of the jetting behavior of new inks the results must also be used in combination with relevant experimental tests before reaching conclusions.

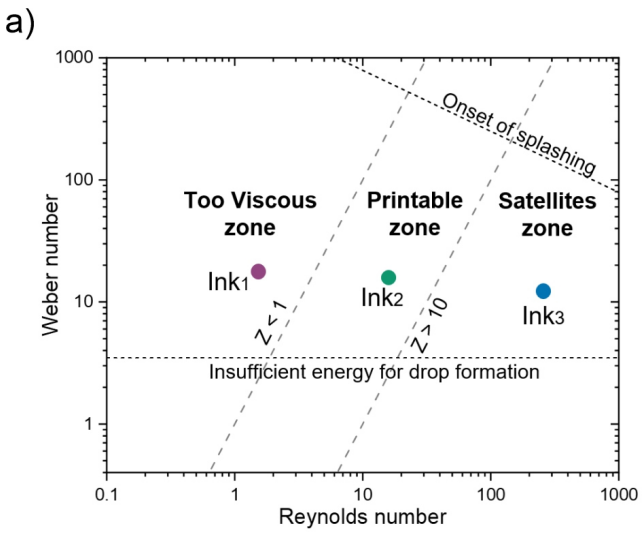

Figure 4.2 Exemplary Schematic of the Fluid Regime of Hypothetical Inks
a) Depending on the properties of the functional inks, they will fall into one of the zones defining their printing stability. Schematic based on[85,90].

4.2 Thin-film Characterization

In the following, the different methods employed in the context of this thesis to characterize the materials deposited in thin-film form, including both individual and complete devices, are introduced. The different techniques allow to assess relevant properties of the materials, such as composition and optical absorbance, that help to evaluate their compatibility with other components. At the same time, they can also help to understand the potential causes for either positive or negative device performance. Moreover, they allow an assessment of the quality of the fabrication process based on metrics such as material morphology, thickness, and homogeneity.

4.2.1 Microscopy

Optical microscopy is used to perform a detailed visualization of deposited materials. It allows for a quick but important assessment on the quality of a deposited layer. In particular, issues related to film formation such as gaps or holes in the material, material agglomeration showing high thickness inhomogeneity, or poor pattern definition are critical aspects to be considered for the development of systems composed by multiple layers. In this thesis, a Nikon Eclipse 80i optical microscope was employed where the sample sub-

strate is first placed over a sample holder that is illuminated with a light source coming from the top and which is subsequently reflected back to the ocular lens allowing to observe the magnified image. The microscope employed allows magnifications of 2x, 5x, 20, 50, and 100x.

4.2.2 Thin-film Profilometry

A Dektak stylus profilometer is an instrument that allows to characterize the surface profile of materials along a single and fixed axis line in order to measure the height and roughness of a deposited layer. In this thesis, a Dektak 150 surface profiler from Veeco was employed where the sample substrate is first placed over a sample holder that can be moved manually within its x (bilateral) and y (forward-backward) axis. After positioning the sample in the desired location, a stylus tip is lowered towards the base until it makes contact with the surface of the sample. The sample holder starts to move within a predefined distance while the tip scans the topography of the surface. Finally, the profile of the surface's sample is automatically plotted resembling to a visualization of hills and valleys where a reference- and measurement-marker allow to obtain differences in the height at various locations of the scanned layer. The different measurement ranges depend on the thickness and roughness of the deposited layer and correspond to 6.5, 65.5 and 524 μm with vertical resolutions down to 1 nm.

4.2.3 Optical Transmittance and Absorbance

Ultraviolet-visible (UV-Vis) spectrophotometry is used to perform an analysis of the interaction between light and the materials studied in this work. Of particular interest is the determination of the different wavelengths at which the materials can absorb light and which is especially relevant for the selection of the active layer component of an OPD device as this will predominately determine the spectral response and possible applications of the devices. In this thesis, an Avaspec (ULS 3648) spectrometer was employed where the sample substrate is first placed over a sample holder that is illuminated with a broadband light source coming from the top. Then, a reference measurement in the dark and under illumination need to be performed in order to account for the surrounding illumination as well as the contribution from the substrate material. During a test, the incoming light is measured at each wavelength after passing through the sample. The absorbance (A) is then obtained based on equations 4-11 and 4-12[92]:

$$A = -logT \quad (4\text{-}11)$$

with

$$T = \frac{il}{il_0} \quad (4\text{-}12)$$

where T is the transmittance il is the incident radiation and il_0 is the transmitted radiation.

4.3 Device Characterization

In the following, the tools and methodologies used to characterize the OPD devices presented in this thesis are introduced. When necessary, further details about specific conditions used during characterization are mentioned at the appropriate locations throughout the text. This is also the case for the methodologies followed during the demonstration of the OPD devices being applied in potential applications which are discussed at different points throughout the text.[a]

4.3.1 Current – Voltage Measurements

This subsection describes the tools and methodology employed to perform IV measurements in the devices presented in this thesis. For a background understanding, the fundamental description of the I-V characteristics of OPDs can be found in Section 2.2.1 and Section 2.2.3.

A semiconductor parameter analyzer Agilent 4155C was employed for the characterization of the current-voltage characteristics of the devices. In order to estimate an LDR, I-V measurements were also performed under illumination. In such cases, the samples were illuminated with LED light sources of specific wavelengths, as specified at the appropriate locations throughout the text. In all cases, the LEDs employed were powered using a Keithley 2636 A source measure unit (SMU). Moreover, neutral density (ND) filters (Thorlabs NDUVxxA/NE5xxB) were used to adjust the light intensity that reached the

[a] Parts of this section have been previously published in
Ruiz-Preciado, L.A., et al. Inkjet-printed high-performance and mechanically flexible organic photodiodes for optical wireless communication. *Sci Rep* **14**, 3296 (2024) ([32]). and Ruiz-Preciado, L.A., et al. Monolithically printed all-organic flexible photosensor active matrix. npj Flex Electron **7**, 6 (2023) ([13]). under the free creative-commons licenses (CC-BY).

devices. The light intensities employed are specified at the appropriate locations throughout the text.

4.3.2 Spectral Responsivity

This subsection describes the tools and methodology employed to perform SR measurements in the devices presented in this thesis. For a background understanding, the fundamental description of the SR characteristics of OPDs can be found in Section 2.2.3.

A broadband Xenon discharge lamp (450 W OSRAM XBO) was used as a light source and directed through a monochromator (Acton SP-2150i) to be selectively filtered at the different wavelengths. In all measurements, the light was modulated with a frequency fixed at 173 Hz by directing the light path through a Thorlabs MC1F10 chopper wheel. When necessary, a Keithley 2636 A was employed to apply a bias to the devices. During acquisition of the measurement signal using a lock-in amplifier (SRS SR830), an additional amplifier, Femto DHPCA-100 amplifier, was used for signal amplification. As part of the methodology, a calibration step is performed for the spectrum of the lamp at the start of each measurement using a calibrated photodiode (FDS100).

4.3.3 3 dB Cut-off Frequency

This subsection describes the tools and methodology employed to perform 3_{dB}-bandwidth cut-off frequency measurements in the OPD devices presented in this thesis. For a background understanding, the fundamental description of the bandwidth characteristics of OPDs can be found in Section 2.2.3.

The bandwidth characterization was performed by measurement of the transient current after illumination with a square-light signal of varying frequency. An Oxxius LBX520 laser was used as light source, the output of which, was modulated with an Agilent 33,522 A function generator. To record the signal, an oscilloscope (Agilent DSO 6102 A) was used. When necessary, a Keithley 2636 A was employed to apply a bias to the devices.

4.3.4 Noise and Detectivity

This subsection describes the tools and methodology employed to perform noise measurements in the OPD devices presented in this thesis. Furthermore, it also describes the

methodology used to obtain detectivity values based on the corresponding noise measurements. For a background understanding, the fundamental description of the noise and detectivity characteristics of OPDs can be found in Section 2.2.3.

During noise characterization, in-coupling of pickup-noise was avoided by a shielded box where the samples were placed while their dark current was being measured. In direct connection to the box, a FEMTO DLPCA-200 amplifier was used to amplify the signal. The signal was then collected with a Keithley 2636 A SMU. When necessary, an isolated voltage source (SRS SIM928) was employed to apply a bias to the devices. Thereafter, a python module developed by Dr. Mervin Seiberlich was used to process the data of the spectral noise density and the specific detectivity. In particular, to obtain the spectral noise density from the transient noise measurements: ‘‘a Hann window function was multiplied to account for digitization errors and the data was Fourier-transformed into reciprocal space to extract the frequency-dependency of the noise.’’[13]. Finally, the data obtained from the noise measurements, the data obtained from the SR measurements and the area of the OPDs are used in combination to calculate the specific detectivity of the OPDs according to equation 2-12, as presented in Section 2.2.3.

5 Fully-Inkjet-Printed Organic Photodiodes

Photodiodes already play a vital role in everyday life due to their numerous applications in modern electronics. However, as technology advances in the direction of areas such as IoT, wearable electronics, augmented reality, and personalized healthcare; there is an increasing need for light-sensors that can be fabricated in a cost-efficient and streamlined process, as well as an increased desire for light-sensors that can conform to varied and complex surfaces. In this chapter, the development of an organic photodiode stack that can fulfill these requirements is presented. The design and fabrication process is described and the main figures of merit are depicted and compared in different device architectures, namely, spin-coated, partially-printed and fully-printed devices. Finally, the high-performance of the developed devices is demonstrated by applying them in an optical communication system, a practical application that will certainly be significant in the implementation of interconnected systems such as IoT and wearable electronics.

Parts of this chapter have been previously published in the journal Scientific Reports[b] *under the free creative-commons license* (CC-BY)[32].

5.1 Introduction

Recently, OPDs have already achieved a level of performance that is comparable to inorganic devices[34,54,55]. However, the majority of advanced OPDs that are currently reported are fabricated with non-easily scalable techniques such as spin coating and thermal evaporation[6,21]. While the state-of-the-art performance achieved by fabrication methods such as spin coating is useful to set a reference point, it is not adequate for a streamlined fabrication of devices at an industrial level. Most importantly, it lacks the design flexibility that is needed in rapid prototype development, integration of multi-device systems, and personalized devices. Similarly, while flexible photodiodes are expected to significantly ex-

[b] Ruiz-Preciado, L.A., Pešek, P., Guerra-Yánez, C. et al. Inkjet-printed high-performance and mechanically flexible organic photodiodes for optical wireless communication. *Sci Rep* **14**, 3296 (2024). ([32])

pand the range of possible applications that can be currently achieved with rigid substrates, the successful implementation of such devices into mass-production areas such as wearables and IoT applications, requires the use of an easily scalable technique with a low-complexity and cost-efficient fabrication. Therefore, in order to fully exploit the advantages of OPDs, it is necessary to achieve the transfer of OPD fabrication into industrially-relevant fabrication processes, while simultaneously maintaining a high device performance.

In this chapter, the industrially-relevant technique of inkjet printing is used to develop a fully printed organic photodiode stack deposited on a mechanically flexible substrate, aiming to achieve a device fabrication with minimal process complexity and increased design flexibility, while maintaining a high device performance. There exist many possible options for flexible substrates, namely, polymer-, paper-, and fibers-based substrates, as well as ultra-thin glass and silicon substrates. In this chapter the widely known and inherently flexible polymer poly(ethylene 2,6-naphthalate) (PEN) was used as the base substrate due to its widespread use in the field of organic electronics. In addition, after the successful development of the OPD stack, the presented architecture was also tested in the ultra-flexible polymer parylene, this can be seen in Chapter 6 Section 6.2. To obtain a high device performance for the different figures of merit of fully-printed devices deposited in mechanically flexible substrates, the establishment of the processing conditions for each layer was necessary and is presented here. Moreover, the change in performance that occurs when the fabrication process is switched between fully-printed, partially-printed and spin-coated devices is discussed. Finally, to demonstrate the high device performance and promising applications of the developed devices, the OPDs are integrated as receivers in an indoor VLC system.

5.2 Design and Fabrication of Fully Inkjet-Printed OPDs

To achieve a functional device, the architecture, material selection and layer optimization as well as the establishment of processing conditions for each step of the fabrication process needs to be performed. In this section, the device design, ink formulations, printing parametrization, and processing conditions utilized to develop the devices are presented.

5.2.1 Device Design

In the following, the design of the fully inkjet-printed OPDs is presented. **Figure 5.1a** shows the stack architecture of the developed OPDs. The devices were fabricated directly on top of the flexible substrate PEN, using silver as the bottom electrode, followed by SnO_2 as hole-blocking layer, then a blend of the polymer donor poly(3-hexylthiophene) (P3HT) and the small-molecule acceptor 5,5′-[[4,4,9,9-Tetraoctyl-4,9-dihydro-s-indaceno[1,2-b:5,6-b']dithiophene-2,7-diyl]bis(2,1,3-benzothiadiazole-7,4-diylmethylidyne)]bis[3-ethyl-2-thioxo-4-thiazolidinone] (IDTBR) formed the BHJ-based active layer. Finally, the polymer poly(3,4-ethylenedioxythiophene) polystyrene sulfonate (PEDOT:PSS) was used as top, transparent electrode. A requirement for each of the selected layers is that the materials should be inkjet-printable. Besides this, the selected stack has several practical advantages. The silver nanoparticles forming the bottom electrode (see Section 5.2.2.1) have low-cost and high-conductivity, moreover, they are based on low reactivity solvents which can be deposited in multiple surfaces. SnO_2 has been proven to be a successful hole-blocking layer for high performance OPDs by yielding devices with low dark current and high responsivity[93,94] while also improving their reliability when compared to other materials such as ZnO, especially after the devices are exposed to UV radiation[95]. The BHJ P3HT:IDTBR has shown impressive optoelectronic properties leading to state-of-the-art performance in both OSC and OPD devices[34,61]. It is characterized by a broadband range of responsivity from 350 to 850 nm. This extended spectral response from visible to the near-infrared allows for a broad number of possible applications reaching responsivity values in the range of 200 to 400 mA W^{-1} and which are comparable to commercially available inorganic devices[34]. Additionally, the non-fullerene nature of the acceptor component IDTBR has shown to provide increased device stability and longer operational lifetimes as compared to devices employing fullerene acceptors[61,96–98]. PEDOT:PSS has been widely studied as an electrode in organic devices[99–105]. In particular, its high flexibility and transparency makes it an ideal material to function as the OPD top electrode. As a whole, the OPD stack presented here, using a top transparent electrode design and deposited via a digital printing technique, makes its fabrication process compatible with multiple substrates including those with pre-fabricated structures, thus facilitating the integration of these OPD devices in complex scenarios like those requiring the integration of multiple devices. A detailed example of such advanced application is explored in Chapter 6.

Figure 5.1b shows the energy levels of the different layers forming the OPD stack. In order to achieve a functional device, it is essential that the layers forming the stack work well not only individually but also collectively. In this case, the proper alignment of their respective energy levels allows an effective charge separation, transport and collection leading to an effective device performance. **Figure 5.1c** shows a top-view schematic of the layout design used to fabricate the devices. The schematic depicts four OPD devices to be deposited in a single substrate. The extended patterns of the silver and PEDOT electrodes form the contact pads that allow for an accurate measurement of the devices. The specific pattern was designed for compatibility with the sample-holder used in the measurement setup. The photodiode active areas are defined by the overlap of the bottom silver electrode and the top PEDOT:PSS electrode and are equal to 1 mm^2. The presented layout can be directly transferred as input into the inkjet printer and used to deposit the different materials layer by layer as depicted in **Figure 5.1d**. This can be further appreciated in **Figure 5.1e**, which shows a photograph of a real sample containing a step-by-step demonstration of the consecutive deposition process, namely, (i) silver, (ii) silver plus SnO_2, (iii) silver, SnO_2 plus active layer, and (iv) complete device. As it can be appreciated, both SnO_2 and PEDOT:PSS are semi-transparent. **Figure 5.1f** shows a photograph of a complete sample with four different OPD devices matching the layout used as input into the inkjet printer computer.

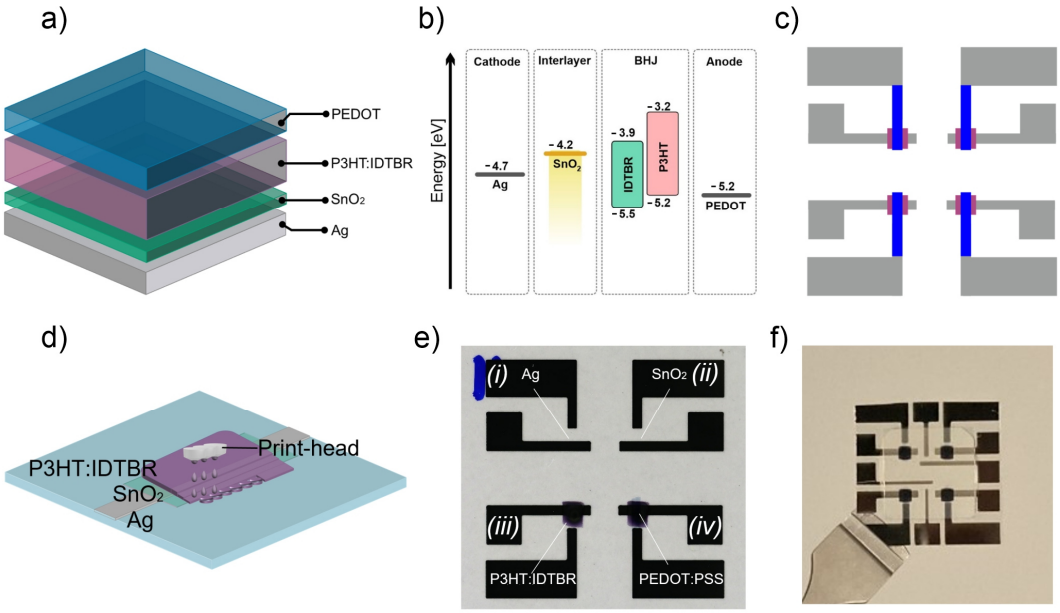

Figure 5.1 Materials, Design, and Fabrication of Fully Inkjet-Printed OPDs.
a) OPD stack. b) Energy levels of the materials forming the OPD stack. c) Schematic of sample layout. d) Schematic of printing process. e) Photograph of real sample depicting the layer-by-layer deposition. f) Photograph of completed sample showing four pixels. Panel a) adapted from[32], CC-BY. Panel b) adapted from[13], CC-BY.

5.2.2 Ink Formulations and Optimization of Inkjet Printing Parameters for Functional Layers

After the device design has been established, the development of ink formulations with corresponding printing parameters and the establishment of processing conditions is presented for each individual layer within the stack.

5.2.2.1 Silver and SnO_2 Layers

The quality of the bottom silver electrode of the OPD stack, in terms of homogeneity and morphology, will directly affect the quality of all consequent layers. Therefore, it is essential to achieve an optimal layer processing. In order to have a smooth deposition of the following layers, the silver layer should be homogenous and relatively thin, and must at the same time remain conductive to avoid detrimental electrical resistance in the device. In this work, the commercially available ink Sigma-Aldrich TGME silver nanoparticle dispersion was employed and deposited on PEN substrates that have been treated with Argon plasma for 1 minute previous to silver deposition. After deposition the samples

were annealed at 120°C for 10 minutes. **Figure 5.2a** shows an image of several test structures deposited on top of a PEN substrate. The squared structures shown here were deposited using various printing resolutions and sizes in order to find an optimally printed layer. Clearly, an excessively high dpi will lead to a shapeless pattern with high ink agglomeration. On the other hand, an excessively low dpi will not allow the merging of the individual droplets and thus lose all possibility of achieving a conductive layer. As seen in **Figure 5.2b**, the dpi also influences the final profile of the electrode where a higher dpi leads to thicker and less homogeneous layers. This can also be seen in **Figure 5.2c-e** which shows microscopy images of the structures at a dpi of 1270, 461.82, and 141.11, respectively. As it can be seen, a test structure with a dpi of 461.82 shows an optimal deposition. Finally, **Figure 5.2f** shows an example of a test structure deposited on PEN without the use of plasma treatment. As it can be seen, even if an optimal printing resolution is used, the quality of the layer is lower compared to the plasma treated samples.

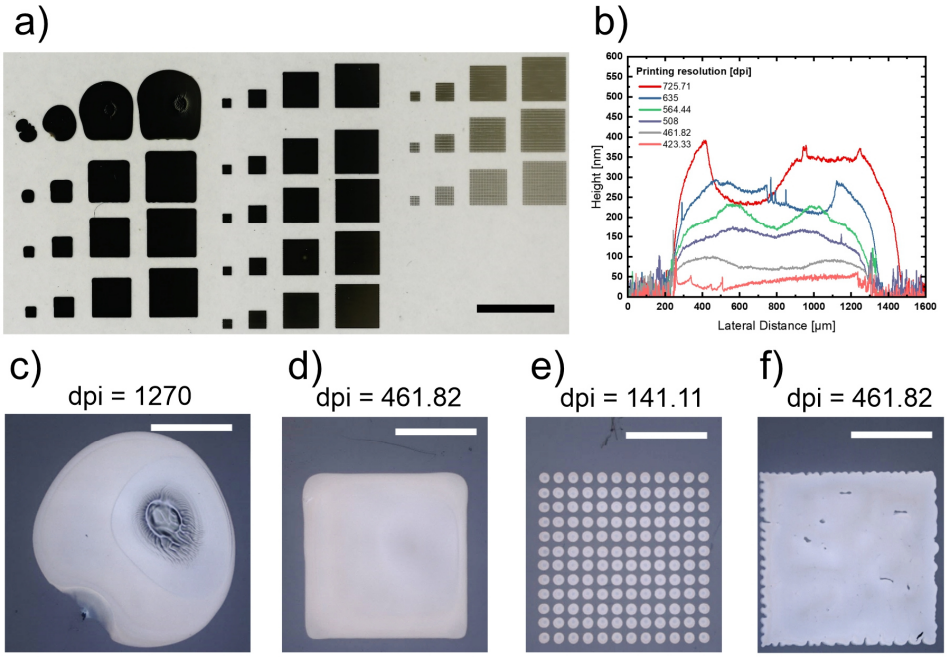

Figure 5.2 Silver Test Structures on PEN.
a) Photograph of silver test structures printed in PEN at different resolutions and different sizes (scale bar = 4 mm). b) Dektak measurements showing the profile of different test structures at different printing resolutions. c-e) Microscope images of silver test structures printed at a dpi of 1270, 461.82, and 141.11, respectively. 1 minute of Argon plasma treatment was used prior to deposition (scale bars = 1000 µm). f) Microscope image of silver test structure printed at a dpi of 461.82 in the case where no plasma treatment was used prior to deposition (scale bar = 1000 µm).

After the selection of the optimal printing parameters, further test structures were fabricated in order to develop the layout required for device characterization. **Figure 5.3a** shows finger structures of varied widths with values ranging from 250 µm up to 1 mm. As it can be seen, the printing direction can impact the quality of the deposited layer with the smallest fingers showing more straight horizontal profiles than their vertical counterparts. **Figure 5.3b** shows a microscope image of the optimized finger layout. The complete layout including contact pads is shown in **Figure 5.3c**. As mentioned before, the pattern of the contact-pads is designed to match the specifications of the sample-holder used in the measurement station.

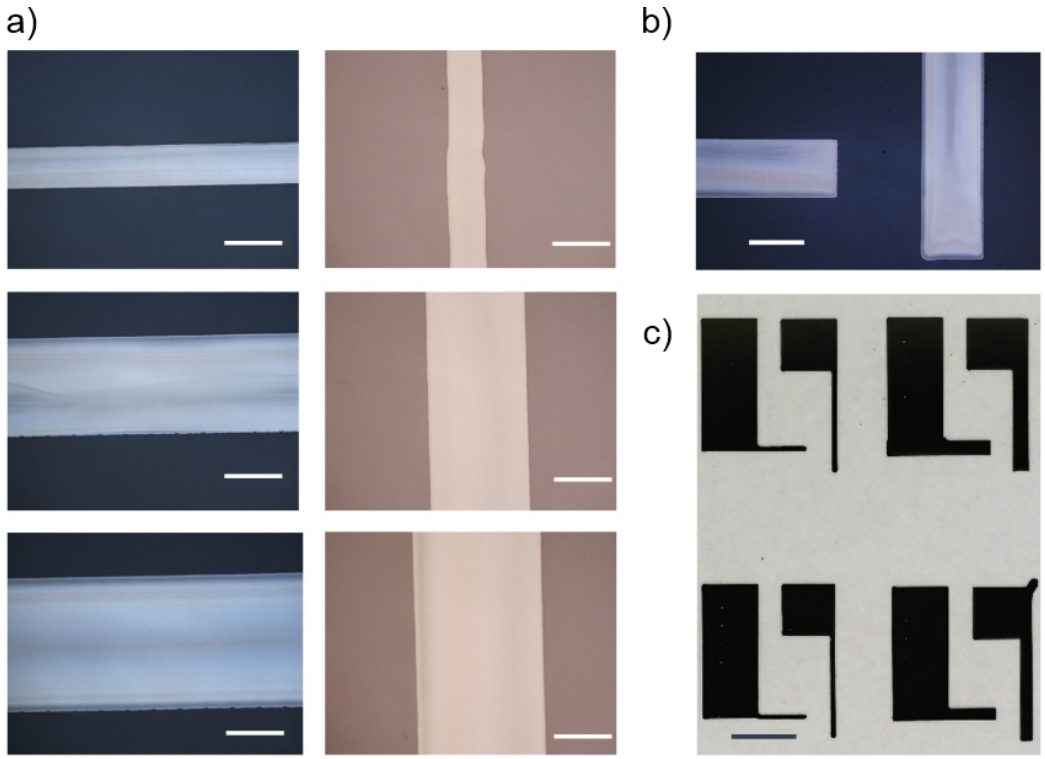

Figure 5.3 Silver Electrodes on PEN.
a) Microscope images of silver electrodes of varied widths printed in PEN (scale bars = 500 µm). b) Microscope image of optimized silver electrodes printed on PEN (scale bar = 1000 µm). c) Photograph of sample containing silver electrodes and contact pads (scale bar = 4 mm).

Moreover, the SnO_2 layer deposited on top of the silver electrode serves as hole-blocking layer and will directly affect the detection limit of the OPD device[94,106]. Therefore, it is important to achieve a high quality layer. In order to achieve functional devices with low

dark currents this layer should be pin-hole free and must have an optimal thickness. In this work, the commercially available ink Avantama N-31 was employed by mixing it with diethylene glycol (DEG) in a 2:1 ratio. A printing resolution of 700 dpi was used to achieve a thickness of 25 nm based on the recipe of Krebsbach et al.[94]. After deposition the samples were annealed at 120°C for 5 minutes. **Figure 5.4a** shows a microscope image of a silver electrode after deposition and annealing of the SnO_2 layer.

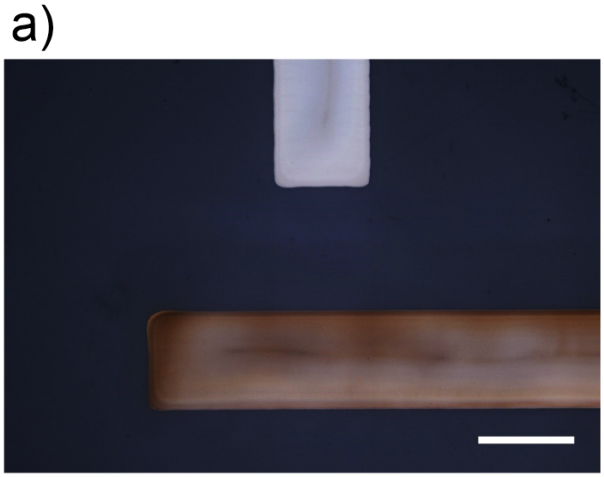

Figure 5.4 SnO_2 on Silver Electrodes.
a) Microscope image of SnO_2 layer deposited over silver electrode. The SnO_2 was annealed for 5 minutes at 120°C (scale bar = 1000 µm).

5.2.2.2 P3HT:IDTBR and PEDOT:PSS Layers

The BHJ active layer is responsible for the photoelectric conversion in the devices. Therefore, it is important to select the appropriate donor and acceptor materials as well as a solvent system that can dissolve both components. In the following, the development of the ink formulation for the P3HT:IDTBR inkjet printed active layers is presented. **Figure 5.5a** shows an schematic with the different components used in the ink formulation. The polymer P3HT and the small-molecule O-IDTBR are dissolved in 1,2-Dichlorobenzene (DCB) in a 1:1 ratio and at a concentration of 20 g L^{-1} and deposited with a thickness of ~350 nm via inkjet printing (dpi = 1204). **Figure 5.5b** shows the pendant drop analysis and contact angle analysis of the developed ink. The contact angle measurements, with an average contact angle of 7.75°, show that the active layer has a good wetting behavior when deposited on top of a PEN substrate covered with SnO_2, indicating that the active

layer ink is well suited for the OPD architecture employed. The pendant drop analysis was used to determine a surface tension equal to 25.90 mN m^{-1}, to estimate the printability of the ink as shown in **Figure 5.5c**. As it can be seen, the ink formulation lies in the printable zone of the Weber – Reynolds diagram. Therefore, the choice of DCB as the solvent material allows to obtain an ink with low complexity and with viscoelastic properties that match the requirements for droplet ejection during inkjet printing.

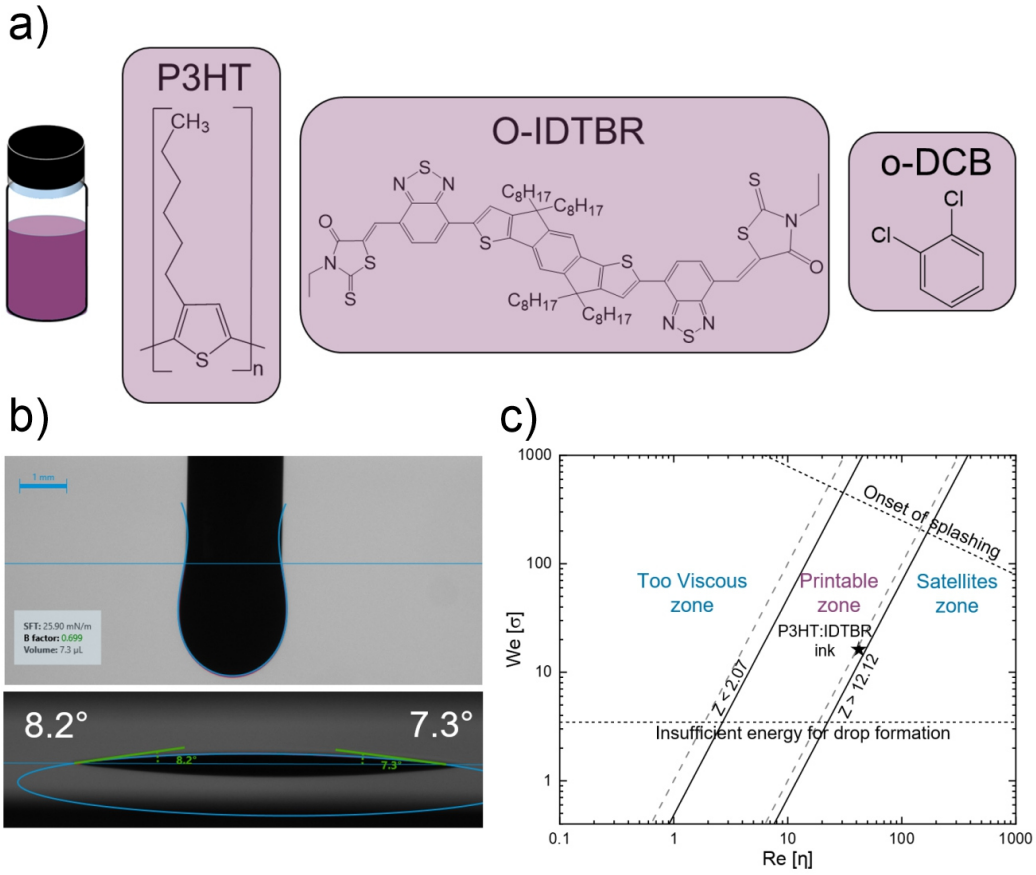

Figure 5.5 P3HT:IDTBR Active Layer Ink for Fully-Inkjet-Printed Devices.
a) Schematic of ink formulation for inkjet printing the P3HT:IDTBR active layer. b) Drop pending analysis (top) and contact angle analysis (bottom) for the P3HT:IDTBR ink. The substrate used corresponds to SnO_2-covered PEN. c) Assessment of ink printability for the P3HT:IDTBR ink. In this case, the z-values are defined by the continues lines and are based on the print-head employed (DMC 16110) while the dotted lines correspond to z-values in an ideal printable range[85,90].

Finally, the PEDOT:PSS layer deposited on top of the active layer serves as top electrode to operate the devices while at the same time allowing light to reach the active area of the OPDs. Therefore, the quality of the top transparent electrode of the OPD stack will directly

affect charge extraction. In this work, a 0.3%$_{vol.}$ of the surfactant Zonyl was added to the commercially available ink Heraeus Clevios FHC Solar and printed on top of the active layer at a resolution of 1270 dpi. **Figure 5.6a** shows images of several PEDOT:PSS test structures deposited on top of a PEN substrate. The structures shown here were deposited using printing resolutions of 846.67, 1016, 1270 and 1693.33 dpi. The optimal layer corresponds to the thinnest layer that remained conductive and was achieved at a resolution of 1270 dpi with a sheet resistance of 300 Ω/□. The squared boxes on the left image mark the location of printed patterns deposited at 846.67 and 1016 dpi. The right image shows the same sample photographed at a tilted angle in order to visualize all the printed structures. The bottom image contains finger test structures with widths of 250 µm and 1 mm. **Figure 5.6b** shows the contact angle analysis for the PEDOT:PSS ink over the active layer P3HT:IDTBR. The image shows a good wetting behavior of PEDOT:PSS on top of P3HT:IDTBR with an average contact angle of 21.25°. **Figure 5.6c** shows a microscope image of the complete device after the deposition of the PEDOT:PSS electrode. Note that the overlap of the bottom silver electrode and the top PEDOT:PSS electrode define the photodiode active area irrespective of the size of the P3HT:IDTBR layer.

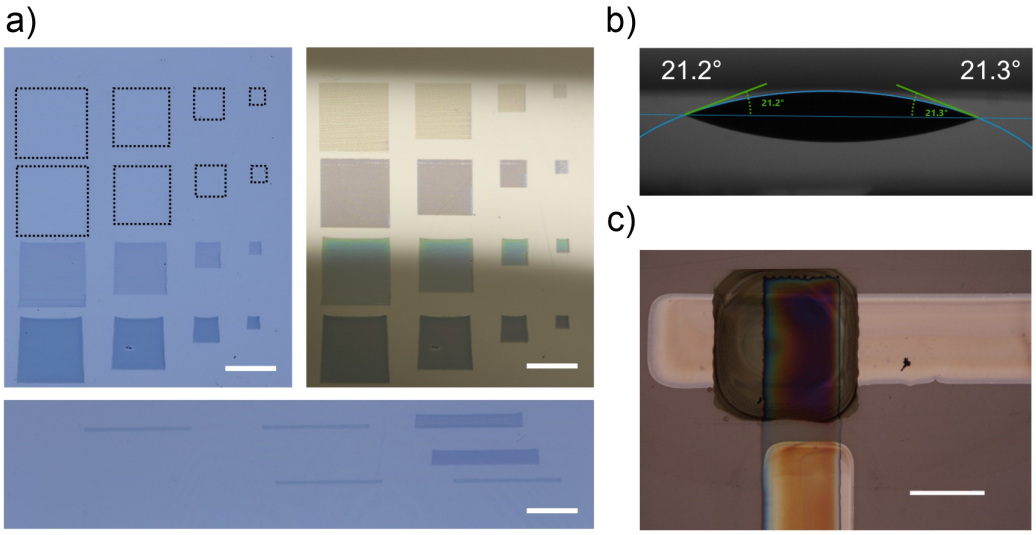

Figure 5.6 Inkjet-Printed PEDOT:PSS for Transparent Electrodes.
a) Photograph of PEDOT:PSS test structures printed at different resolutions and different sizes (top left). The same sample photographed at a tilted angle in order to visualize all the printed structures (top right). Photograph of PEDOT:PSS electrodes of varied widths (bottom). All cases correspond to PEDOT:PSS layers printed in PEN (scale bars = 4 mm). b) Contact angle analysis for the PEDOT:PSS ink over the active layer P3HT:IDTBR. c) Microscope image of a completed and fully inkjet-printed OPD device showing the PEDOT:PSS layer deposited over the active layer P3HT:IDTBR (scale bar = 1000 µm).

5.3 Characterization of Fully Inkjet-Printed Devices

After the device fabrication using the process discussed in Section 5.2, the fully-printed OPDs were characterized in terms of their main figures of merit. In this section, the performance of the devices in terms of steady-state and dynamic characteristics is presented. Additionally, a comparison to OPDs based on the same active layer P3HT:IDTBR but developed by other fabrication techniques, namely, spin-coated and partially-printed methods, is shown and discussed.

5.3.1 Figures of Merit of the Fully Inkjet-Printed OPDs

In the following, the static (**Figure 5.7**) and dynamic (**Figure 5.8**) characteristics of the fully inkjet-printed OPDs are presented. **Figure 5.7a** shows the J-V characteristics measured in the dark and at varied light intensities using a green LED (λ = 520 nm). The sweep in voltage from -3 to 2 V shows a characteristic diode behavior that confirms the success-

ful design and fabrication of the device stack. The plot shows a low dark current with a value of 2.27×10^{-7} A cm^{-2} at -2 V. Also consistent with the expected photodiode behavior, an increase in illumination intensity leads to an increase in the current output of the devices. **Figure 5.7b** shows the current density vs the optical power from where a good LDR value of 79 dB was determined at -2 V. **Figure 5.7c** shows the SR of the device. As it can be seen, the device has a broad SR in the range of 350 to 850 nm. It has a strong response in the visible range and finds its peak in the NIR at around 740 nm. This behavior is characteristic of the P3HT:IDTBR BHJ active layer used in the device stack, showing the spectral bands of both P3HT and IDTBR materials. When the bias voltage applied is increased we also observe an increase in the responsivity. At the peak wavelength of 740 nm this value increases from 333 mA W^{-1} at 0 V to 376 mA W^{-1} at -2 V where both values are comparable to those of other high-performing OPDs in the literature[107–113].

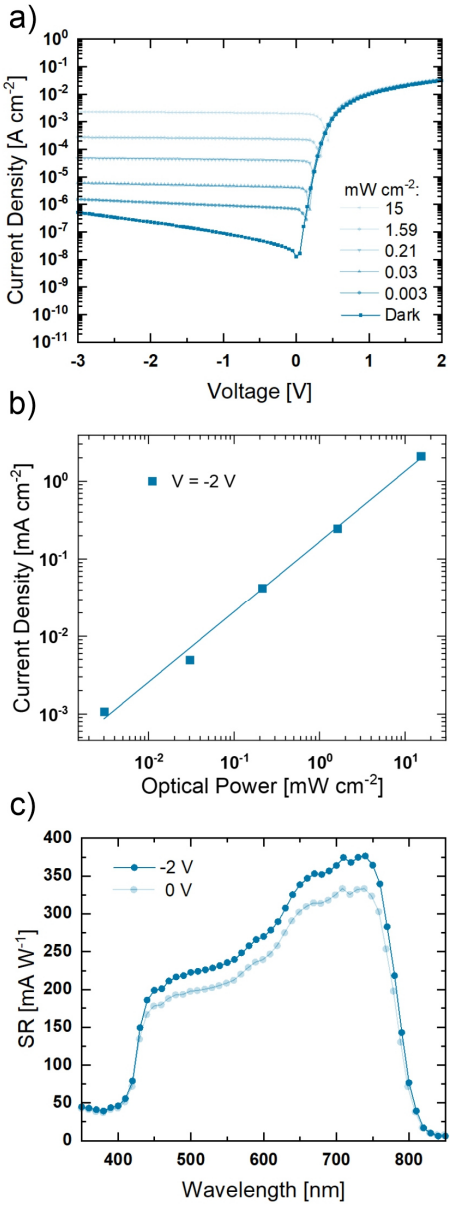

Figure 5.7 Static Characteristics of the Fully-Inkjet-Printed OPDs.
a) J-V curves at different light intensities, λ=520 nm. b) Linear dynamic range at -2 V, LDR= 79 dB, λ=520 nm. c) SR at 0 and -2 V. All panels in figure adapted from[32], CC-BY.

Figure 5.8a and **Figure 5.8b** show the spectral noise density *Sn* and specific detectivity *D** of the device, respectively. The *D** is calculated from the frequency-dependent noise measurements and exhibits a value of 1.8x10[10] Jones at -2 V. A python module developed by Dr. Mervin Seiberlich was used to process the data of the spectral noise density and the specific detectivity. Finally, **Figure 5.8c** shows the frequency response of the devices. The

OPDs reached f_{-3dB} values of 1.1 MHz at 0 V, which increases to 2.1 MHz at -2 V. The values presented here are competitive with those of other state-of-the-art OPDs, especially in terms of their high f_{-3dB} values[16,34,114].

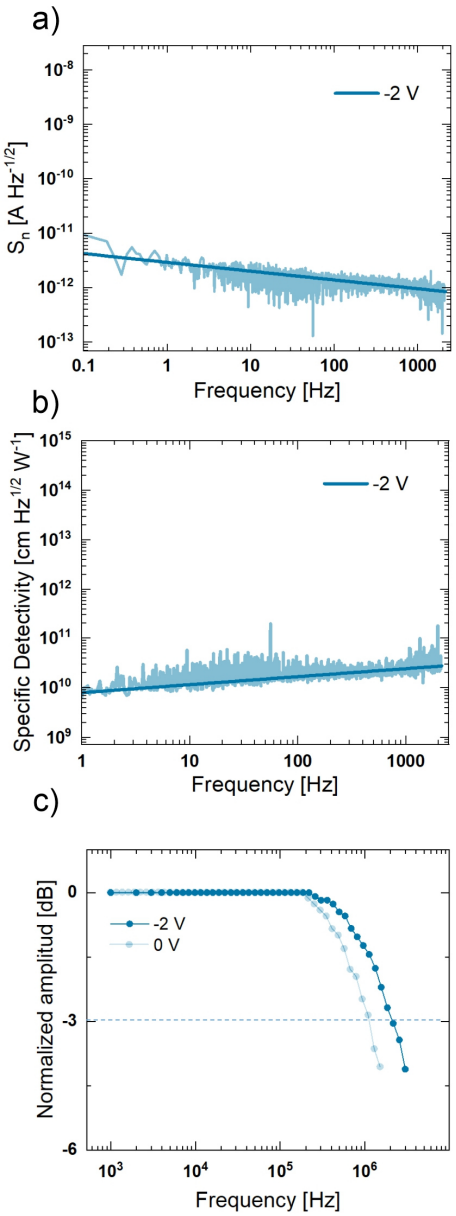

Figure 5.8 Dynamic Characteristics of the Fully-Inkjet-Printed OPDs.
a) Spectral noise density at -2 V. b) Specific detectivity at -2 V. c) Bandwidth measurements at 0 and -2 V. A python module developed by Dr. Mervin Seiberlich was used to process the data of the spectral noise density and the specific detectivity. Panel c) adapted from[32], CC-BY.

5.3.2 Comparison of Fully Printed OPDs versus Spin-coated and Partially-Printed Samples

After a complete characterization of the fully printed OPDs, their performance was compared to the performance of OPDs based on the same active layer P3HT:IDTBR but developed by using spin-coating and partially-printed fabrication methods. **Figure 5.9** shows the architectures and device photographs of the different OPDs studied. This corresponds to fully-printed (**Figure 5.9a**), spin-coated (**Figure 5.9b**), and partially-printed OPDs (**Figure 5.9c**). A comparison between different device architectures is useful to understand the advantages and disadvantages of each processing technique and to gain insight into the best applications of each OPD technology. Moreover, a fully printed fabrication represents both a more complex development and a more relevant and industrially advantageous process. Therefore, its comparison to lab-scale techniques allows to understand the trade-off between device performance and fabrication method. The device design and fabrication of the fully-printed OPDs is the same as presented in Section 5.2. The device design of the spin-coated and partially-printed samples was selected in alignment with the performance benchmark established for spin-coated devices utilizing the same active layer[34]. Another important distinction regarding the fabrication process of the devices comes from the ink formulation of the active layers. The solvent system in the active layers of spin-coated samples is chlorobenzene (CB). However, ink formulations optimized for spin coating are not optimal for applications in inkjet printing. Based on this, the active layers of the partially-printed and fully-printed samples use a different solvent system, namely, DCB. DCB has a higher boiling point as compared to CB. This results in a lower evaporation rate that helps to avoid clogging of the printing nozzles and therefore yields a more efficient printing process.

In the case of the spin-coated and partially-printed samples, the devices were fabricated on a glass substrate containing a pre-structured ITO pattern. ITO was used as the transparent electrode, which in this design allows entry of the incoming light. A spin-coated SnO_2 film of ~25 nm was deposited on top and used as hole-blocking layer. Then the P3HT:IDTBR active layer was either spin-coated (thickness 220 nm) or inkjet-printed (thickness 240 nm). Finally, a MoO_3 film (thickness 30 nm) and a silver film (thickness 100 nm) were vacuum evaporated on top and used as electron-blocking layer, and electrode, respectively. By comparing the photographs of the fabricated devices, the samples with inkjet-printed active layers show a distinctive spatial separation between pixels, emphasizing a reduced material consumption as compared to the spin-coated sample. The pixel

active area of all the devices in all the architectures employed is equal to 1 mm^2 as defined by the overlap between their corresponding electrodes. The photographs also display the flexibility of the fully-printed samples which represents an important advantage compared to the rigid samples, as it highlights its potential to enable versatile applications in multiple fields such as in wearable and flexible electronics.

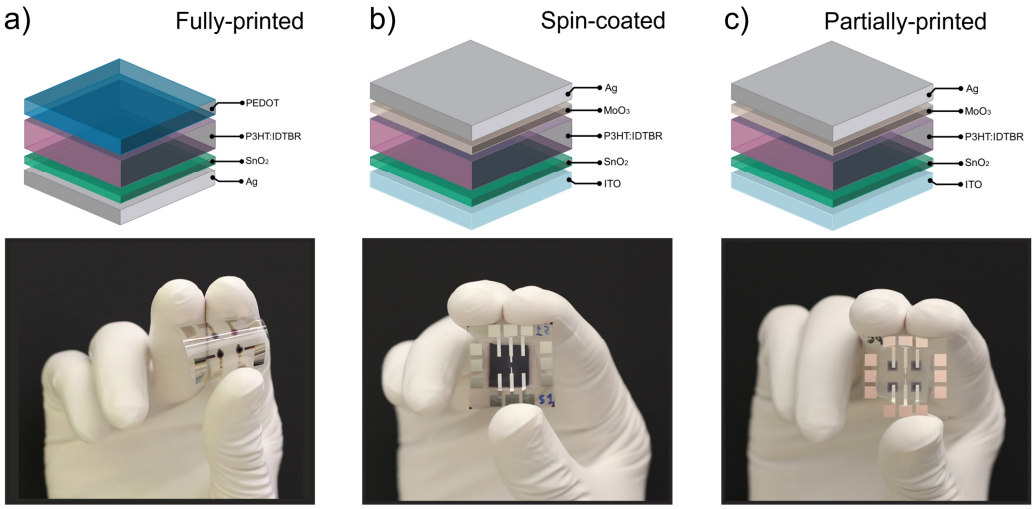

Figure 5.9 Device Architectures of the Fully-Printed, Spin-Coated, and Partially-Printed OPD Technologies.
a) Materials and photograph of fully-inkjet-printed OPDs. b) Materials and photograph of spin-coated OPDs. c) Materials and photograph of partially-printed OPDs. In the partially-printed OPDs, only P3HT:IDTBR was inkjet-printed. Figure adapted from[32], CC-BY.

Figure 5.10 shows a comparison between the J-V characteristics, the SR and the frequency response of the fully-printed OPDs against the spin-coated and partially-printed devices. **Figure 5.10a**, shows the current densities measured in the range from -3 to 2 V. In the photovoltaic regime, (e.g. at 2 V) the fully-printed sample shows the lowest current density, resulting from an increased series resistance in the device, while spin-coated and partially-printed samples maintain similar current levels. Under reverse bias (e.g. at -2 V), the three devices reached similar dark current levels, with 2.27×10^{-7} A cm^{-2} for the fully-printed sample as compared to 1.89×10^{-7} A cm^{-2} for the spin-coated and 3.9×10^{-8} A cm^{-2} for the partially-printed sample. Under illumination, the mismatch in dark current disappears completely, as the output current of the devices increases due to light exposure. Overall, the three devices show similar J-V characteristics and a good device performance.

Figure 5.10b shows the SR of the three devices at -2 V. As it can be seen, the SR of the fully-printed devices shows a higher performance. Moreover, the shape in the SR profile of the fully-printed samples also differs from the shape in profile of spin-coated and partially-printed samples. These variations can be attributed to variations in the thickness of the active layers of the samples. The fully-printed samples have an active layer thickness of ~ 350 nm. In contrast, the spin-coated and partially-printed samples have lower active layer thicknesses with values measured at ~220 and ~240 nm, respectively. A thicker active layer can boost the photoreponse of the device due to a higher light absorption. At the same time, previous literature reports on the influence of BHJ thickness variation have shown that thicker active layers can result in changes in the SR profiles of the devices[54,115–117]. Because the partially-printed and spin-coated samples have a similar thickness, they exhibit a homogenous response across the complete spectral range. They both show a gradual increase until their peak value at 740 nm, succeeded by a steep decline until 850 nm. On the other hand, the higher thickness in the fully-printed samples leads to a more pronounced increase in SR, which is particularly distinctive in the range of 400 to 600 nm. Overall, all devices cover the visible to NIR range of light from 350 to 850 nm, showing the characteristic behavior expected from P3HT:IDTBR. Furthermore, all devices reach state-of-the-art SR values when compared to other devices in literature[107–113]. In this case, the maximum SR value reached was 376 mA W^{-1} given by the fully-printed device at -2 V.

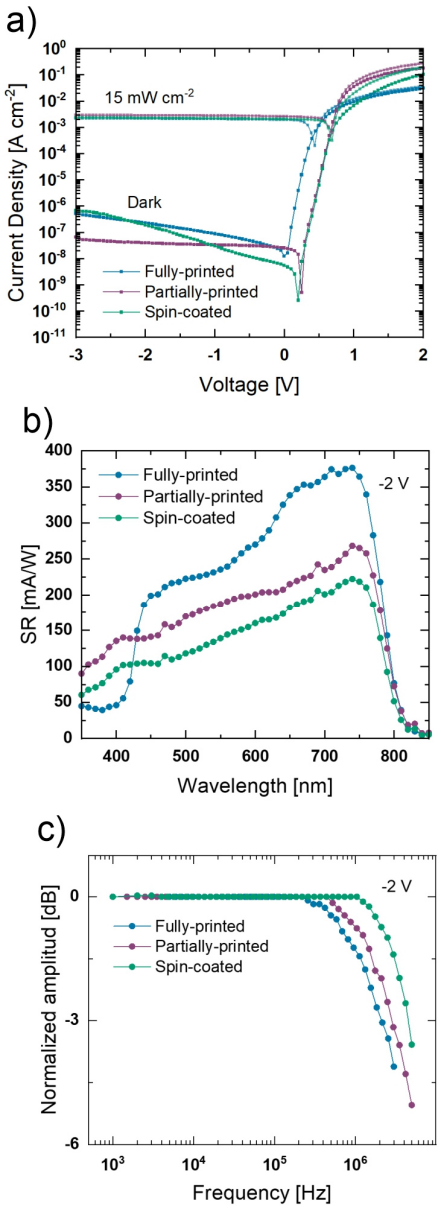

Figure 5.10 Comparison of Performance of the Fully-Printed, Spin-Coated, and Partially-Printed OPD Technologies .
a) J-V curves in the dark and under illumination, λ=520 nm. b) SR at -2 V. c) Band-width at -2 V. All panels in figure adapted from[32], CC-BY.

Figure 5.10c shows the frequency response of the three devices at -2 V. In this case, the fully-printed devices show the lowest performance. The samples reached a maximum f_{-3dB} of 2.1 MHz, as compared to 2.8 and 4.4 MHz from the partially-printed and spin-coated samples, respectively. The lower performance of the fully-printed samples in comparison to the partially-printed devices is ascribed to its higher active layer thickness. As men-

tioned before, the partially-printed and spin-coated devices have layer thickness around 200 nm. According to previous findings from our research group and published by Strobel et al. in[34], this thickness value provides an optimal balance between the transit time and the RC limit in these devices. Moreover, the findings showed that increasing the active layer thickness further, results in an increase in the transit time, consequently causing a decrease in detection speed. On the other hand, the performance of the fully-printed samples in comparison to the spin-coated devices is influenced not only by the active layer thickness but also by their differences in ink formulation. For instance, it can be noted that while using a similar active layer thickness, partially-printed and spin-coated devices have different detection speeds; with the partially-printed devices having a lower performance. As prior literature reports have demonstrated, the change of solvent systems from DCB to CB applied in P3HT-based blends[118,119], including P3HT:IDTBR compositions[120], can have a direct effect on the domain size and crystallinity of deposited layers. This can impact exciton diffusion and charge separation efficiency. This is then reflected in the performance of the different architectures where, as mentioned before, fully-printed and partially-printed samples use DCB and spin-coated samples use CB as their solvent system. To explore this further, **Figure 5.11** shows the bandwidth of the partially-printed sample against a control spin-coated sample fabricated with a DCB-based active layer, i.e., the same ink formulation as used in the printed active layers.

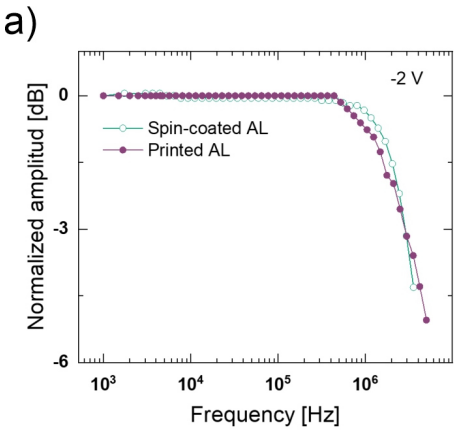

Figure 5.11 Spin-Coated and Partially-Printed Samples with DCB-Based Active Layer.
a) In this case both samples have same ink formulation based in DCB. Both samples reach f_{-3dB} values of around 2.8 MHz at -2 V. Figure adapted from[32], CC-BY.

In this case, both samples reach f_{-3dB} values of around 2.8 MHz at -2 V. This indicates that if the solvent system is maintained, it is possible to switch the fabrication technique while maintaining the detection speed of the device. Nevertheless, this is achieved by a decreased performance in spin-coated samples rather than an increased performance in printed samples. As discussed before, in optimal processing conditions, the results achieved by spin-coating outperformed the f_{-3dB} achieved by inkjet-printing. Another important consideration in this scenario is the trade-off between device performance and design flexibility since a fully printed fabrication represents a more relevant and industrially advantageous process. Finally, it is worth mentioning that, even though the performance of the fully-printed device was the lowest, it remains highly competitive when compared to other values reported in literature[15,16,21,114,121–126]. The values achieved for the spin-coated samples showing a f_{-3dB} of 4.4 MHz at -2 V, are among the highest reported to date for state-of-the-art OPDs[16,21,34,114] but they are based on a non-scalable technique in rigid substrates. On the other hand, the fully printed and mechanically flexible OPDs could be easily integrated in a variety of systems requiring a versatile design adaptation. The next section, presents the performance of the devices as receivers for an indoor VLC system and how the shift in fabrication process impacts performance.

5.4 Application of OPDs as Receivers in VLC System

After characterizing the fully inkjet-printed OPDs and comparing them to the performance of spin-coated and partially-printed OPDs, the OPDs were applied as receivers in a VLC system to assess their capabilities for practical applications in optical wireless communication (OWC) systems. The corresponding analysis is presented here. As mentioned before, the developed OPDs have detection speeds that rank about the highest reported so far for state-of-the-art OPDs. Therefore, a suitable field of application is in OWC systems for data transfer where high bandwidths are required and which will certainly be significant in the implementation of interconnected systems such as IoT and wearable electronics. **Figure 5.12a** shows a photograph of the setup and components employed during the experiments. The process started by generating the input signal in the processing computer using the software Matlab (i). Then, the signal was sent into an arbitrary waveform generator (AWG) (ii) connected to a bias-tee (iii) to be able to modulate the intensity of the LED (iv). In this case, a white LED light source with a bandwidth of 1.2 MHz and optical power of 21 mW cm^{-2} was used as the transmitter and the OPDs were used as the receiver

(v). In specific, each OPD technology was tested separately. Therefore, individual measurements were performed for each OPD receiver, alternating between the fully-printed, partially-printed, and spin-coated OPDs. In all cases, a power supply was used to bias the OPDs at -2 V (vi) and the output signal was amplified using a transimpedance amplifier (TIA) (vii). The acquisition of the received data was done in real-time using an oscilloscope (viii). Finally, for the purpose of regenerating the estimated data stream and to be able to determine a bit error rate (BER), the acquired signal was processed in Matlab and compared to the transmitted data sequence. The VLC measurements were performed in collaboration with the group of Prof. Stanislav Zvánovec from Czech Technical University (CTU) in Prague. The assembling of the VLC measurement setup and the processing of the VLC signals for data transmission was done by Dr. Petr Pešek and M.Sc. Carlos Guerra Yánez.

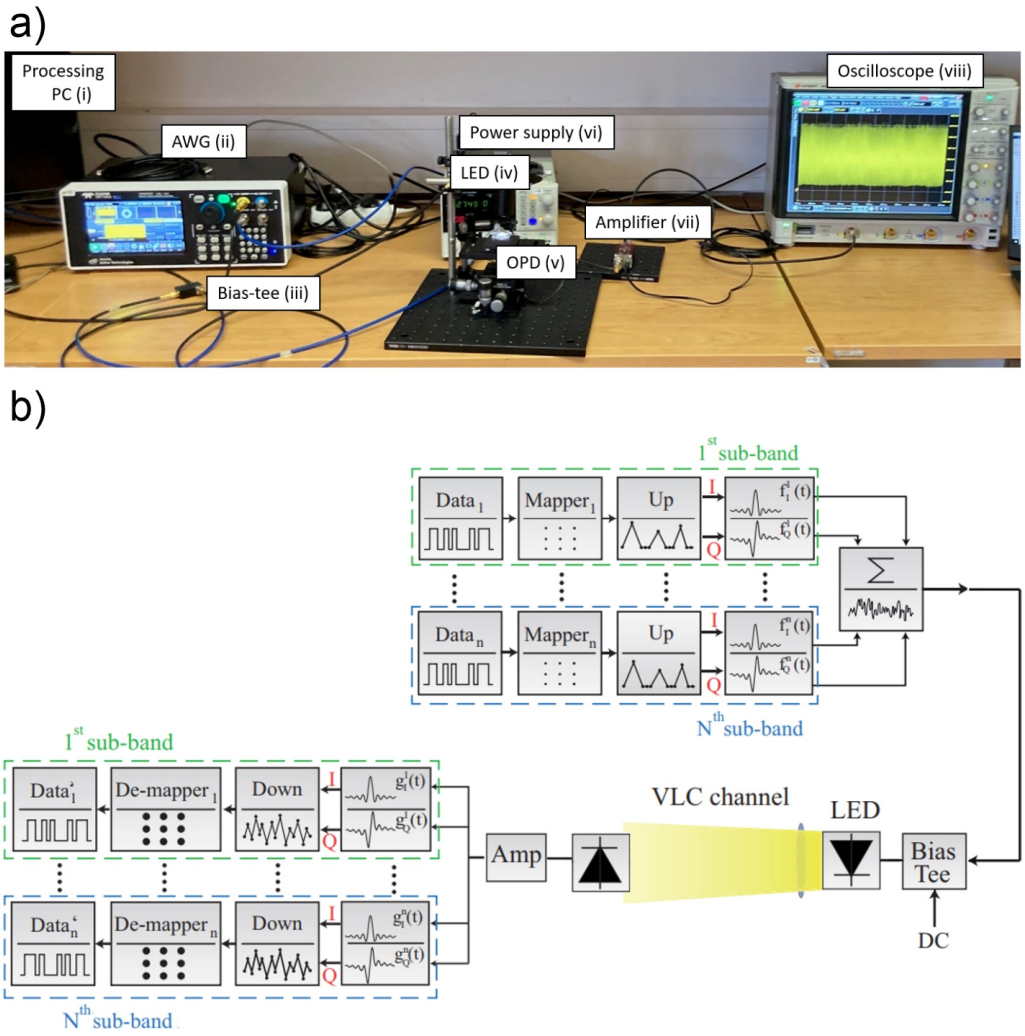

Figure 5.12 Experimental Setup Employed in the VLC Measurements.
a) Photograph showing the different components forming the VLC setup. b) Schematic of the VLC process. Individual measurements were performed for each OPD receiver alternating between the fully-printed, spin-coated and partially-printed OPDs. The assembling of the VLC measurement setup and the processing of the VLC signals for data transmission was done by Dr. Petr Pešek and M.Sc. Carlos Guerra Yánez. Panel b) adapted from[32], CC-BY.

A more detailed description of the VLC system can be seen in the block diagram depicted in **Figure 5.12b**. During the execution of the measurements, the modulation format known as multi carrierless amplitude and phase (*m*-CAP) modulation, was employed. The *m*-CAP modulation format is advantageous because it allows to transmit data at bandwidths that lie above the 3_{dB} bandwidth of the transmitter and receivers employed. In specific: "This modulation format allows us to divide the occupied bandwidth into sub-

bands that are affected by the distortion independently and load a different amount of data into each subband allowing us to effectively use a higher bandwidth beyond the 3_{dB} bandwidth of our devices.''[32]. More details about the *m*-CAP modulation format can also be found in[83]. **Figure 5.13a** shows the spectrum of the LED used as transmitter during the measurements. As it can be seen, the spectrum matches the range of photoresponse of the OPDs used as receivers (**Figure 5.10b**). **Figure 5.13b** shows the maximum spectral efficiency and maximum data rate obtained for each architecture studied where all measurements met the target BER limit of 7% forward error correction. The spectral efficiency of the fully printed OPDs, measured at 1 MHz and with the OPD biased at -2 V, is equal to 6.41 b s^{-1} Hz^{-1}. In comparison, the spin-coated and partially-printed OPDs showed values of 6.62 and 6.31 b s^{-1} Hz^{-1}, respectively. The maximum data rate of the fully printed OPDs, measured at 5 MHz and with the OPD biased at -2 V, is equal to 17.1 Mb s^{-1}. In comparison, the spin-coated and partially-printed OPDs showed values of 20 and 17.1 Mb s^{-1}, respectively. The individual spectrums received while conducting the measurements can be found in Figure A.1 in the appendix. It can be noted that the maximum data rates were obtained at a bandwidth above the 3_{dB} bandwidth of the OPDs and LED employed. As previously mentioned, this was possible thanks to the use of the *m*-CAP modulation technique which allows to transmit data at bandwidths that lie above the 3_{dB} bandwidth of the transmitter and receivers employed (see discussion **Figure 5.12b**). In general, the data rates obtained with all three OPD architectures are suitable for practical applications. Examples of possible applications include: data transfer from wearable sensors for health monitoring[127], indoor localization and control signals[128], and traffic safety with inter-vehicle communication[129]. Moreover, it can be seen that the three different OPD architectures showed a similar performance in terms of both the spectral efficiency and the maximum data rate. By comparing the fully-printed OPDs to the better-performing spin-coated OPDs, the absolute differences obtained are 2.9 Mb s^{-1} in terms of data rate, and 0.2 b s^{-1} Hz^{-1} in terms of spectral efficiency. Moreover, as it can be seen, the fully-printed OPDs were evaluated in both flat and mechanically bent scenarios (see inset in **Figure 5.13b**). During the bent measurements presented here, the sample was curved at a bending radius of 50 mm by employing a semi-cylindrical test structure. In general, measurements at bending radiuses above ≥50 mm showed consistent results. For example, a bending radius of 100 mm was also tested maintaining an equal performance (see Table 5.1). On the other hand, bending radiuses below 50 mm resulted in damage to the OPD samples due to the lack of mechanical flexibility in the epoxy used for encapsulation. An encapsulation was

employed as it is required to protect the devices from degradation by oxygen and water molecules present in the environment[61,130]. Further bending measurements were performed on the OPDs to evaluate their potential performance independently to the VLC system. These measurements took place inside a glovebox with low oxygen and water levels (<0.1 ppm), where encapsulation is not needed. In this case, the devices were placed under a monochromatic light source with a 520 nm wavelength while their output current was measured. From here, their photoresponses were evaluated at different bending radiuses, namely, 100, 50, 10 and 5 mm. As reported in **Figure 5.13c**, the results show that, after being subjected to even more extreme bending conditions, the photoresponse of the devices remains uniform. More specifically, by comparing the SR of our sample as measured in a flat state against the bent states the results show a maximum absolute difference of only 17 mA W^{-1} in SR. Based on these results, it is expected that optimizing the encapsulation approach, in particular by increasing the flexibility of the epoxy employed, would allow the devices to also demonstrate a consistent spectral efficiency and data rate at bending radiuses below 50 mm. In any case, it must be noted that despite the reduced flexibility caused by the encapsulation method, samples that can adjust to radiuses ≥50 mm, as shown within the VLC system, continue to be considerably more favorable than the rigid samples and allow for applications that require samples adaptable to different surfaces (see **Figure 5.13d**) and which cannot be achieved with the rigid samples.

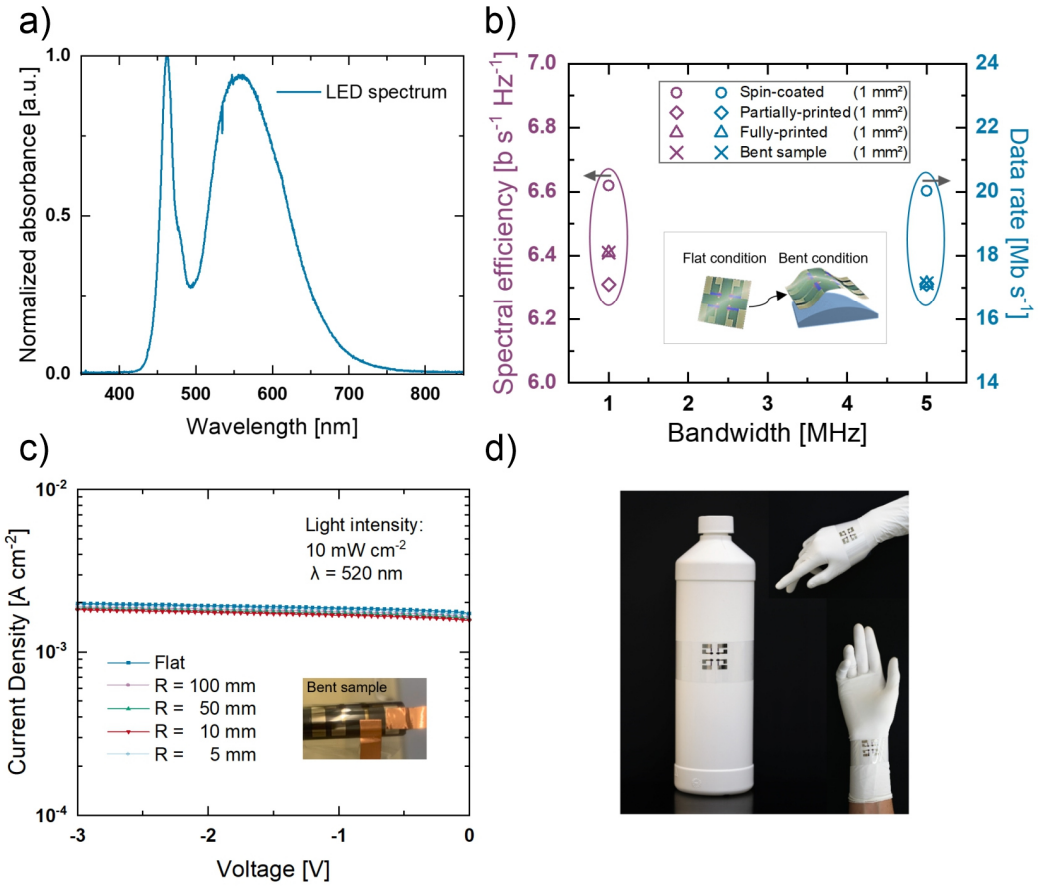

Figure 5.13 Application of OPDs as Receivers in VLC System.
a) Spectrum of the LED used as transmitter in the VLC system. b) Spectral efficiencies and data rates achieved with each OPD technology. The fully-printed OPDs were measured in both flat and bent conditions as schematically depicted in the inset figure. The bending radius corresponds to 50 mm. c) OPD photoresponse at different bending radiuses. d) Flexible OPDs adapting to different surfaces. The LED spectrum was measured by M.Sc. Carlos Guerra Yánez. The assembling of the VLC measurement setup and the processing of the VLC signals for data transmission was done by Dr. Petr Pešek and M.Sc. Carlos Guerra Yánez. All panels in figure adapted from[32], CC-BY.

In summary, the results presented in this section, which are summarized in Table 5.1, show that the fully-printed OPDs were successfully implemented as receivers in a VLC system where they demonstrated a performance suitable for practical applications and which is equivalent to the performance demonstrated by the OPDs developed by spin-coating and partially-printing methods. At the same time, their performance resembles that of other high-performing OPDs tested in VLC systems[7,15,121–125,131]. Moreover, the results show that the fully printed OPDs can also maintain their performance under bending conditions, which, combined with their manufacturing advantages, makes them prom-

ising candidates to be implemented in wearable, flexible and IoT applications requiring wireless data exchange. Finally, the results presented here are also relevant for the field of OWC, since VLC systems employing OPDs as receivers are scarce. It is particularly uncommon to find studies on VLC systems that employ OPDs with high f_{-3dB} bandwidths and VLC systems using OPDs deposited by digital printing techniques. Commonly, the predominant focus is either on inorganic devices or in organic transmitters such as organic light emitting diodes (OLEDs)[132–137].

Table 5.1 Overview of results obtained for the different OPD technologies in terms of VLC and SR measurements.

Fabrication method	Spin-coated	Partially-printed	Fully-printed				
Bending radius [mm]	Flat	Flat	Flat	100	50	10	5
SR [mA W^{-1}] at 0 V, λ = 520 nm	115	168	181	170	168	164	175
Spectral efficiency [b s^{-1} Hz^{-1}] at -2 V	6.62	6.31	6.41	6.41	6.41	-	-
Data rate [Mb s^{-1}] at -2 V	20.0	17.1	17.1	17.1	17.1	-	-

Note: Table 5.1 adapted from[32].

5.5 Summary

In this chapter, the development of an innovative and fully-inkjet printed OPD stack is presented. The aim was to develop an OPD stack with high design flexibility, and using a scalable fabrication technique while maintaining a high device performance. The OPD design is based on a top transparent electrode that can be fully deposited via a digital printing technique, making the fabrication process highly versatile and compatible with multiple systems and substrates. The OPD stack is composed by silver, SnO_2, P3HT:IDTBR, and PEDOT:PSS and it was developed in a mechanically flexible PEN substrate. The P3HT:IDTBR active layer employed in the OPD stack is characterized by a broadband range of responsivity, from 350 to 850 nm, making the devices suitable for a large number of possible applications. At first, the device design and fabrication was introduced by describing the ink formulations, printing parametrization, and processing conditions utilized to develop each layer of the devices. Subsequently, the fully inkjet printed OPDs were characterized in terms of their main figures of merit. The results demonstrated a successful fabrication process yielding high-performing OPDs. In particular, the characteristics obtained in terms of both static and dynamic performance are competitive with those of other state-of-the-art OPDs, especially in terms of their f_{-3dB} with a value of 2.1 MHz at -2 V. As part of the performance analysis, the fully-printed OPDs were compared to the performance of OPDs based on the same P3HT:IDTBR active layer but developed by using spin-coating and partially-printed fabrication methods. This allowed to understand the advantages and disadvantages of each OPD technology and to analyze the trade-off between device performance and fabrication method. The highest contrast in performance was seen in terms of the spectral response and the detection speed of the devices. In specific, the highest detection speed was achieved with the non-scalable spin-coated devices deposited on rigid substrates and corresponded to 4.4 MHz at -2 V, which is among the highest reported to date for state-of-the-art OPDs. In comparison, the fully-printed OPDs showed a highly competitive yet lower detection speed with a value of 2.1 MHz as well the highest spectral response with a value of 376 mA W^{-1} compared to 222 mA W^{-1} from the spin-coated devices. Overall, the three OPD technologies showed a high device performance. Finally, the OPDs were applied as receivers in a VLC system to assess their capabilities for practical applications in optical wireless communication systems where they reached data rates of up to 20 Mb s^{-1}, demonstrating a performance suitable for practical applications such as data transfer from wearable sensors for health monitoring. The VLC

measurements also showed that the performance of the fully-printed OPDs is equivalent to the performance demonstrated by the OPDs developed by spin-coating and partially-printing methods and at the same time, it resembles the performance of other high-performing OPDs tested in VLC systems. Therefore, the fully-printed OPDs proved their suitability in communication systems for data transfer. Additionally, the investigation also provided a valuable contribution to the field of VLC where studies of VLC systems using high-performing OPDs as receivers is still uncommon. More broadly, the OPD stack designed and developed in this chapter features promising advantages such as high processing versatility, mechanical flexibility and high performance that makes them promising candidates to be implemented in sensor networks and other interconnected systems such as IoT and wearable electronics.[c]

[c] *Parts of this chapter have been previously published in the journal Scientific Reports under the free creative-commons license* (CC-BY) *([32]).*

6 OPD-OTFT Integration

After the successful development and performance demonstration of the fully inkjet-printed OPD stack, the integration of the OPD devices with organic thin film transistors (OTFTs) is investigated. The objective is to achieve all-organic photosensor active matrices on thin, flexible substrates. To this end, the OPD architecture developed in Chapter 5 was tested in connection to two different transistor technologies provided by two different project partners, Pohang University of Science and Technology (POSTECH) in South Korea from the group of Prof. Sungjune Jung, and InnovationLab GmbH in Germany. An optimization in terms of design and integration approach was necessary for each OTFT technology and is addressed here. Moreover, the characteristics of the individual and integrated devices are depicted. Finally, a demonstration of the fabricated photosensor active matrices and their suitability for different applications is presented.

The experimental work presented in this chapter, in particular from Section 6.2, was developed in close collaboration with Dr. Sanghoon Baek. For this reason, an overview of the contributions to the various results is documented in Table A.1 of the appendix. Additional contributions by other authors are mentioned at the appropriate locations throughout the text.

Parts of this chapter have been previously published in the journal npj flexible electronics[d] *under the free creative-commons license* (CC-BY)[13].

6.1 Introduction

Recent advances in OPD development, such as those presented in Chapter 5, can promote their implementation into more advanced systems, like for instance, large-area photosensor active matrices. Matrices of optoelectronic devices are of particular interest because they enable spatial and multichannel detection of light[11,51,59]. Moreover, passive matrices which rely solely on photodetectors such as photodiodes, i.e. without incorporating tran-

[d] Ruiz-Preciado, L.A., Baek, S., Strobel, N. et al. Monolithically printed all-organic flexible photosensor active matrix. npj Flex Electron **7**, 6 (2023). ([13])

sistor devices, tend to be limited by electrical and optical crosstalk caused by high current leakage[51,138]. This results in lower resolutions and makes them unsuitable for large area applications. Integration of photodetectors with transistors, into an active sensing matrix, represents an alternative to overcome these issues. By making use of transistors to act as switches, this technology allows to individually address the employed photodetectors, increasing control of the electrical signals and reducing crosstalk[51,59]. To date, numerous examples on the integration of OPDs with transistors have been presented[13,41,139–154]. Most of these reports, however, utilize lengthened and expensive processing steps, non-scalable fabrication techniques, and heavily rely in the use of complementary components such as shadow-mask patterning. They are typically based on techniques such as, photolithography, thermal evaporation, coating, vacuum sublimation, or most commonly, a combination of these various deposition methods[13,143,153,154]. All of these approaches present drawbacks that prevent them from using all the advantages of large area electronics. At the same time, the use of organic materials has been mainly focused on hybrid systems such as the integration of OPDs with a backplane of inorganic transistors. Only a few studies have applied industrially-relevant and easily-scalable methods to realize all-organic OPD-OTFT photosensor systems[142,145].

In this chapter, the industrially-relevant technique of inkjet printing is used to monolithically integrate OPDs and OTFTs to form all-organic active matrices on mechanically flexible substrates. For this, it is necessary to establish a robust fabrication process with minimal complexity and high design flexibility while achieving a homogenous performance over the complete array of OPD-OTFT devices[13]. The fully-printed OPDs are monolithically integrated into two different OTFT technologies. The first technology was developed by the group of Prof. Sungjune Jung at POSTECH and corresponds to an inkjet-printed matrix of transistors composed of bottom-gate, top contact OTFTs. In this case, the devices are deposited on the ultrathin and flexible parylene polymer. The second technology was developed by partners at InnovationLab GmbH and corresponds to a photolithography-patterned, inkjet-printed matrix of transistors composed of top-gate, bottom contact OTFTs. In this case, the devices are deposited on PEN. To obtain a successful compatibility between OPD and OTFT devices and to maintain a high device performance after the integration process, an optimization in terms of design and integration approach was necessary for each OTFT technology and is addressed here. Moreover, the characteristics of the individual and integrated devices are depicted. Finally, the fabricated photo-sensors

and their suitability for different applications are presented in terms of static and dynamic demonstrations.

6.2 OPD Integration to POSTECH's Backplane

This section presents the work developed for the integration of the fully-inkjet printed OPDs into the backplane of OTFTs developed by the group of Prof. Sungjune Jung at POSTECH. The design and integration approach followed for each pixel as well as for the complete matrix is addressed. Then, the characteristics of the individual sensor elements, as well as those of the integrated devices, are presented. Moreover, an optimization of the integrated devices is discussed. Finally, a demonstration of the active matrix is presented.

6.2.1 Matrix Backplane and OTFT Characteristics

In this section, the matrix of transistors provided by POSTECH is described. In addition, the individual characteristics of the OTFT devices forming the matrix backplane are presented. The fabrication of the OTFT matrix samples used for the integration and the characterization of individual OTFT devices was done by Dr. Sanghoon Baek from POSTECH. The design of the integration layout used in the OPD-OTFT integration was done in collaboration with Dr. Sanghoon Baek and Dr. Noah Strobel with contributions from all three participants. The layout is presented in **Figure 6.1a**. The OTFT stack for the presented layout can be seen in **Figure 6.1b**, the OTFTs are deposited by inkjet-printing silver on top of parylene to form the gates of the devices. A second parylene layer covers the gate and functions as the dielectric material, followed by a second silver pattern that forms the source and drain electrodes of the transistors. The semiconductor material, poly(N-alkyl diketopyrrolopyrrole dithienylthieno-[3,2-b]thiophene) (DPP-DTT), is then printed to define the active area of the transistors. Finally, an additional parylene layer is deposited on top to be used as interlayer and serves as the base where the fully inkjet-printed OPDs are integrated[13]. A microscope image of the fabricated devices can be seen in **Figure 6.1c**. Further details on the processing of the OTFT devices can also be found in[13,155].

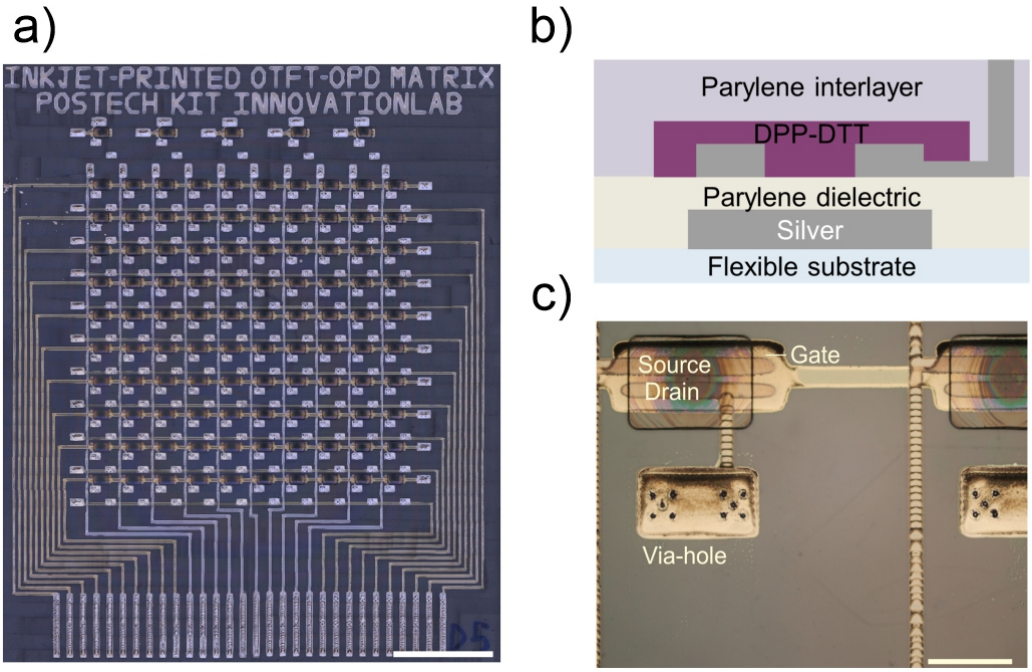

Figure 6.1 Matrix Layout and OTFT Design Used for OPD-OTFT Integration.
a) OTFT matrix used for the OPD-OTFT integration (scale bar= 1 cm). Sample photograph provided by Dr. Sanghoon Baek. The design of the integration layout was done in collaboration with Dr. Sanghoon Baek and Dr. Noah Strobel. Moreover, the fabrication of the OTFT matrix and the characterization of the individual OTFT devices was done by Dr. Sanghoon Baek. b) Material stack of the OTFT devices. The flexible substrate corresponds to parylene. c) Microscope image of the OTFT devices (scale bar= 1000 µm). Panels b) and c) adapted from[13], CC-BY.

The transistors employed in this chapter correspond to inkjet printed OTFTs with a bottom-gate, top contact architecture. The devices have a width-to-length ratio W/L = 25, an average threshold voltage (V_{TH}) of -1.2 ± 0.13 V and an average mobility µ of 0.09 ± 0.01 cm^2 V^{-1} s^{-1} [13]. **Figure 6.2a-b** depicts the transfer and output characteristics of a standard OTFT device. As it can be observed, the devices do not show a hysteresis. This suggests minimal charge trapping and highlights their stability. The on-current (I_{DS}) and off-current (I_{OFF}) of the devices are ~1 µA and ~7 pA, respectively. It can be noted that, since our main interest lies on the performance of the OTFT devices after undergoing the integration process, measurements were performed on OTFT samples where OPDs had been already deposited on the same substrate. Nevertheless, the OTFTs were measured individually as discrete components since after integration it is still possible to address the discrete components individually. A detailed description of the integration process is

presented in Section 6.2.2. To individually address the OTFTs, the voltages used were the gate to source voltage (V_{GS}) and the drain to source voltage (V_{DS}).

Given that the OPD-OTFT integration aims to achieve photo-sensitive matrices, the change in response of the OTFT devices when exposed to light was also considered. **Figure 6.2c** shows the relative change in current ($\Delta I/I_0$) shown by OTFT devices under illumination at different light intensities. ΔI is the difference between the values of current in the dark and under illumination and I_0 corresponds to the current in the dark. As it can be seen, the devices show negligible changes in current at λ= 520 nm, for both the saturation (V_{DS}= -10 V) and linear regime (V_{DS}= -1 V).

Finally, in order to corroborate that the deposition of OPDs do not influence the performance of the OTFTs, the devices were also compared before and after integration. This is presented in **Figure 6.2d**. where no degradation in electrical performance can be seen in the transfer characteristics after the OPD integration.

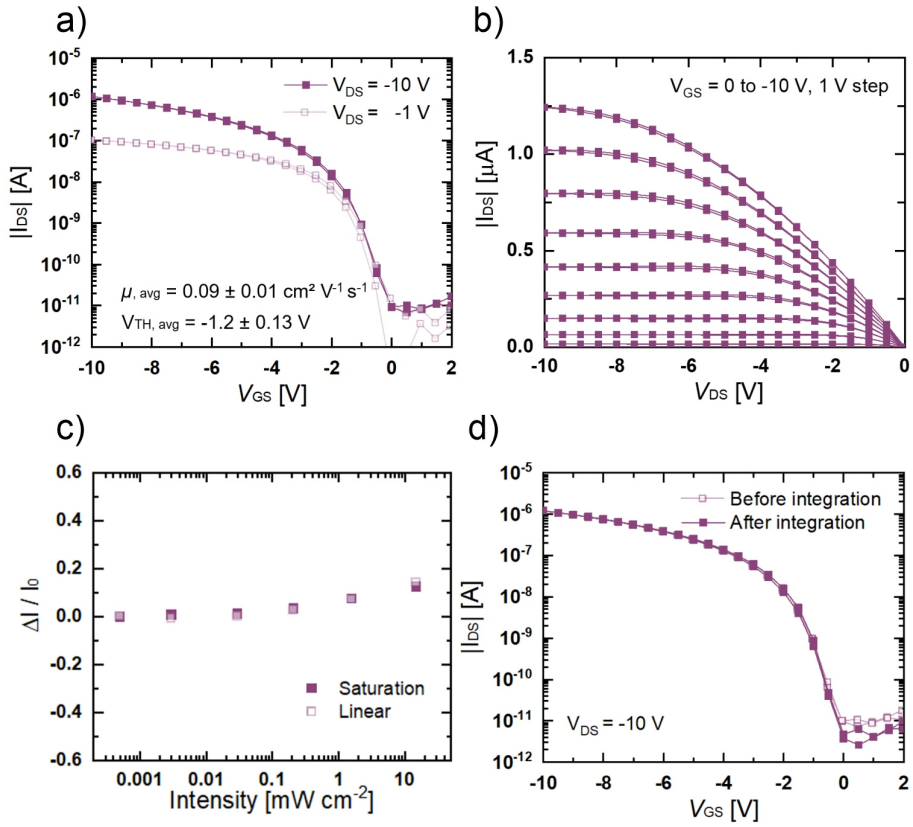

Figure 6.2 Characteristics of OTFTs Provided by POSTECH.
a) Transfer characteristics of the OTFT devices employed. b) Output characteristics of the OTFT devices employed. c) Relative change in current under illumination (λ= 520 nm) for the OTFT devices employed. d) Transfer characteristics of the OTFT devices before and after the OPD integration. The characterization of the individual OTFT devices was done by Dr. Sanghoon Baek. All panels of figure adapted from[13], CC-BY.

6.2.2 Design and Integration Approach for OPD-OTFT Pairs

In this section, the pixel design and methodology followed for the integration of the OPD-OTFT pairs is presented. **Figure 6.3a** shows the stack architecture of the integrated devices. In this case, a single substrate was used to deposit both the OPDs and OTFT devices. The substrate consists of a glass substrate coated with a parylene layer which can be detached upon completion of the fabrication process. The OTFTs are deposited first as described in Section 6.2.1. Their fabrication ends with the deposition of a top parylene layer to be used as interlayer and which serves as the base where the fully inkjet-printed OPDs are integrated. The device architecture of the fully-printed OPDs is the same as presented in Section 5.2 of Chapter 5. It consists of silver as the bottom-electrode, SnO_2 as

hole-blocking layer, P3HT:IDTBR as the BHJ-based active layer and PEDOT:PSS as the top, transparent electrode. The photodiode active areas are defined by the overlap of the bottom silver electrode and the top PEDOT:PSS electrode. **Figure 6.3b** shows a microscope photograph of an integrated OPD-OTFT pair. Here, it is possible to visualize the connection of the cathode of the OPD with the via hole that leads to the drain of the OTFT. During fabrication, the via-holes are created using a pulsed laser.

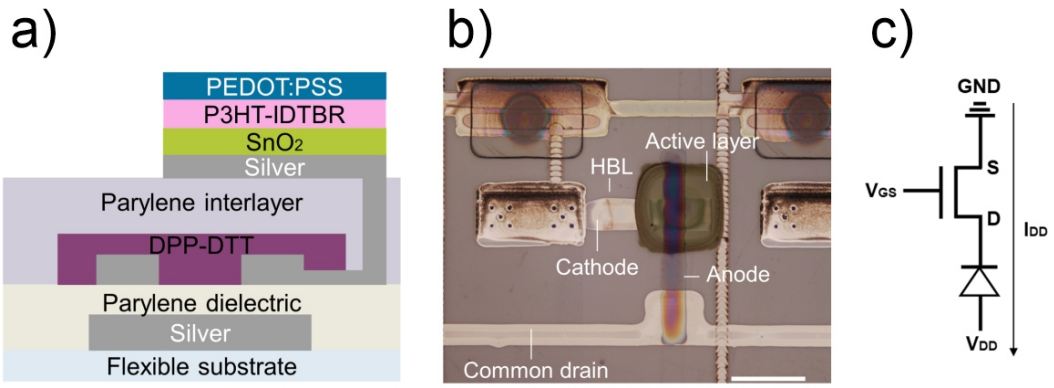

Figure 6.3 Design and Architecture of OPD-OTFT Integrated Devices.
a) Material stack of the OPD-OTFT integrated devices. The flexible substrate corresponds to parylene. b) Microscope image of the OPD-OTFT integrated devices (scale bar = 1000 µm). c) Schematic of the electric circuit of the integrated devices. All panels of figure adapted from[13], CC-BY.

The devices are connected in series and can be operated by applying the driving voltage (V_{DD}) and a gate to source voltage (V_{GS}), as depicted in **Figure 6.3c**. After integration, it is still possible to address the discrete components individually. In this case, the voltage V_{GS} and the voltage V_{DS} are used for the transistors and the voltage between anode and cathode (V_{diode}) is used for the photodiodes. Through the presented concept, we developed a 10×10 active matrix array where 100 OPD-OTFT pairs are integrated. This can be seen in **Figure 6.4a**, which shows a photograph of the developed matrix. Here, the anodes of all OPDs are connected to a common electrode (i.e. bit line), and their cathodes are connected to their matching transistors which act as dynamic switches. Similarly, the transistors are divided in rows, where each row connects their gates to a common electrode (i.e. world lines). This approach allows us to use the switching properties of the transistors in order to selectively retrieve the photocurrent from the OPDs of each pixel. Therefore, by applying a voltage that switches the transistors on and off, we can sequentially address row after row until we read the entire matrix[13]. A schematic of the fabrication process can be

seen in **Figure 6.4b**, where the sequence of layers forming the stack of both OTFTs and OPDs is shown to be monolithically deposited on a single substrate. The starting layers, (i) and (ii), represent the gate and top electrodes of the transistors. Subsequently, the layer deposition continues through the achievement of complete OTFT devices (iii), and follows with the deposition of the OPD layers, i.e. (iv) and (v), until the complete integration of full OPD devices connected to the transistors (vi). As it can be schematically seen in **Figure 6.4c**, once the inkjet-printed deposition is finished, the parylene-based matrix can be fully detached from its carrier glass-substrate resulting in an ultra-thin and flexible matrix with a total thickness <5 μm. This can be further appreciated in **Figure 6.4d**, which shows a photograph of a real matrix sample, highlighting its mechanical characteristics.

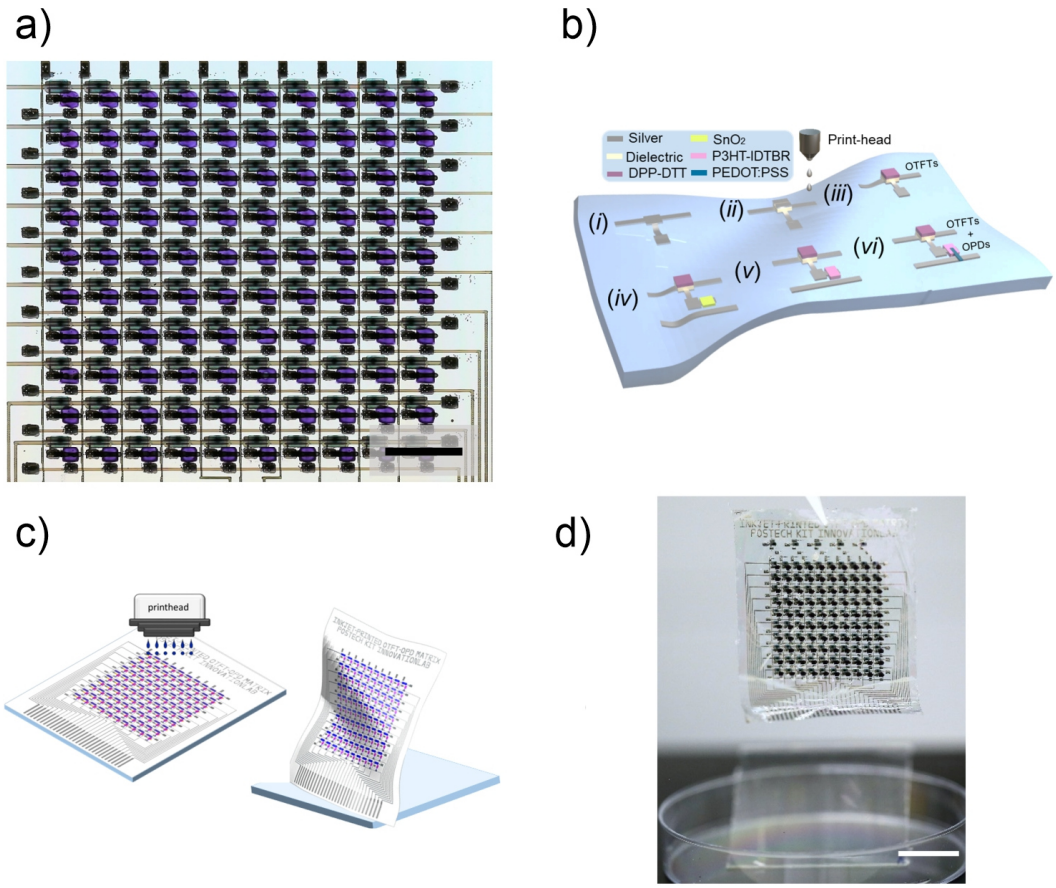

Figure 6.4 Fabrication of OPD-OTFT Integrated Matrix.
a) Photograph of matrix sample after integration (scale bar = 5 mm). b) Schematic of layer's deposition during the integration process. c) Schematic of the printing process and detachment of sample from carrier substrate. d) Photograph of the thin (<5 µm) and flexible integrated sample after detachment (scale bar = 20 mm). All panels of figure adapted from[13], CC-BY.

6.2.2.1 Solvent-Substrate Compatibility and Silver Optimization

The first step to address the monolithic integration was to investigate the process compatibility of the developed OPD stack with the OTFT stack. As mentioned before, the parylene interlayer that covers the OTFT devices represents the layer on which the OPDs are printed and is fundamental to avoid a degradation of the OTFTs after the processing of the OPDs. The interlayer has to be resistant to the different solvents employed in the ink formulations of the OPDs and it needs to provide a suitable surface in terms of surface energy and surface homogeneity for the deposition of the OPD stack. In this case, a redefinition of the printing parameters of the silver electrodes had to be explored to ensure

the compatibility of our OPD processing with this new substrate. This step is critical to the performance of the integrated devices since the quality of the silver electrodes influences the quality of all subsequent and preceding layers. In accordance with the OPD processing, the commercially available ink, Sigma-Aldrich TGME silver dispersion, was employed and deposited on parylene-covered glass substrates that have been treated with Argon plasma for 1 minute previous to silver deposition. After deposition the samples were annealed at 120°C for 10 minutes. **Figure 6.5a** shows an image of several test structures deposited on top of parylene. The squared structures shown here were deposited using various printing resolutions and sizes in order to find an optimally printed layer. The same trend seen with PEN in Chapter 5 is observed, namely, an excessively small drop spacing (DS), i.e. high dpi, will lead to a shapeless pattern with high ink agglomeration. In contrast, an excessively high DS, i.e. low dpi, will not allow the merging of the individual droplets and thus lose all possibility of achieving a conductive layer. **Figure 6.5b** shows microscopy images of the patterns with a printing resolution of 1270 (top), 461.82 (middle), and 141.11 dpi (bottom). As it can be seen, a test structure with a dpi of 461.82 shows an optimal deposition. This shows that the fabrication process developed for the OPD stack in PEN is also compatible with parylene. While this is of great benefit, it is important to keep in mind that this represents only the initial requirement for integration. The number of stacked layers and the scale of the system brings a much higher level of complexity to this processing as compared to the fabrication of individual devices. Particularly due to the requirement of achieving hundreds of devices where both compatibility and homogeneity of performance is critical.

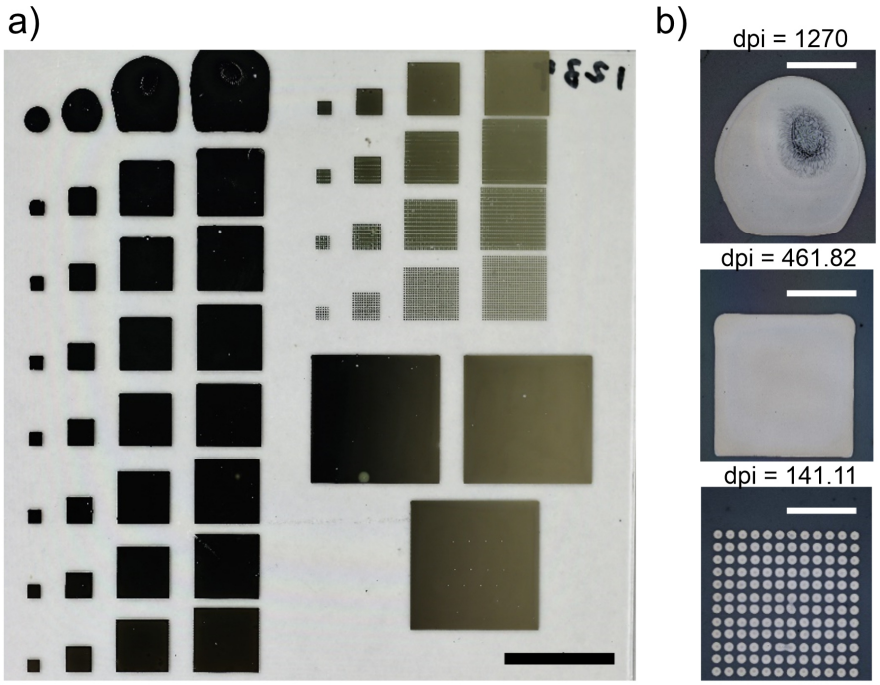

Figure 6.5 Silver Test Structures on Parylene.
a) Photograph of silver test structures printed in parylene at different resolutions and different sizes (scale bar = 4 mm). b) Microscope images of silver test structures printed at different resolutions (scale bars = 1000 µm).

During integration, the inkjet-printed silver was used not only to create the electrodes for the OPDs but also to form the physical connection between OTFTs and OPDs. **Figure 6.6a** shows examples of technical challenges that were encountered during fabrication. In some cases, the silver electrode would fail to achieve a connection through the via-hole to the OTFT devices (**Figure 6.6a**, left). In other occasions, a layer processing with successful connection will still be inadequate if the quality of the silver layer in terms of homogeneity and roughness was not sufficient, leading to issues in the morphology of the following layers as is depicted here for the case of the active layer (**Figure 6.6a**, middle). Therefore, the optimization of the printing process was critical for the achievement of uniform and high quality layers (see **Figure 6.6a**, right). Moreover, the reproducibility of the process for each OPD-OTFT pair was necessary and lead to a robust fabrication process (see **Figure 6.6b**).

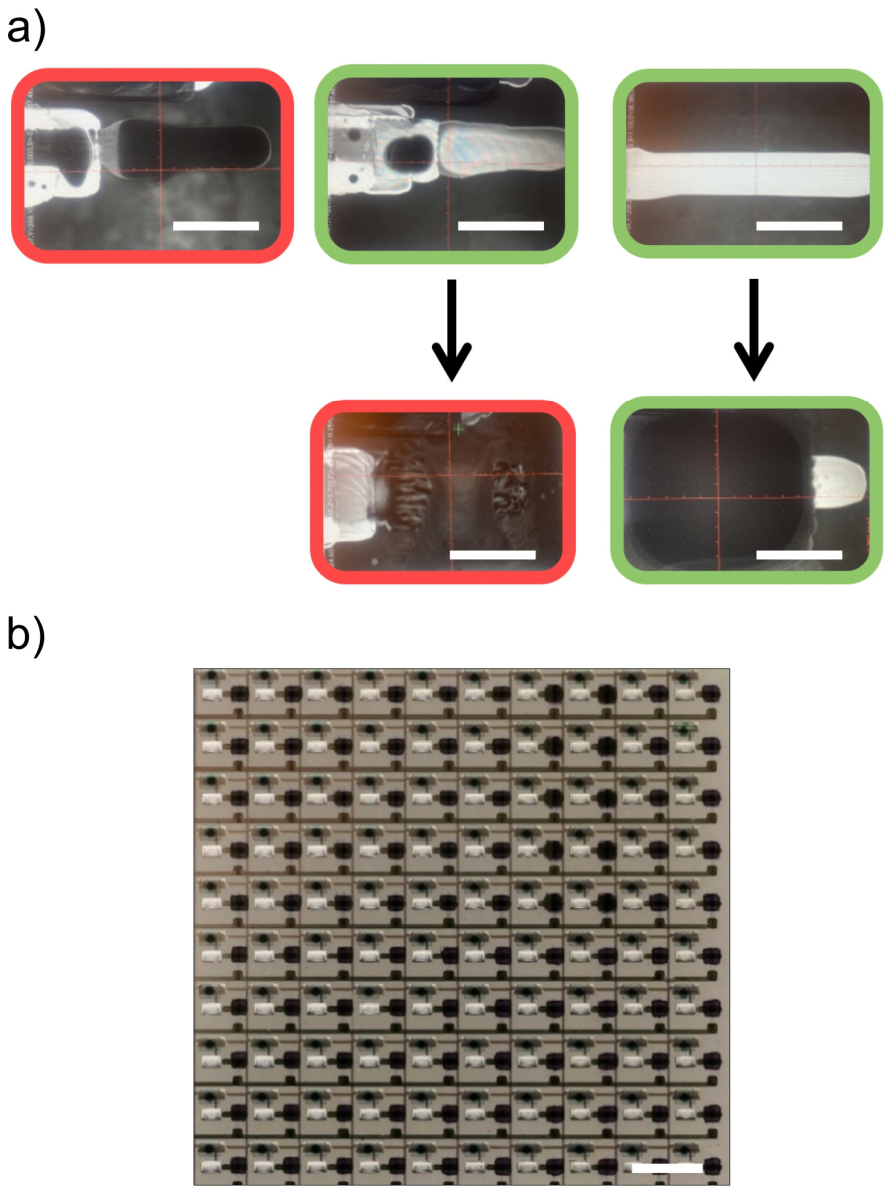

Figure 6.6 Examples of Printing Optimization During OPD-OTFT Integration.
a) Photographs of printed silver structures (left) and printed silver structures plus printed active layer structures (middle and right). Photos enclosed in red depict failed scenarios. Photos enclosed in green depict successful scenarios. The photos were taken using the printer's camera (scale bars = 500 µm). b) Top view photograph of matrix sample showing the successful fabrication process (scale bar = 4 mm).

6.2.3 Integrated Devices with Varied OPD Size

After the successful compatibility tests in terms of fabrication process, further compatibility tests in terms of the electrical characteristics of the OTFTs and OPDs were performed and are presented here. The objective was to find the best combination of OPD-OTFT pairs based on the output current of the devices. To this end, different samples containing the same OTFT design were processed with OPDs of different sizes. The OTFT layout remained unchanged because it was impractical to re-design and fabricate several backplanes of transistors with different layouts. On the other hand, the size of the deposited OPDs can be modified relatively easily by modifying their digital layout and adjusting the printing process accordingly. As mentioned before, their versatile design approach represents one of the advantages for this OPD design, which facilitates their integration with multi-device systems. In particular, the variation in OPD size was performed by adjusting their active area, as defined by the intersection of their top and bottom electrodes. Adjusting the dimensions of the active area of the OPD allows to tune the range of photoresponse of the OPD-OTFT pair. This happens because the output current of the integrated device is determined by the electrical characteristics of the independent components that are connected in series (see **Figure 6.3c** in Section 6.2.2). **Figure 6.7a-b** shows the transfer characteristics at $V_{DD} = -1\,V$ (i.e. in linear regime) of integrated devices with OPDs of active areas equal to 1.14 and 0.04 mm^2, respectively. These represent the largest and smallest OPD sizes studied. In the plots, the current between the OPDs' anode and the OTFTs' source (I_{DD}) is plotted against V_{GS}. In both cases the devices were measured in the dark and when illuminated with a monochromatic light at increased intensities and with $\lambda = 520$ nm. As it can be observed in both plots, the current I_{DD} increases with increasing light intensity due to the photodiodes response. In this case, the OTFT devices do not contribute to the current under illumination, as shown in the tests presented in **Figure 6.2c** of Section 6.2.1. Moreover, the difference between the values of I_{DD} in the dark and at maximum illumination (ΔI) is increased when the OPD size is decreased. This is attributed to the lower dark current of smaller OPDs which determines the lower limit of the response while the maximum current is limited by the transistors. By comparing the devices with OPDs of 1.14 mm^2 against the devices with OPDs of 0.04 mm^2, ΔI shows an increase of three orders of magnitude. The individual transfer characteristics of different OPD-OTFT pairs that were tested can be found in Figure A.2 of the appendix. The results are summarized in **Figure 6.7c** which shows a comparison of the relative change in photocurrent $\Delta I/I_0$, for all the

OPD-OTFT pairs tested. I_0 corresponds to the current in the dark of each device. Moreover, the area displayed represents the OPD size that was integrated in each case and V_{DD} corresponds to -1 V. By comparing the devices with OPDs of 1.14 mm^2 against the devices with OPDs of 0.04 mm^2, the results show a 70-fold difference in $\Delta I/I_0$ between them.

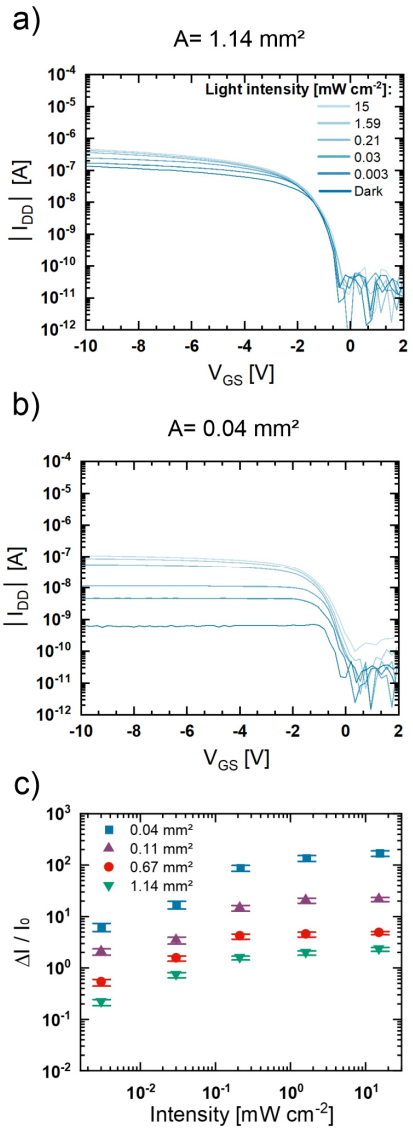

Figure 6.7 OPD-OTFT Integrated Devices with OPDs of Different Sizes.
a) Transfer characteristics of the integrated devices with V_{DD}= -1 V and with an OPD size of 1.14 mm^2. b) Transfer characteristics of the integrated devices with V_{DD}= -1 V and with an OPD size of 0.04 mm^2. c) Relative change in current against light intensity at V_{GS}= -10 V and V_{DD}= -1 V. for integrated devices with OPDs of various sizes. All panels in figure adapted from[13], CC-BY.

6.2.4 Performance of Integrated Devices as a Function of Driving Voltage

After studying the impact of OPD size in the functionality of the integrated devices, and in order to further optimize the performance of the integrated devices, their output as a function of their operational voltage was analyzed and is presented here. The objective was to find the best voltage to operate the devices in order to optimize their photoresponse and power consumption. **Figure 6.8a-b**, shows the transfer characteristics for the saturation (**Figure 6.8a**) and the linear regime (**Figure 6.8b**) at the fixed OPD size of 0.11 mm^2. In this case, when comparing the linear regime (V_{DD}= -1 V) against the saturation regime (V_{DD}= -10 V), an increase in the photoresponse can be appreciated, for example, by looking at ΔI, i.e., the difference between the values of I_{DD} in the dark and at maximum illumination. In particular, an increase of one order of magnitude in ΔI is achieved when switching from V_{DD}= -10 V to V_{DD}= -1 V. This increase occurs because, in the linear regime of operation, even small variations in voltage lead to significant increases in the output current of the devices, which leads to a higher relative change in current when compared to the saturation regime. In addition to this, the lower limit of the response is also influenced by V_{DD}, as OPDs have a lower dark current at lower V_{DD} values.

The individual transfer characteristics of different OPD-OTFT pairs that were tested can be found in Figure A.2 of the appendix. Measurement results for devices of all sizes are summarized in **Figure 6.8c**, which shows both the power and the relative change in current $\Delta I/I_0$ as a function of the driving voltage V_{DD}. In this case, the experiments were measured at a constant V_{GS} voltage of -10 V. As it can be seen, the power is higher for integrated pixels with higher OPD size, while the relative change in current $\Delta I/I_0$ shows the opposite effect being lower for integrated pixels of higher OPD size. Moreover, the effect is much more pronounced at lower V_{DD} bias. The analysis shows that lower driving voltages lead to an increased device response and to a drop in the consumed power. In specific, the relative change in current of the integrated devices with an OPD size of 0.04 mm^2, i.e. the smallest devices tested, is twelve times lower when the driving voltage is changed from -1 V to -10 V. In that same scenario, the power required increases by two orders of magnitude.

With respect to other studies found in literature where OPDs and transistors were also integrated, the devices presented in this chapter have a favorable drift from previous trends reported so far[13,139,141,142,144,151–154] as shown in **Figure 6.8d**. The plot shows the

sensitivity against power for pixels of integrated devices. The device sensitivity was defined as the slope of $\Delta I/I_0$ versus light intensity[13]. The sensitivity and power values of the devices were calculated by Dr. Sanghoon Baek. As it can be seen, the devices presented in this chapter cover a long range of power consumption values depending on the operational regime and in the size of the integrated devices employed, with a noticeable shift to increased sensitivity at decreased power consumption. In specific, the comparison of the integrated devices with an area of 1.14 mm^2 and 0.04 mm^2 shows an absolute difference of 50 nW when operated at -1 V, with power values of 100 nW and 50 nW, respectively. When operated at -10 V the change is of 9 µW against 350 nW for the devices of 1.14 mm^2 and 0.04 mm^2. Furthermore, as it can be seen, the device sensitivities achieved here are competitive with respect to the values found in the other studies. In particular, the tuning of the OPD size towards smaller active areas directed the sensitivity to higher values. Moreover, the values of power consumption in the µW-range correspond the lowest values reported until now.

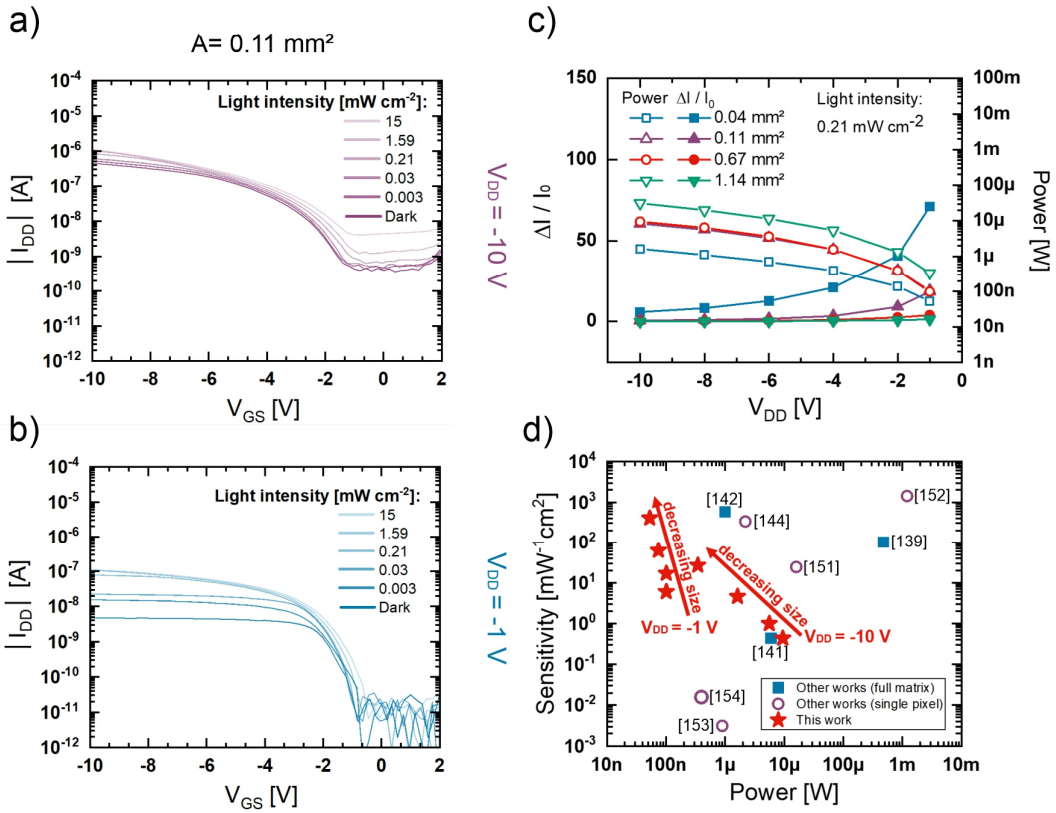

Figure 6.8 OPD-OTFT Integrated Devices at Different V_{DD} Values.
a) Transfer characteristics of the integrated devices with an OPD size of 0.11 mm^2 and with V_{DD}= -10 V. b) Transfer characteristics of the integrated devices with an OPD size of 0.11 mm^2 and with V_{DD}= -1 V. c) Relative change in current (left axis) and power (right axis) versus driving voltage for integrated devices with OPDs of different sizes. In this case, V_{GS}= -10 V. d) Sensitivity against required power for all the integrated devices from this work (V_{GS}= -10 V) as well as for other integrated devices found in the literature. Sensitivity and power values were calculated by Dr. Sanghoon Baek. All panels in figure adapted from[13], CC-BY.

6.2.5 Characterization of Optimal Integrated Devices

After studying different OPD-OTFT pairs with variations in OPD size and operational voltage, optimal integrated devices were determined and studied further in order to assess their capabilities for practical applications. The corresponding analysis is presented here. It is important to note that the optimal devices were determined not only based on their electrical characteristics but also in terms of their reproducibility within the fabrication process; since a uniform device performance is particularly important within a matrix of devices. For example, while OPD-OTFT pairs using an OPD size of 0.04 mm^2 showed the

best performance, as reported in **Figure 6.7** of Section 6.2.3, they also presented lower yields during their fabrication with values below 70%. In particular, inhomogeneous wetting during the printing deposition tended to have a more significant impact on the quality of their smaller electrodes resulting in formation issues such as those seen in Figure A.3 of the appendix. On the other hand, devices with OPDs of higher sizes were not significantly affected by these issues. Therefore, the integrated devices with an OPD size of 0.04 mm^2 were not selected for practical applications. Instead, the devices with an OPD size of 0.11 mm^2 were chosen. **Figure 6.9a** shows the distribution of current values measured for 100 OPD-OTFT pairs. In this case, the OPD size employed corresponds to 0.11 mm^2. The measurements were performed both in the dark and during illumination at λ= 520 nm, and correspond to the output current obtained at a V_{DD}=-1 V and a V_{GS}= -10 V. The average currents during illumination and in the dark correspond to 105±17 nA and 4.5±1.8 nA, respectively. This shows a good reproducibility for OPD-OTFT pairs using an OPD of 0.11 mm^2.

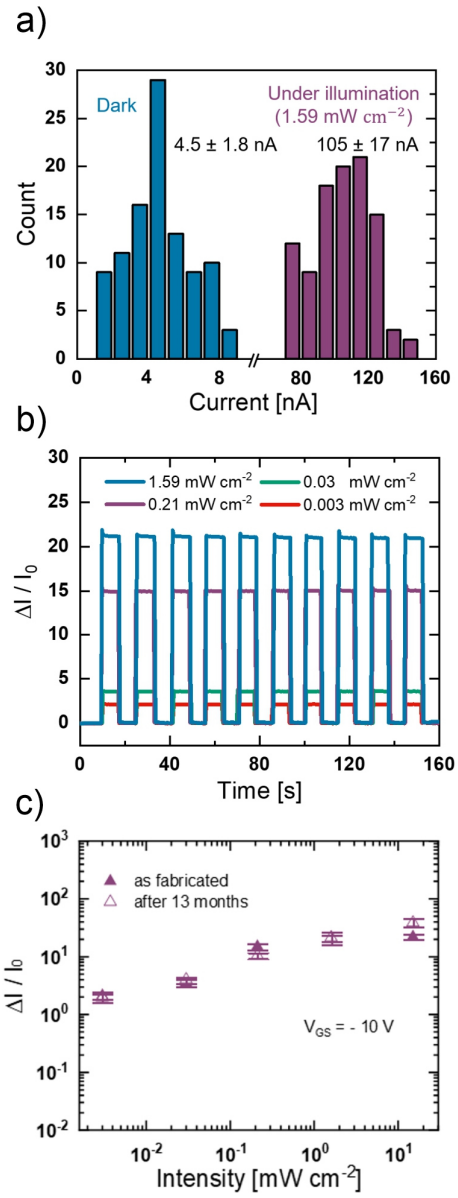

Figure 6.9 Performance of the OPD-OTFT Integrated Devices Forming the Active-Matrix.
a) Distribution of current values for 100 integrated devices. The devices were measured in the dark and under illumination. b) Dynamic current response at different light intensities. The current of the devices was measured in the dark and under illumination in real time. In each case, the light was turned on and off for periods of 10 seconds. The plot shows the relative change in current against time. c) Comparison of performance between the devices presented in Figure 6.8b and devices stored for 1 year and one month inside a glovebox. All devices correspond to integrated devices with an OPD size of 0.11 mm^2. All panels in figure adapted from[13], CC-BY.

Moreover, in order to test the adaptation of the devices to real-time changes in illumination, their output current was measured continuously while a monochromatic light source of λ= 520 nm was switched on and off to alternate between 10 seconds of illumination and 10 seconds of dark conditions. The process was repeated for each light intensity, namely, 0.003, 0.03, 0.21 and 1.59 mW cm^{-2}. The results, presented in terms of the relative change in current against time, are shown in **Figure 6.9b**. In this case, the voltages were fixed at V_{GS}= -10 V and V_{DD}= -1 V. The devices showed a clear and steady photoresponse to all the different light intensities. Moreover, once the light source was turned off, the response was easily reversed to its original value in dark conditions. As it can be seen, this process can be repeated multiple times without affecting the performance of the devices, highlighting their reliability and durability. Finally, **Figure 6.9c** shows the relative change in current in the linear regime and V_{GS}= -10 V, at different light intensities, of the samples with an OPD size of 0.11 mm^2 (values extracted from **Figure 6.8b**) and compares them to the results obtained for samples that were measured after one year and one month of storage inside a N_2-filled glovebox. The results show that the samples have a good stability with no visible degradation in performance. The complete transfer characteristics of the devices measured can be seen in Figure A.4 of the appendix.

6.2.5.1 Figures of Merit of the OPDs Used in the Optimal Integrated Devices

In the previous sections, the optimal integrated devices were determined to contain OPDs with an active area of 0.11 mm^2. This section presents the characterization of the OPDs with an active area of 0.11 mm^2. Since the main interest lies on the performance of the devices after undergoing the integration process, measurements were performed on OPDs that were already integrated into an OPD-OTFT pixel and were measured individually as discrete components. After integration, it is still possible to address the discrete components individually. The OPDs were addressed individually by contacting the anode and the cathode of the OPDs (i.e. V_{diode}). Moreover, to be able to perform the characterization of the SR, detection speed, and noise for the OPDs, a unique sample design was used (see Figure A.5 of the appendix). In this case, the contact pads of the sample were designed based on the specifications of the sample-holder used in the corresponding probe stations. The design rules used to fabricate the devices of this sample remain the same as those presented in all other integrated devices.

Figure 6.10 shows the steady-state and dynamic characteristics of the OPD devices with an active area of 0.11 mm^2. The J-V characteristics are shown in **Figure 6.10a**. The plot

shows the dark current as well as different currents measured under illumination using a green LED (λ= 520 nm) with a maximum optical power of 15 mW cm^{-2}. At the representative bias voltage of -2 V, the average dark current from ten devices show values of 0.71 ± 0.07 µA cm^{-2}. **Figure 6.10b** shows the current density of the devices against different optical powers at -2 V. As it can be seen, the devices show a good performance with an estimated LDR value of 89 dB.

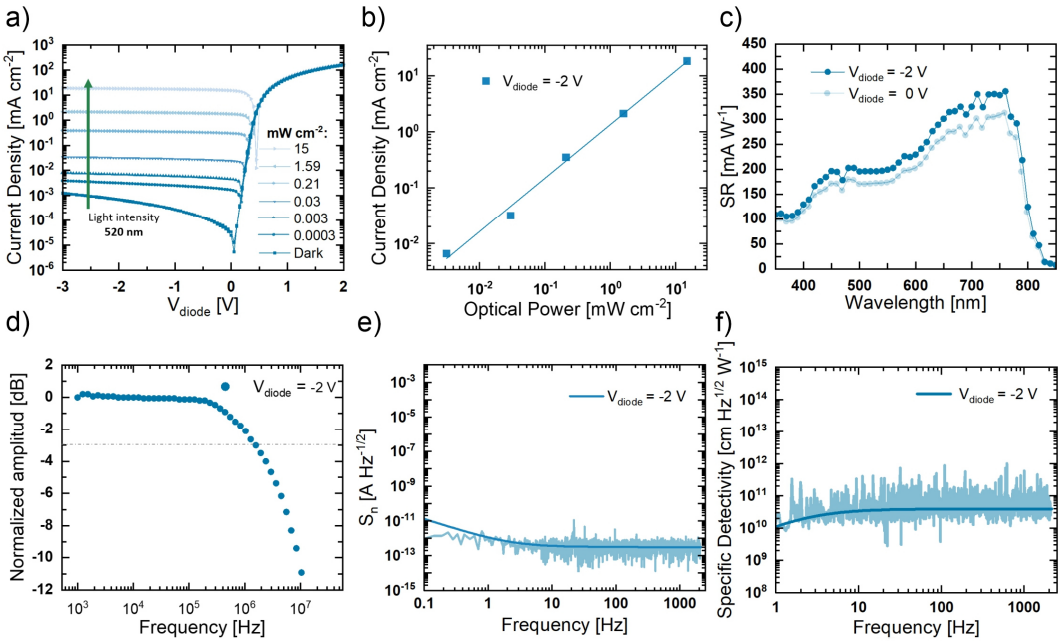

Figure 6.10 Characteristics of OPDs with a Size of 0.11 mm^2.
a) J-V curves measured in the dark and under illumination (λ= 520 nm). b) Current densities at different optical powers at -2 V. LDR= 89 dB. c) SR measurements at 0 and -2 V. d) Bandwidth measurements at -2 V. e) Spectral noise density at -2 V. f) Specific detectivity at -2 V. The noise spectral density measurement is used for the calculation of the detectivity. A python module developed by Dr. Mervin Seiberlich was used to process the data of the spectral noise density and the specific detectivity. All panels in figure adapted from[13], CC-BY.

Figure 6.10c shows the SR performance at different voltages. In general, the measurements show the expected broad-band profile based on their photoactive layer with a broadband response from 350 to 850 nm. Moreover, at the representative voltage of -2 V the peak value at λ= 760 nm corresponds to 356 mA W^{-1}. This corresponds to an increase of 44 mA W^{-1} when compared to the measurements performed at 0 V, where the peak

value was 312 mA W^{-1}. This increase in SR is caused by the enhanced charge carrier extraction coming from the increment in bias voltage.

Figure 6.10d depicts the frequency response at -2 V. At this representative voltage, the f_{-3dB} has a value of ~1.5 MHz showing an excellent performance which makes them suitable for many useful applications including those requiring high detection speeds.

Finally, **Figure 6.10e** and **Figure 6.10f** show the noise spectral density and specific detectivity of the devices, respectively. The noise spectral density measurement is used for the calculation of the detectivity D^*. A python module developed by Dr. Mervin Seiberlich was used to process the data of the spectral noise density and the specific detectivity. In this case, the calculated D^* shows a maximum value of 3.9×10^{10} Jones at -2 V.

In summary, the OPDs used in the integration of the OPD-OTFT pairs show a good performance in all their figures of merit, with similar characteristics to other high-performing OPDs found in literature[14,33–35,55,56,111,156,157].

6.2.6 Assessment of Integrated Devices for Wearable and Advance Light-Monitoring Applications

In order to test if the devices are suitable for real-life wearable applications, their performance was measured at different bending radiuses, namely, 0, 5, 10 and 50 mm. These radiuses are comparable to the bending levels that the sample would undergo when placed on a person's arm, hand or finger. The results can be observed in **Figure 6.11a**. which shows the relative change in current of bent samples at different illuminations. The inset of the figure exemplifies the measurement procedure by showing a schematic of a sample being placed on a test structure with a pre-defined bending radius. During the measurements, a monochromatic light source (λ= 520 nm) was used for illumination. As it can be seen, the devices showed insignificant change in current, specifically, <1% change in current when compared to the flat reference measurement. **Figure 6.11b** shows a photograph of the real sample. As it can be seen, the sample conforms easily around a finger. In this regard, one example of a practical application is photo-plethysmography (PPG) measurements which are widely used for health monitoring. A schematic of the measurement, performed in transmission mode, can be seen in **Figure 6.11c**, where the light out of an LED goes through a finger and into the sensor. The sensor then absorbs part of the received light and generates a current response which can be used to estimate the pulse of a person. The LED employed in this case has a wavelength of 640 nm. **Figure**

6.11d shows the results of the pulse measurements where the signal versus time was recorded. Different pixels were tested and operated either in the linear or saturation regime. In both operation regimes the signals show pulse patterns. However, the signal with more distinguishable peaks is observed under the linear regime due to the enhanced response of the devices in this regime. In this case, a heartbeat of approximately 67 bpm was obtained.

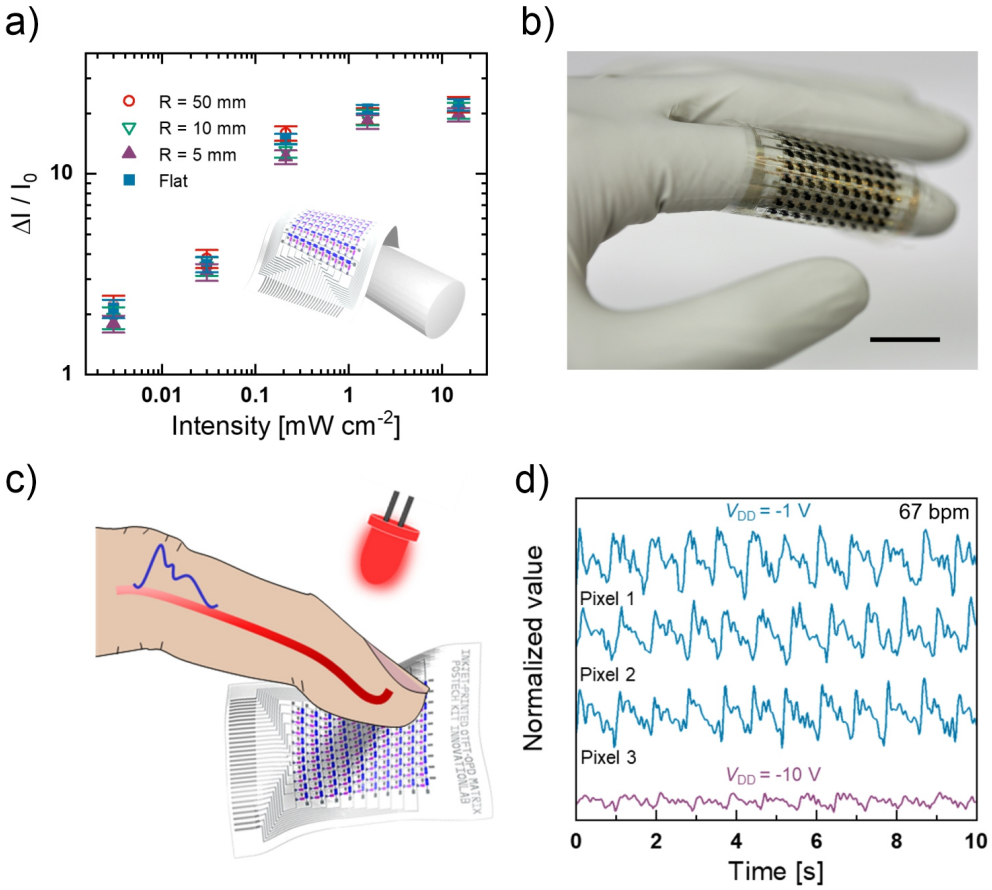

Figure 6.11 Assessment of OPD-OTFT Integrated Devices for Wearable Applications.
a) Photoresponse measurements under mechanical stress performed at different radiuses (R) where the relative change in current is plotted for different light intensities (λ= 520 nm). The radiuses were pre-defined by using test structures of fixed R as schematically shown in the figure inset. b) Photograph of a real sample placed around a finger (scale bar= 2 cm). c) Schematic representation of transmittance mode PPG measurement. d) Signals from pulse measurements in the linear and saturation regimes. A LabVIEW script written by M.Sc. Kai Xia was used to record the real-time signals during the PPG measurements. Panels a), c) and d) adapted from[13], CC-BY.

Finally, to demonstrate the application potential of the 10×10 flexible arrays reported in this work, static and dynamic demonstrations of the sensor matrix were performed and are presented here in the following. **Figure 6.12a** shows a schematic of the static demonstration. The static demonstration was performed with the sample still attached to a glass substrate for it to remain in a flat condition. During the experiment, a green LED with λ= 520 nm and an intensity of 1.59 mW cm^{-2} was used for illumination. Moreover, a patterned mask was placed on top of the sample to define the areas being illuminated. The mask layout contains three holes in the shape of geometrical figures, namely, a rectangle, a cross and a triangle. The light from the LED can only pass through these geometrical openings. In this manner, a set of exposed and covered pixels is defined (see **Figure 6.12b**). Thus, based on their location under the mask, pixels yield different output currents during the measurement. The output currents, at V_{GS}= -10 V and V_{DD}= -1 V, of the one hundred pixels forming the matrix were recorded. The relative change in current for each pixel is shown in **Figure 6.12c**. Here, the colors in the map indicate the variations in light response in the matrix. In specific, a contrast in relative change in current over three orders of magnitude was obtained between exposed and covered pixel areas. Finally, as it can be observed, the responses measured within the matrix successfully replicate the expected patterns proving that spatial mapping can be achieved with this matrix.

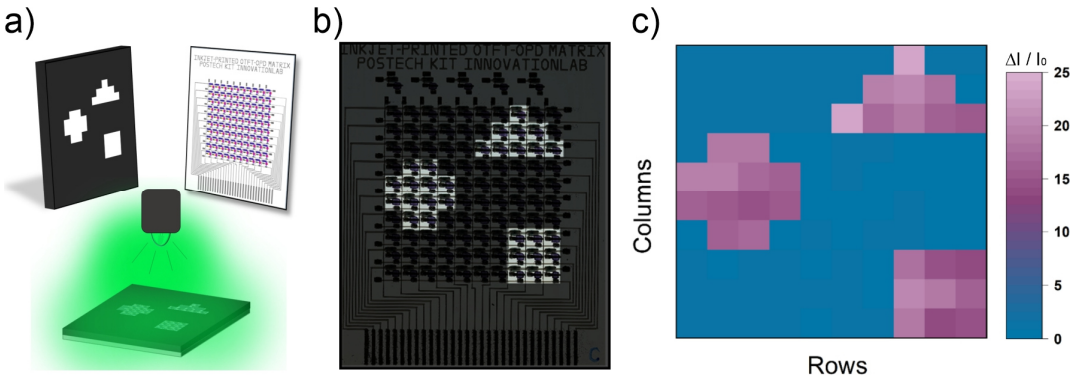

Figure 6.12 Matrix Static Demonstration.
a) Schematic representation of the mask, matrix sample and illumination process. b) Photograph of a real sample covered by a schematic of the mask in order to show the covered and exposed pixels. c) Output response for each pixel forming the complete matrix. The response from each pixel is presented by their relative change in current (V_{GS}= -10 V, V_{DD}= -1 V). The variations in response between pixels are indicated by the variations in color. Panels b) and c) adapted from[13], CC-BY.

The dynamic demonstration was performed in a curved surface with a radius of 10 mm. The chosen curvature was meant to imitate the mechanical conditions experienced by a matrix sample when placed over the hand of a person to act as a wearable device. This is exemplified in **Figure 6.13a**.

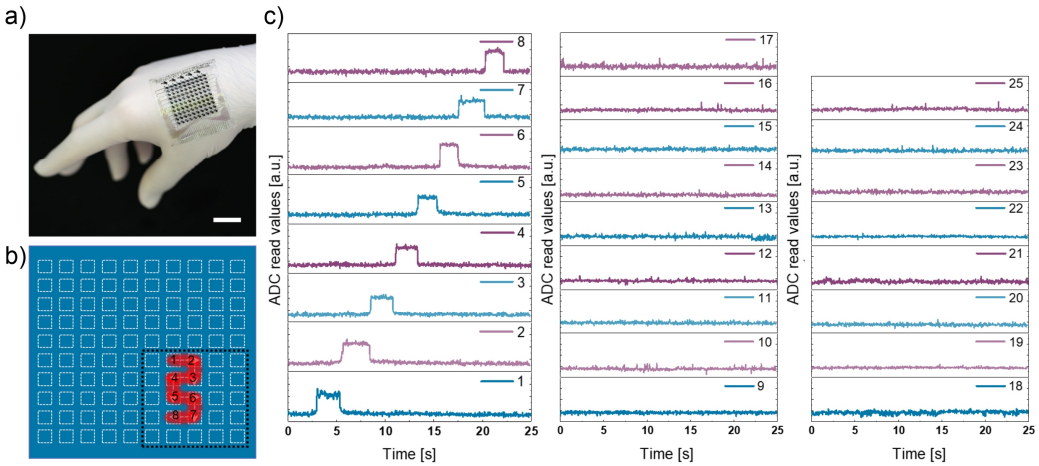

Figure 6.13 Matrix Dynamic Demonstration.
a) Photograph of a matrix sample conforming to a hand (scale bar= 2 cm). b) Schematic showing the dynamic light path across the matrix. The measurement was performed in a region containing 25 pixels as shown by the dotted rectangle. The point light source was displaced over eight different pixels as indicated in the diagram. c) Matrix current response obtained in real-time from the 25 pixels employed. The readout electronics employed in this measurement was provided by Prof. Sung-min Park from POSTECH. Panels b) and c) adapted from[13], CC-BY.

To illuminate the sample during the measurement, a laser pointer of λ= 640 nm was moved across the sample in different directions, hitting only one pixel at the time. **Figure 6.13b** shows the path followed by the laser pointer. As it can be seen, 8 different pixels were illuminated during the measurement. Moreover, the diagram shows a total of 25 pixels enclosed by a dotted rectangle. This corresponds to all the pixels recorded during the dynamic measurement and is defined by the maximum number of pixels that can be simultaneously addressed by the readout electronics employed during the measurements. The readout electronics was provided by Prof. Sung-min Park from POSTECH. In specific: "The spatial mapping of the matrix for the dynamic demonstration was done using custom-built readout electronics by measuring the current of each pixel. Signals were collected via analog-to-digital converters (ADC) and processed using MATLAB. More specifically, we have used a 115200 bps-UART and 12-bit-ADC chip for the scanning electronics. The

electronics scans the selected 5 × 5 square grid in the array at 30 Hz (30 frames per second), and the signals at each pixel were recorded at 30 Hz. As we used one ADC for the array, the ADC collected signals at 750 Hz (30 Hz × 25 pixels). The biases used are V_{GS} = −10 for a word line, and V_{DD} = −10 V or −1 V for a bit line."[13].
Finally, **Figure 6.13c** shows the signals recorded in real-time in the 25 pixels employed. In this case, the data was obtained at V_{GS}= -10 V and V_{DD}= -1 V. The recorded signals demonstrate that the light path can be successfully followed with the matrix.

In summary, the static, dynamic and bending demonstrations presented here prove the suitability of the developed matrix for practical light-sensing applications including those requiring spatial mapping, light monitoring or mechanical flexibility.

6.3 OPD Integration to InnovationLab GmbH Backplane

This section presents the integration of the fully-inkjet printed OPDs into the backplane of OTFTs developed by InnovationLab GmbH in the framework of the 2-HORISONS BMBF project. The design and integration approach followed as well as the characteristics of the individual sensor elements are introduced. Then, the integrated devices, their characteristics and the complete matrix are presented.

6.3.1 Layout and Characteristics of OTFT Devices Used for Integration

In this section, the matrix of transistors provided by InnovationLab GmbH is described. In addition, the individual characteristics of the OTFT devices forming the matrix backplane are presented. The fabrication of the OTFT matrix was done by Sebastian Raths from BASF and by Dr. Karl-Philipp Strunk, Dr. Stefan Schlisske, M. Eng. Benjamin Obermajer and Manuel Seifert from InnovationLab GmbH. The design of the integration layout was done in collaboration with Dr. Karl-Philipp Strunk and Dr. Stefan Schlisske with contributions from all three participants. The OTFT stack used in the matrix layout can be seen in **Figure 6.14a**. BASF possess proprietary ownership of the materials used as OTFT dielectric layer and organic semiconductor. The material employed as interlayer dielectric was SU-8 and was used as a base to deposit the OPD layers. The metallic electrodes correspond to gold. The OTFT devices are fabricated by thermal evaporation of gold on top of PEN, forming the source and drain of the devices. The semiconductor material is then inkjet printed to define the active area of the transistors. Subsequently, a first dielectric layer is spin-coated

on top to function as the OTFT dielectric material. This is followed by a second gold pattern that forms the gate electrodes of the transistors. Finally, an SU-8 dielectric layer is deposited on top to be used as interlayer for the integration of the fully inkjet-printed OPDs. The structure of the metallic contacts and the via-holes employed to connect the OPD-OTFT pairs was done via photolithography. The transfer characteristics of the OTFT devices are shown in **Figure 6.14b**. At V_{DS}= -10 V, the devices have an on-current (I_{DS}) and an off-current (I_{OFF}) of ~11 µA and ~65 pA, respectively.

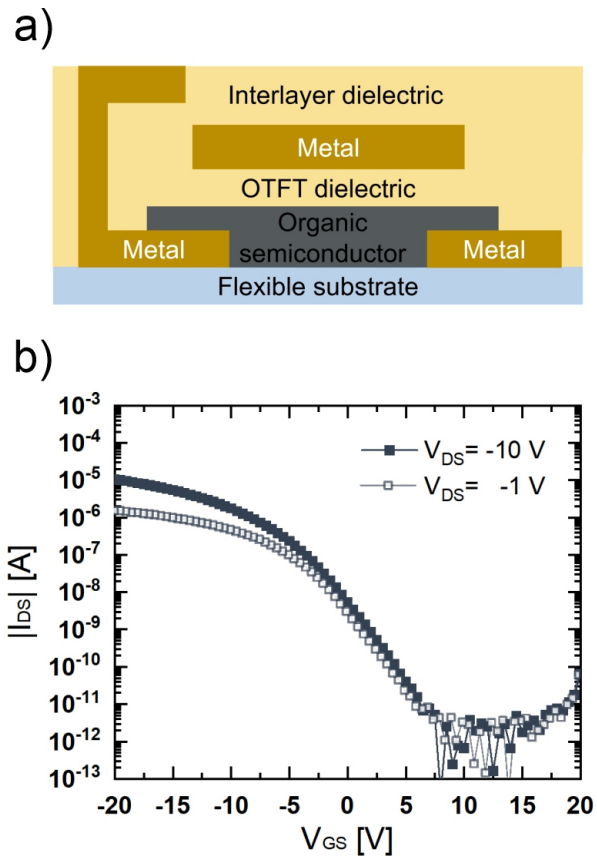

Figure 6.14 Design and Characteristics of OTFTs Provided by InnovationLab GmbH
a) Material stack of the OTFT devices employed. The flexible substrate corresponds to PEN. The fabrication of the OTFT matrix was done by Sebastian Raths from BASF and by Dr. Karl-Philipp Strunk, Dr. Stefan Schlisske, M. Eng. Benjamin Obermajer and Manuel Seifert from InnovationLab GmbH. The design of the integration layout was done in collaboration with Dr. Karl-Philipp Strunk and Dr. Stefan Schlisske. b) Transfer characteristics of the OTFT devices employed.

6.3.2 OPD-OTFT Integration

In this section, the pixel design and methodology followed for the integration of the OPD-OTFT pairs is presented. **Figure 6.15a** shows a microscope image with six OPD-OTFT pairs after the OPDs were integrated by inkjet printing. In this case, the size of the via-hole that connects the OPDs and OTFTs has been adapted to pre-define the active area of the OPDs. This allows to use gold as the bottom electrode of the OPDs as a replacement for silver. Since gold is readily a component of the OTFT stack, the bottom electrodes of the OPDs can be incorporated into pre-existing processing steps, therefore simplifying the fabrication process by eliminating one printing step. Except for the replacement of silver by gold, as bottom electrode, the device architecture of the fully-printed OPDs is the same as presented in Section 5.2 of Chapter 5. The bottom electrode is followed by SnO_2 as hole-blocking layer, P3HT:IDTBR as the BHJ-based active layer and PEDOT:PSS as the top, transparent electrode. The size of the active area of the OPDs is defined by the overlap of the gold and PEDOT:PSS electrodes and corresponds to 0.06 mm^2. By using photolithography to pre-define the active areas, smaller OPD footprints can be achieved without issues in the fabrication process. **Figure 6.15b** shows a photograph of the full matrix of integrated devices where a total of 1024 OPD-OTFT pairs was achieved. In order to measure the complete matrix, a read-out electronics is required. However, the optimization of the internal software needed to control the read-out electronics was not possible due to project delays related to COVID and other unforeseen circumstances. Therefore, measurements of the complete matrix could not be performed. Nevertheless, it was still possible to address the OPD-OTFT pairs individually to confirm the functionality of the integrated devices. **Figure 6.15c** shows the transfer characteristics of the OPD-OTFT integrated devices at V_{DD}= -10 V. Due to the small OPD size, low dark currents can be achieved in the integrated devices. At V_{GS}= -20 V, the measured dark current I_0 corresponds to 38 pA.

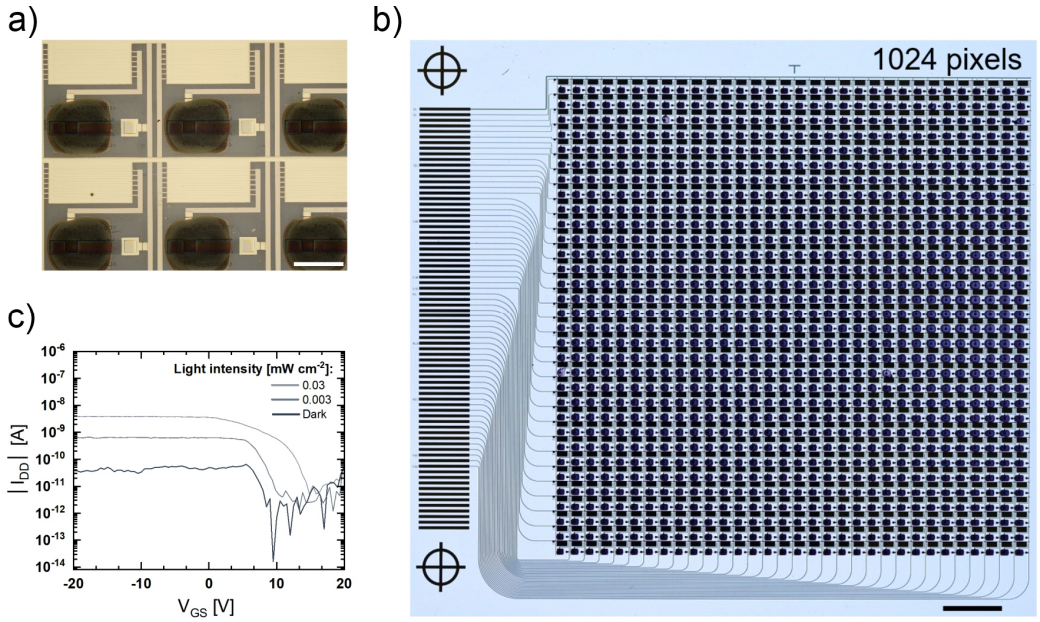

Figure 6.15 OPD-OTFT Integrated Devices
a) Microscope image showing six OPD-OTFT integrated devices (scale bar = 1000 µm). The fabrication of the OTFT matrix was done by Sebastian Raths from BASF and by M. Eng. Benjamin Obermajer and Manuel Seifert from InnovationLab GmbH. The design of the integration layout was done in collaboration with Dr. Karl-Philipp Strunk and Dr. Stefan Schlisske. b) Photograph of matrix sample after integration (scale bar = 1 cm). c) Transfer characteristics of the integrated devices with V_{DD}= -10 V and with an OPD size of 0.06 mm^2.

6.4 Summary

In this chapter, the integration of fully inkjet-printed OPDs with different matrices of transistors was investigated. The OPDs were monolithically integrated into two different OTFT technologies, provided by two different project partners, the group of Prof. Sungjune Jung from POSTECH in South Korea, and InnovationLab GmbH in Germany. The first step to address the integration was to investigate the process compatibility between the developed OPD stack and the OTFTs. For this, an optimization in terms of matrix design and integration approach was necessary for each OTFT technology. The layout design, the solvent's compatibility and the optimization of the printing process were addressed resulting in uniform and high-quality layers as well as high performing devices. With POSTECH's OTFT backplane, the developed matrix consists of 100 OPD-OTFT pairs integrated in an ultrathin and flexible substrate, where each OPD-OTFT pair is composed of more than 10 functional layers.

As part of the investigation, compatibility tests in terms of the electrical characteristics of the OTFTs and OPDs were performed by processing different samples with a fixed OTFT design but with OPDs of different sizes. This was possible thanks to the versatile design approach of the inkjet printed OPDs and allowed to find the best combination of OPD-OTFT pairs as well as to optimize their photoresponse as integrated devices.

Subsequently, the integrated devices were optimized further by analyzing their output as a function of their operational voltage. This allowed to find the best voltage to operate the devices and to optimize further their photoresponse as well as their power consumption.

The results showed that the tuning of the OPD size towards smaller active areas lowered the power consumption below the µW-range and directed the sensitivity of integrated devices towards higher values, achieving one of the highest sensitivity values found in the literature for all-organic integrated sensors. Thereafter, the optimal integrated devices were determined and studied further in order to assess their capabilities for practical applications. In this regard, the devices were subjected to dynamic current measurements under alternating illumination, to measurements under mechanical stress at different bending radiuses and, were also applied to perform PPG measurements. The results demonstrated their reliability and durability as well as their suitability for real-life wearable applications. Finally, to demonstrate the application potential of the 10×10 flexible arrays reported in this work, static and dynamic demonstrations of spatial light sensing were performed successfully using the sensor matrix. Moreover, with InnovationLab

GmbH OTFT backplane, the integration was tested in matrices of larger areas with an increased number of devices. In this case, the successfully developed matrix consists of 1024 OPD-OTFT pairs integrated in a thin and flexible substrate.

Based on the achievements of the OPD integration with both OTFT technologies, this chapter presents a process capable to integrate stacks of up to 10 functional layers and up to 1024 OPD-OTFT pairs based on the inkjet printing of OPDs. Additionally, both OPDs and OTFTs showed a high performance that remained unchanged despite undergoing the integration process. Looking ahead, the presented work is expected to facilitate the use of optoelectronic devices in next-generation applications, particularly those where the advantages of organic electronics such as mechanical flexibility, high freedom of design and high performance are needed.[e]

[e] *Parts of this chapter have been previously published in the journal npj flexible electronics under the free creative-commons license* (CC-BY) *([13]).*

7 Semi-Transparent Inkjet Printed OPDs with NIR Photoresponse

The past two chapters focused on the development and integration of OPD devices based on an innovative OPD stack that employed the broad-band BHJ material P3HT:IDTBR as active layer. In this chapter, a new BHJ system that focuses in the near infrared (NIR) part of the spectrum is investigated. The ink formulation, device architectures and fabrication processes are described. Moreover, the main figures of merit are depicted and compared between the different device architectures. Finally, a demonstration of the OPD devices is presented in terms of a practical application.

7.1 Introduction

A prevalent trend in OPD technology involves its close alignment with the advancements of organic solar cells (OSCs). In the past, most OPD devices were therefore designed with light detection in the visible range, following the focus of material development for OSCs. However, after the introduction of a new family of materials known as non-fullerene acceptors (NFAs), the development of new materials for OSCs accelerated and diversified. An example of this new class of materials is the NFA O-IDTBR. As seen in Chapter 5 and Chapter 6, this material can be used in combination with the donor polymer P3HT to achieve high-performing OPD devices with a photoresponse that extends into the NIR; and it has also been originally found as one of the most successful material combinations for next-generation OSCs[61–63]. However, even if the response of O-IDTBR extends into the NIR, it still has a relatively strong response in the visible range, and when combined with P3HT the resulting BHJ (P3HT:IDTBR) remains an active layer system with broad-band absorption covering a large wavelength-range from 350 to 850 nm. More recently, the design flexibility of NFA materials fueled the design of new chemical structures with absorptions that extend further into the NIR range[158–171]. This has opened new possibilities for the fabrication of innovative OPD designs with focus on light detection outside of the visible spectrum. Photodetectors that can selectively detect NIR light are particularly advantageous in areas such substance-authentication[17,172–174], health monitoring[175–178] and light communication[179]. Additionally, NIR-absorbing materials have the potential to be engi-

neered into semi-transparent devices[180–185] which can be used in advanced applications such as smart-windows[158,186,187], retinal implants[188] and touchless interfaces[189]. Furthermore, as introduced in Chapter 5, a key factor to enable the large-scale production of OPDs lies on their fabrication via digital printing techniques such as inkjet printing. In this manner, the significant advantages of inkjet printing such as design flexibility and precise resolution, can be applied to fabricate high-performing OPDs and multi-device systems; like those presented in Chapter 6. However, the process of developing inkjet-printable inks is complex. As a result, the available active layer combinations suitable for inkjet-printing are limited. Given that the active layer material governs the range of the device's response, it would be greatly beneficial to develop new inks for active layer materials, thereby opening new possibilities for practical applications.

In this chapter, a new BHJ system for inkjet printed NIR OPD devices is presented. The new ink formulation is based on the NFA known as 2,2′-((2Z,2′Z)-((12,13-bis(2-ethylhexyl)-3,9-diundecyl-12,13-dihydro-[1,2,5]thiadiazolo[3,4-e]thieno[2″,3″:4′,5′]thieno[2′,3′:4,5]pyrrolo[3,2-g]thieno[2′,3′:4,5]thieno[3,2-b]indole-2,10-diyl)bis(methanylyli-dene))bis(5,6-dichloro-3-oxo-2,3-dihydro-1H-indene-2,1-diylidene))dimalononitrile (BTP-4Cl), a chlorinated small molecule NFA based on a dithienothiophen[3.2b]-pyrrolobenzothiadiazole (TPBT) core structure[168]. BTP-4Cl which has NIR absorption, is used in combination with the transparent polymer known as polyindenoflurorene-8-triarylamine (PIF8-TAA). PIF8-TAA is a triarylamine copolymer derivative used as donor material. Upon thin-film deposition it is a semi-transparent material with limited absorption in the visible range[14]. Due to its high stability to ambient air and suitable charge-carrier mobility[72,190], it has been previously employed as a p-type material in transistors[191], and as a hole-transport layer in solar cells[192]. Only until recently it was considered as a donor material in photodetectors for selective red- and blue-light detection when used with the acceptors ITIC-4F and IDFBR[14]. In the work presented in this chapter, the thoughtful selection of the appropriate donor and acceptor components yields a semi-transparent active layer exhibiting high transmittance in the visible range with an effective photoresponse focused in the NIR part of the spectrum. At first, the capability of the new BHJ system is investigated in spin-coated devices. Subsequently, the ink formulation and characterization of the active layer is presented in terms of its suitability for inkjet printing. Then, the inkjet printed active layer is employed to fabricate OPD devices that can be compared to the spin-coated references. Moreover, different device architectures are designed and fabricated aiming to expand the application of the new BHJ from opaque to

semi-transparent devices (i.e. visible transparency comprising the complete OPD-stack). Finally, as a demonstration, the promising features of the developed devices are presented via PPG measurements.

7.2 Feasibility Study and Reference Performance for PIF8-TAA:BTP-4Cl

In the following, the BHJ material system developed, and tested for its application in NIR OPDs, is presented. The functionality of the BHJ system was determined during the analysis of samples fabricated with spin-coated active layers. This allowed for an efficient screening of the material system before undergoing the complex adaptation into an inkjet printed process. Additionally, a definition of reference performances was achieved through experimental measurements of the main figures of merits of the spin-coated OPDs.

7.2.1 Materials, Architecture, Design, and Fabrication

In this section, the materials used to form the active layer system, the OPD architecture employed for the reference devices, as well as the fabrication process that was followed are introduced. **Figure 7.1a** shows the chemical structures of the materials employed. The small molecule BTP-4Cl is soluble in common organic solvents such as chlorobenzene (CB), and has an absorption dominated by the NIR part of the spectrum, from 600 to 900 nm, with its peak at 746 nm[168]. Thanks to its extended absorption, practical solubility, and low bandgap, it has been used to fabricate high performing OSCs with broader photo-response and improved efficiencies[158,168]. Moreover, a few examples of OPD devices containing BTP-4Cl also exist[193,194]. However, these correspond to studies focused on broad photo-response, with donor-acceptor combinations similar to those oriented to OSCs.

As mentioned before, the polymer PIF8-TAA is a semi-transparent material with limited absorption in the visible range[14], and which only until recently was considered as a donor material in photodetectors for selective red- and blue-light detection when used with the acceptors ITIC-4F and IDFBR[14]. As it can be seen in **Figure 7.1b**, the donor:acceptor combination proposed here, namely, PIF8-TAA:BTP-4Cl yields a semi-transparent active layer exhibiting high transmittance in the visible range and showing a decay in transmittance towards the NIR part of the spectrum. **Figure 7.1c** shows an schematic of the fabrication process followed to develop the reference devices. A glass substrate with pre-defined ITO

electrodes was spin-coated with a layer of the hole-blocking material SnO_2. The active layer material formed by PIF8-TAA and BTP-4Cl was dissolved in CB at a concentration of 40 g L^{-1} and spin-coated on top. The donor:acceptor ratio was varied from 2:1, and 1:1, to 1:2 as described in detail in Section 7.2.2. Finally, the electron-transport material MoO_3 and the second electrode formed by silver where thermally evaporated on top. The final active area of all the OPD devices studied is defined by the overlap of the ITO and silver electrodes and corresponds to 1 mm^2. **Figure 7.1d** shows the HOMO-LUMO levels of BTP-4Cl and PIF8-TAA, with values taken from[72,168,191], as well as the energy levels of the electrodes and transport layers employed, with values taken from[30,72,195–197]. The energy levels show a clear energy offset between the donor and the acceptor materials which is essential to achieve an efficient exciton separation and consecutive charge carriers' collection in the OPD devices.

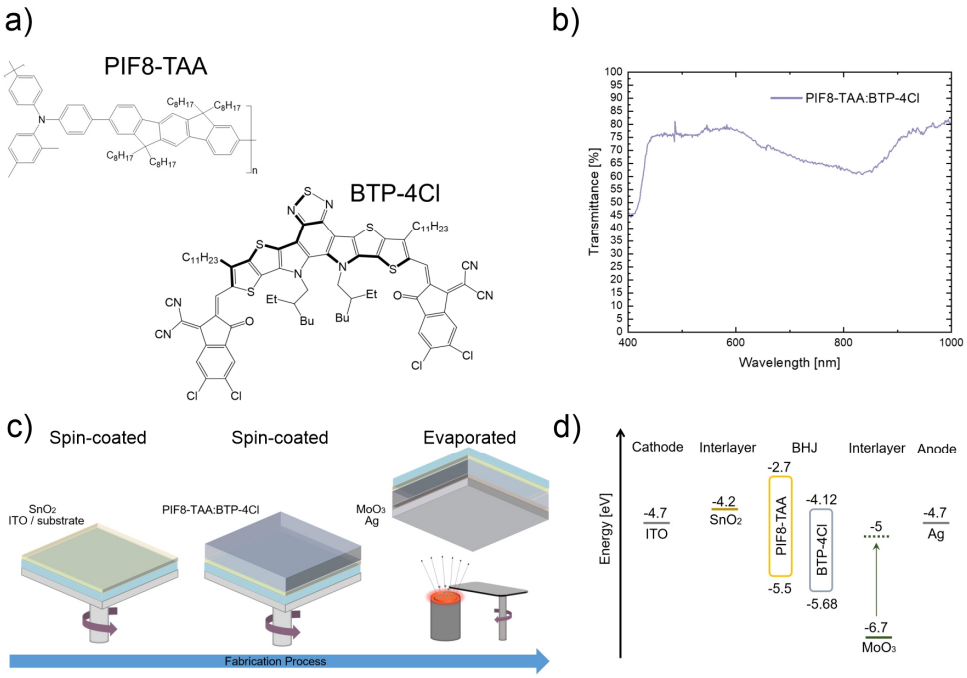

Figure 7.1 Materials and OPD Architecture of Devices with PIF8-TAA:BTP-4Cl Active Layer
a) Molecular structures of the polymer PIF8-TAA and the NFA BTP-4Cl. b) Transmittance measurement for the active layer PIF8-TAA:BTP-4Cl. c) Fabrication process of the spin-coated reference samples. d) Energy levels of PIF8-TAA and BTP-4Cl as well as the energy levels of the electrodes and transport layers employed in the OPD devices. In the case of the interlayer MoO_3, the level offset corresponds to the alignment reported in the case of contact with an organic material[72,197,198].

7.2.2 Definition of Reference Performance in Spin-Coated Devices

In this section the characterization performed in different spin-coated samples is presented. By quantifying the performance of spin-coated samples a benchmark for future devices can be established. In particular, this will be useful to evaluate the performance of devices based on the more elaborated inkjet printed layers. As part of this analysis, different donor to acceptor ratios were studied with the aim to find the optimal combination for OPD devices. **Figure 7.2** shows the J-V, SR, and 3_{dB}-bandwidth plots of the three different donor:acceptor ratios being investigated. From left to right, these correspond to a PIF8-TAA:BTP-4Cl ratio of 1:1, 1:2 and 2:1, respectively.

Figure 7.2a-c shows the J-V characteristics of the devices measured in dark conditions. In this manner, it is possible to study the dark current of the devices at different bias voltages. In general, the J-V measurements of all samples show working devices, without indication of shunt-paths and no signs of problems with the employed blocking layers. This demonstrates an effective design of the OPD stack as well as the suitability of the active layer material. As it can be seen, the blend ratio of 1:1 shows the lowest dark current when operated in reverse bias. At the representative bias voltage of -2 V the dark current of the devices yields a value of 7.61×10^{-8} A cm^{-2}, followed by the blend ratio of 1:2 with 7.30×10^{-7} A cm^{-2}, and lastly with 1.32×10^{-6} A cm^{-2} for the case with a 2:1 ratio.

Figure 7.2d-f shows the SR values of the devices measured at -2 V. In general, the SR measurements of all samples show a significantly higher response in the NIR-range of the spectrum compared with their limited response in the visible range. This is in agreement with their expected behavior based on their PIF8-TAA:BTP-4Cl photoactive layer (see **Figure 7.1b**) where PIF8-TAA contributes mainly to the response at around 400 nm and BTP-4Cl defines the majority of the remaining photo-response. The resulting SR profile yields devices that are semi-transparent in the visible range but which remain photo-responsive for NIR-based applications. As it can be seen, the samples with blend ratios of 1:2 and 2:1 show slightly higher SR values when compared to the sample with 1:1 ratio. In this case, the peak SR values (λ= 840 nm) correspond to 47 mA W^{-1} for the 1:1 ratio, 56 mA W^{-1} for the 1:2 ratio, and 55 mA W^{-1} for the 2:1 ratio.

Figure 7.2g-i shows the frequency response of the devices measured at -2 V. For the devices with blend ratio of 1:1 and 1:2, the f_{-3dB} cut-off frequencies show state-of-the-art performance with values between 3 and 5 MHz, therefore being among the highest

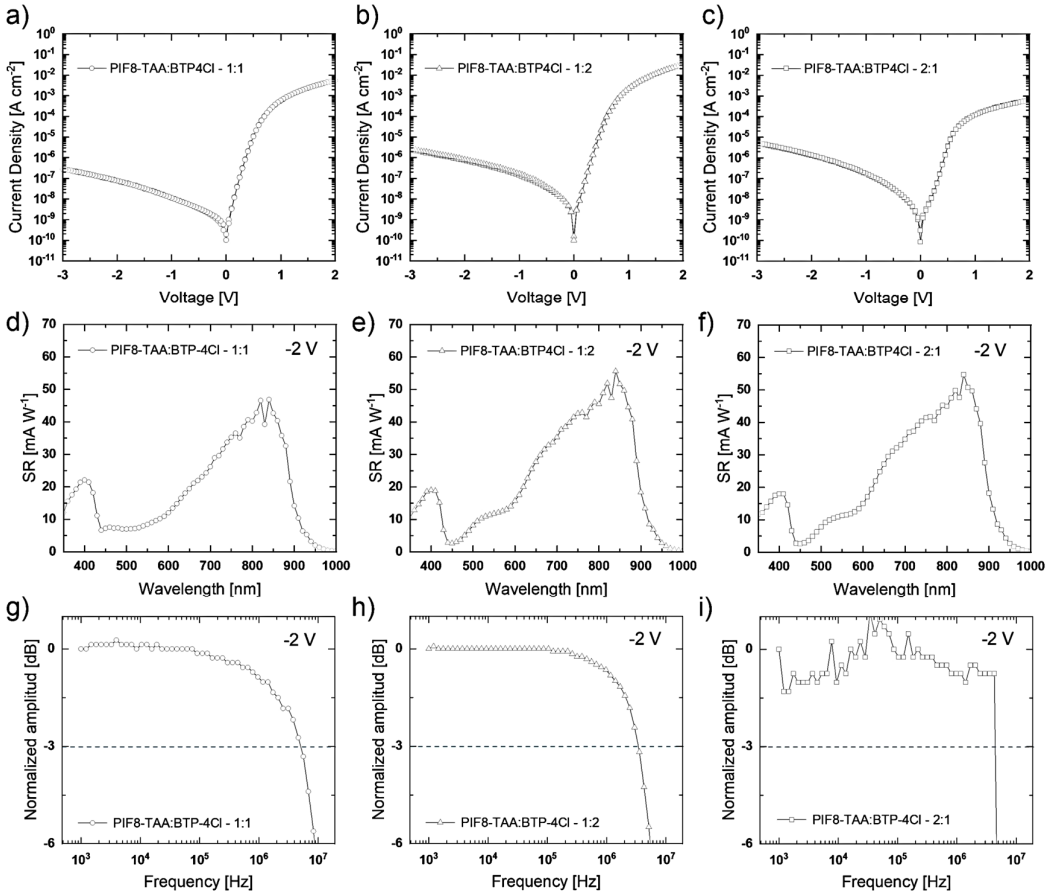

Figure 7.2 Comparison of Donor:Acceptor Ratios in Spin-Coated Devices
a-c) J-V characteristics of the three different donor:acceptor ratios studied. The ratios correspond to 1:1, 1:2 and 2:1, respectively. d-f) Spectral responsivities of the three different donor:acceptor ratios studied. The ratios correspond to 1:1, 1:2 and 2:1, respectively. g-i) Cut-off frequency measurements of the three different donor:acceptor ratios studied. The ratios correspond to 1:1, 1:2 and 2:1, respectevily.

reported in the literature for organic devices[16,21,34,114]. This remarkable performance is well suited for applications where fast detection speeds are required, like in the case of light communication systems. As it can be seen, the blend ratio of 1:1 shows the highest performance in this case. At the representative bias voltage of -2 V the cut-off frequency yields a value of ~5.03 MHz, compared to 3.38 MHz from the devices with blend ratio 1:2. The measurements performed on the devices with blend ratio 2:1 show an unstable behavior from which a reliable cut-off frequency cannot be determined.

Based on the presented results, the blend ratio of 1:1 was selected as being the most efficient due to having the lowest dark current and highest cut-off frequency while maintaining a similar SR performance. In specific, the devices with 1:1 ratio showed a dark current

around one order of magnitude lower than the 1:2 devices and almost two orders of magnitude lower than the devices with 2:1 ratio. The SR showed a maximum absolute difference of 9 mA W^{-1} in comparison with the other devices (see Table 7.1). Finally, the f_{-3dB} value was 1.486 times higher than the other devices.

It can be noted that an in-depth understanding of the influence of blend ratios on the different device characteristics cannot be successfully extracted based on the presented results because the experiments performed cannot account for other important variables such as those related to the morphological differences of the films[32,118]. However, the aim of this analysis is to accomplish an efficient determination of the optimal donor:acceptor combination to be employed in the OPD devices. By using spin-coating to undergo this performance optimization, the iteration time and the complexity of device processing can be minimized. Additionally, the findings from this section can be implemented in future devices such as those employing inkjet printed active layers.

In consideration of the results obtained in this section, and summarized in Table 7.1, the selected blend ratio of 1:1 is applied in all consecutive devices of the following sections.

Table 7.1 Summary of performance on OPDs with spin-coated PIF8-TAA:BTP-4Cl active layer based on donor to acceptor ratio.

Donor:acceptor ratio	Dark current [A cm^{-2}]	Maximum SR @ 840 nm [mA W^{-1}]	f_{-3dB} [MHz]
1:1	$7.61x10^{-8}$	47	5.03
1:2	$7.30x10^{-7}$	56	3.38
2:1	$1.32x10^{-6}$	55	-

7.3 Ink Formulation for Inkjet Printing and Devices with Inkjet Printed PIF8-TAA:BTP-4Cl Active Layer

In the following, the ink formulation and characterization of the active layer is presented in terms of its suitability for inkjet printing. Then, the inkjet printed active layer is employed to fabricate OPD devices with the same device stack used in the spin-coated references. The devices containing the inkjet printed active layer are optimized and then compared to the spin-coated OPDs.

7.3.1 Inkjet Printing of PIF8-TAA:BTP-4Cl Active Layer

After the capability of the new BHJ system was successfully demonstrated in spin-coated devices, this section introduces the ink formulation of the active layer developed for printed devices and the analysis of the ink in terms of its suitability for inkjet printing. **Figure 7.3a** shows an schematic with the different components used in the ink formulation. In this case, PIF8-TAA and BTP-4Cl are dissolved in DCB in a 1:1 ratio and at a concentration of 20 g L^{-1}. After deposition the active layer is annealed for 10 minutes at 140°C. Different printing resolutions were employed to deposit the active layers as described later in Section 7.3.3. The choice of DCB as the solvent material has two main considerations: first, in contrast to the solvent CB used in the spin-coated references, DCB has a boiling point that is well-suited for an inkjet printing process where it tends to lead to less clogging issues at the nozzles. Secondly, when used to dissolve both PIF8-TAA and BTP-4Cl it yields an ink with viscoelastic properties that match the requirements for droplet ejection during inkjet printing. As it can be seen in **Figure 7.3b**, the ink formulation lies in the printable zone of the Weber – Reynolds diagram. Additionally, **Figure 7.3c** shows the pendant drop analysis and contact angle analysis of the developed ink. The pendant drop analysis was used to determine a surface tension equal to 28.75 mN m^{-1}, to be used in the calculation of the Weber – Reynolds diagram. The contact angle measurements, with an average contact angle of 14.5°, show that the active layer has a good wetting behavior when deposited on top of a glass substrate covered with SnO_2. This indicates that the ink is also well suited for the OPD architecture employed.

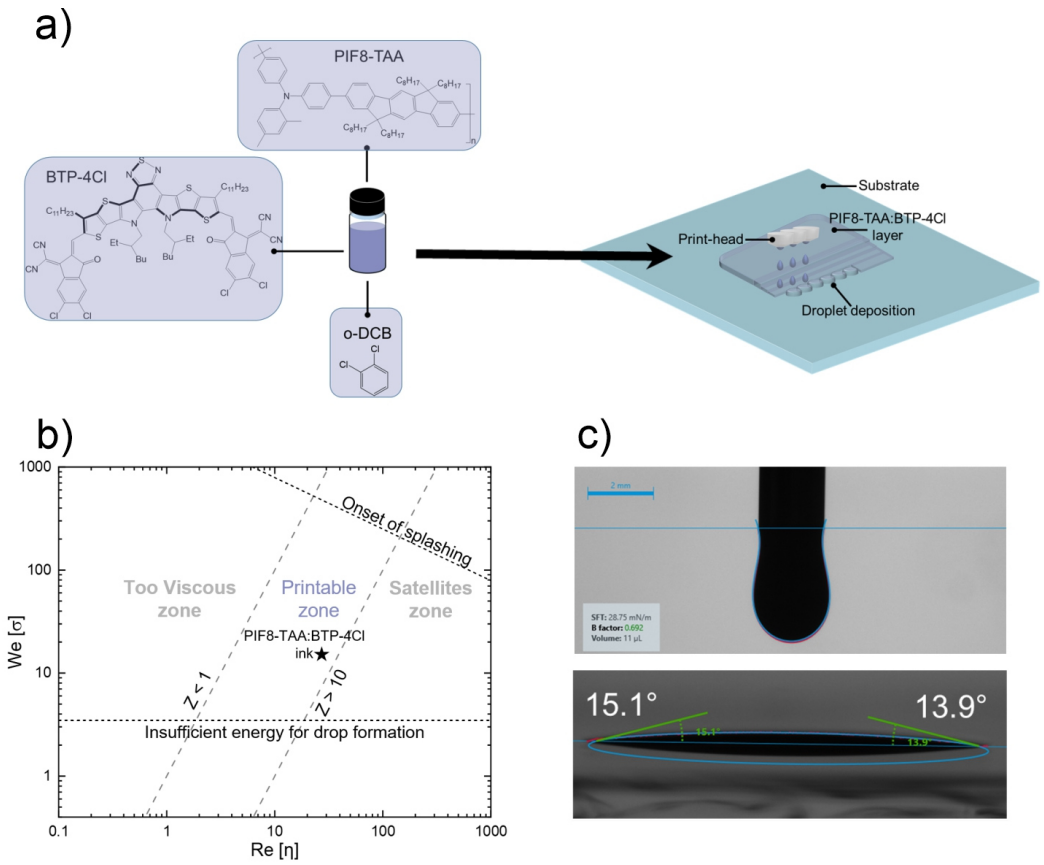

Figure 7.3 PIF8-TAA:BTP-4Cl Ink for Inkjet-Printed OPDs
a) Schematic of ink formulation and inkjet printing process for the PIF8-TAA:BTP-4Cl active layer. b) Assessment of ink printability for the PIF8-TAA:BTP-4Cl ink. c) Drop pending analysis (top) and drop wetting analysis (bottom) for the PIF8-TAA:BTP-4Cl ink. The substrate used corresponds to SnO_2-covered glass.

7.3.2 Devices with Inkjet-Printed PIF8-TAA:BTP-4Cl Active Layer

After the development of an ink formulation suitable for inkjet printing, the active layer was employed to fabricate inkjet-printed OPD devices that can be compared to the spin-coated references. In the following, the OPD architecture employed for the inkjet-printed devices, and the fabrication process that was followed, are presented.

Figure 7.4a shows an schematic of the fabrication process followed to develop the inkjet-printed devices. With respect to the process employed for the fabrication of spin-coated devices (see **Figure 7.1c**), the only difference is the deposition of the active layer. Namely, a glass substrate with pre-defined ITO electrodes was spin-coated with a layer of the hole-

blocking material SnO_2. The active layer material formed by PIF8-TAA and BTP-4Cl was prepared as described in Section 7.3.1 and inkjet-printed on top. The dpi was optimized as described later in Section 7.3.3. Finally, the electron-transport material MoO_3 and the second electrode formed by silver where thermally evaporated on top. **Figure 7.4b** shows a photograph of a fabricated sample. Similar to the case of the spin-coated samples, most layers in the stack, have a high transmittance in the visible range and therefore only the silver layers forming the electrodes can be easily appreciated. The final active area of all the OPD devices studied corresponds to 1 mm^2.

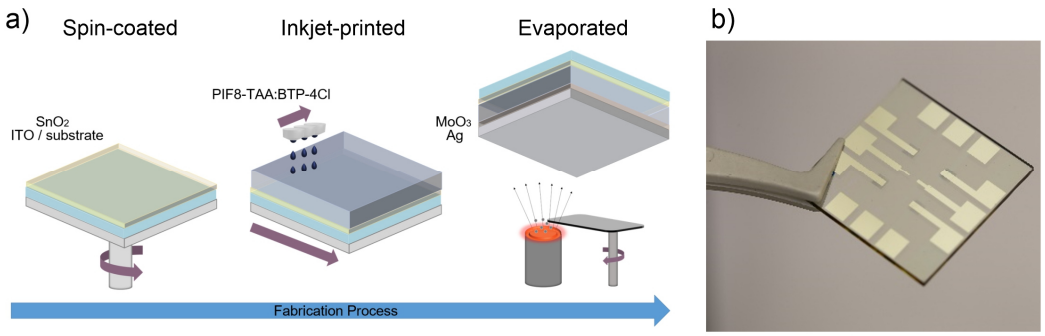

Figure 7.4 Architecture of Devices with Inkjet-Printed PIF8-TAA:BTP-4Cl Active Layer
a) Fabrication process of the samples with inkjet-printed active layer. b) Photograph of an exemplary sample containing the inkjet-printed active layer PIF8-TAA:BTP-4Cl.

7.3.3 Optimization of Performance in Devices with Inkjet-Printed PIF8-TAA:BTP-4Cl Active Layer

In this section the characterization performed in different inkjet-printed samples is presented. At first, the OPD devices based on inkjet-printed active layers were fabricated at different printing resolutions in order to find the optimal parameter for the OPDs. Devices containing an active layer with a resolution of 635, 725.71 and 846.67 dpi where fabricated. The lowest dpi employed, i.e. 635, did not yield functional devices due to short-cuts and was thus not investigated further. The comparison of the devices with a resolution of 725.71 and 846.67 dpi is presented here.

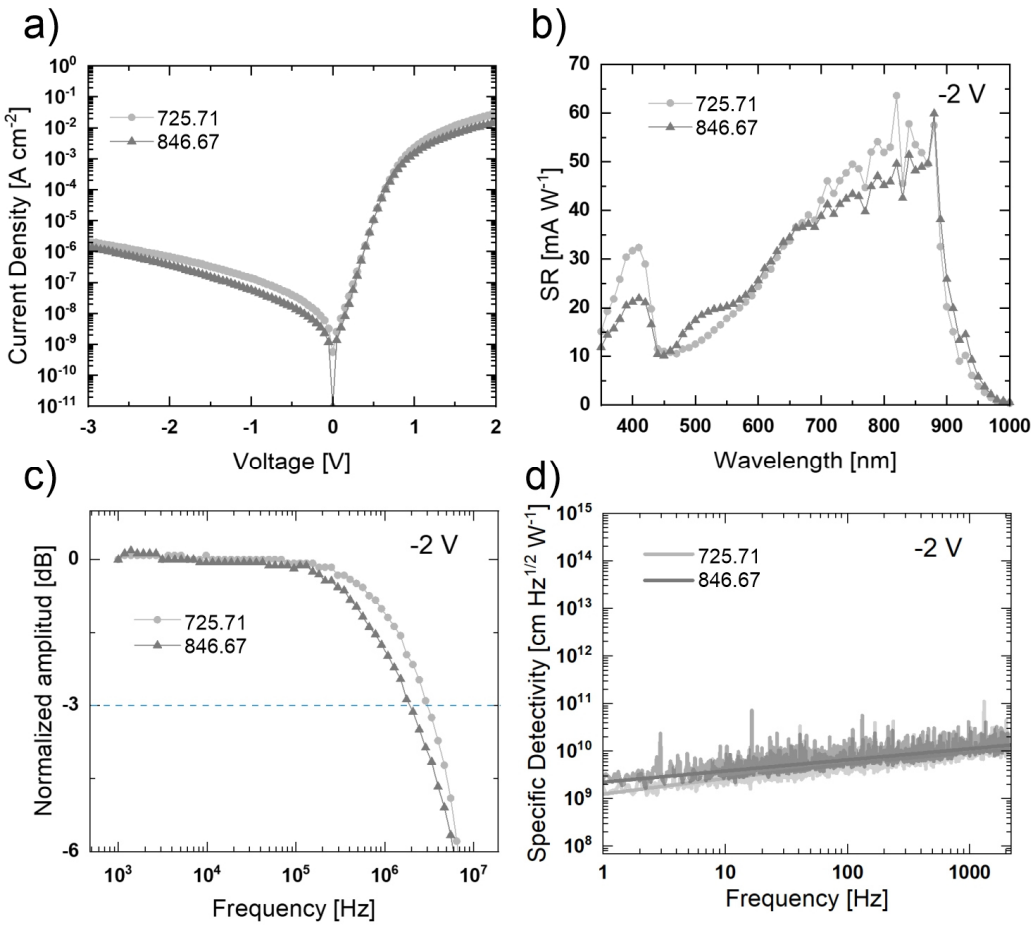

Figure 7.5 Characteristics of OPDs with Inkjet-Printed PIF8-TAA:BTP-4Cl Active Layer at Different Printing Resolutions
a) J-V curves measured in the dark. b) SR measurements at -2 V. c) Bandwidth measurements at -2 V. d) Specific detectivity at -2 V. A python module developed by Dr. Mervin Seiberlich was used to process the data of the spectral noise density and the specific detectivity.

Figure 7.5 shows a direct comparison of the different OPD characteristics for devices with the two different printing resolutions. **Figure 7.5a** shows the J-V curves in the dark. As it can be seen, the dark currents of both devices show a very similar performance. At the representative voltage of -2 V, the devices have and absolute difference in dark current of only 0.33 μA cm^{-2}.

Figure 7.5b depicts the SR performance at -2 V. Here, the performance between both devices is again very similar. Small variations in their profile can be observed from around 450 to 550 nm and again at around 700 to 850 nm. This could be attributed to variations in their layer thickness as expected by the different printed resolutions. Nevertheless, the

variations observed are minimal, and the general profile of the photoactive layer remains, showing a higher response in the NIR-part of the spectrum in comparison to its lower response in the visible range. In this case, the maximum SR achieved corresponds to 58 mA W^{-1} (see Table 7.2).

Figure 7.5c shows the frequency response at -2 V. In this case, the difference in performance is more pronounced with the devices of dpi = 725.71 showing the highest detection speed. The f_{-3dB} values correspond to ~2 and ~3 MHz for the devices of dpi = 846.67 and the devices of dpi = 725.71, respectively (see Table 7.2).

To complement the characterization of the printed devices, their specific detectivity D^* is also presented, as shown in **Figure 7.5d**. A python module developed by Dr. Mervin Seiberlich was used to process the data of the spectral noise density and the specific detectivity. At the representative bias voltage of -2 V, the calculated D^* corresponds to up to 6.13×10^9 Jones for the devices using dpi= 725.71 and to 7.44×10^9 Jones for the devices using dpi= 846.67. The corresponding noise spectral density (Sn) measurement used for the calculations can be found in Figure A.6 of the appendix.

In summary, the printing resolution with dpi = 725.71 was selected as being the most efficient based on the presented results, showing a 50% increase in cut-off frequency, and a more favorable SR-profile for semi-transparent devices with NIR detection; all while maintaining a very similar performance in terms of specific detectivity and dark current.

In consideration of the results obtained in this section, and which are summarized in Table *7.2*, the selected printing resolution with dpi = 725.71 is applied in all consecutive devices of the following sections.

Table 7.2 Summary of performance on OPDs with inkjet-printed PIF8-TAA:BTP-4Cl active layer based on printing resolution.

Printing resolution [dpi]	Dark current [A cm^{-2}]	Maximum SR @ 840 nm [mA W^{-1}]	f_{-3dB} [MHz]	D^* [Jones]
725.71	6.76×10^{-7}	58	2.96	6.13×10^{-9}
846.67	3.51×10^{-7}	51	1.98	7.44×10^{-9}

Moreover, after the selection of an optimal printing resolution for inkjet-printed devices, the optimized devices were studied further by measuring their characteristics at increased voltages and varied light intensities in order to broaden the study of their light response.

Their additional characterization and its comparison to the spin-coated references is presented here.

Figure 7.6 shows the steady-state and dynamic characteristics of the devices based on the inkjet-printed active layer. The J-V characteristics are shown in **Figure 7.6a**. The plot shows the dark current as well as different currents measured under illumination using an NIR LED (λ= 850 nm) with a maximum optical power of 15 mW cm^{-2}.

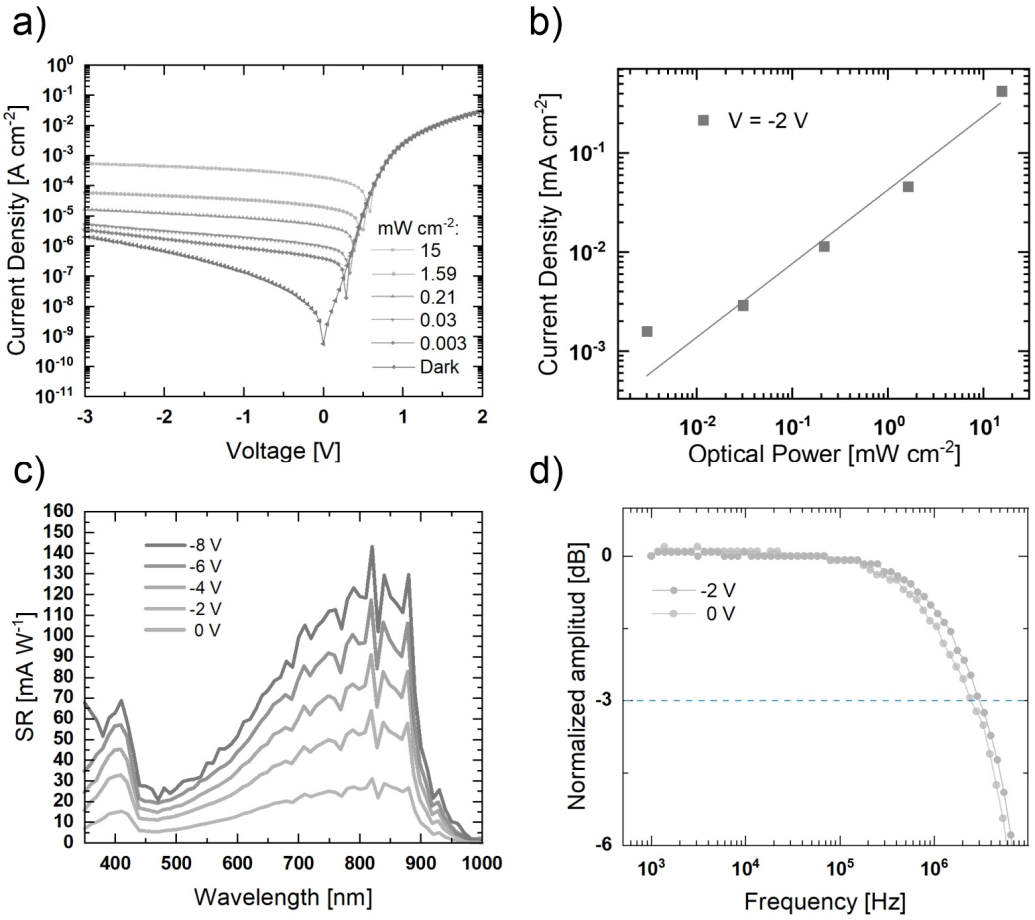

Figure 7.6 Further Characterization of OPDs with Inkjet-Printed PIF8-TAA:BTP-4Cl Active Layer

a) J-V curves measured in the dark and under illumination (λ= 850 nm). b) Current densities at different optical powers at -2 V. LDR= 56 dB. c) SR measurements from 0 to -8 V. d) Bandwidth measurements at 0 and -2 V with f_{-3dB} > 2 MHz. Active layer of devices printed at dpi = 725.71.

The measurements show a dark current of 6.76×10^{-7} A cm^{-2}. This is a very similar performance to the dark current of the reference devices deposited by spin-coating. In this case, the dark current is slightly higher with an absolute difference of 0.6 μA cm^{-2} when compared to the reference devices.

To further complement the characterization of the printed devices, their dynamic behavior at different optical powers was studied. **Figure 7.5b** Shows the current density versus optical power for the different currents measured under illumination. Based on this, an LDR of 56 dB was estimated for the devices. An estimation of an LDR value did not form part of the screening process employing spin-coated devices.

Figure 7.6c shows the SR performance at different voltages. In general, all the SR measurements show the expected profile based on their PIF8-TAA:BTP-4Cl photoactive layer with a higher response in the NIR-range as compared to the limited response in the visible range. This is also in agreement with the profile seen for the reference devices deposited by spin-coating. Moreover, at the representative voltage of -2 V the SR value at λ= 840 nm corresponds to 58 mA W^{-1}. In this case, the SR performance of the printed devices has a higher value than the peak SR of spin-coated devices, with an absolute difference of 11 mA W^{-1} when compared to the reference devices. At -8 V, i.e., the maximum voltage measured, the SR value at λ= 840 nm was 129 mA W^{-1}.

Figure 7.6d depicts the frequency response at 0 and -2 V. At 0 V the f_{-3dB} has a value of ~2.48 MHz and at -2 V it has a value of ~2.96 MHz. This increase in f_{-3dB} is likely due to a more efficient extraction of the charge carriers caused by the increment in bias voltage. At the representative bias voltage of -2 V, the devices show a lower detection speed when compared to the reference spin-coated devices with an absolute difference of 2.07 MHz. This decrease in performance is not fully understood but it is likely caused by the different processing of the active layers. In particular, variations in ink formulation solvents are known to influence the domain size and crystallinity of BHJ blends which could lead to the changes in device performance[32,118].

In summary, the inkjet printed active layer was successfully used to fabricate OPD devices that show a similar performance to the performance of spin-coated devices composed by the same device stack. Additionally, their performance is comparable to the performance of other NIR-oriented OPD devices found in literature[172,174,199–210]. With their most significant advantage being their state-of-the-art detection speed. Their good device performance in combination with their deposition via an industrially-relevant fabrication technique makes this BHJ system a promising option for real-world applications.

7.4 Semi-Transparent Inkjet-Printed Devices

After the previous sections successfully demonstrated the functionality and performance of the PIF8-TAA:BTP-4Cl photoactive layer, and seeking to fully exploit the potential advantages of its low absorption in the visible range, in this section, different device architectures are designed and fabricated aiming to expand the application of the new BHJ from opaque to semi-transparent devices. The aim is to achieve functional devices formed by OPD stacks where all layers show a high transmittance in the visible range. In the following, two different semi-transparent technologies and their corresponding characterization are presented. The two approaches investigated correspond to: semi-transparent devices with ultra-thin silver electrodes and semi-transparent devices with PEDOT electrodes. The performance of both technologies is compared between each other as well as to the performance of reference spin-coated devices and printed devices with opaque architecture. Finally, a potential application of the semi-transparent devices is presented.

7.4.1 Semi-Transparent Devices with Ultra-Thin Silver Electrodes

The first approach to achieve semi-transparent devices consisted on lowering the thickness of the evaporated silver electrodes in order to achieve transparent but conductive electrodes[189,211–218]. Therefore, the OPD stack and fabrication process of these devices remains the same as described for the printed opaque devices in Section 7.3.2, with the only difference being the reduced thickness of the silver layer during the evaporation process. In this case, the thickness was reduced from 100 nm to only 10 nm. The selection of a 10 nm thickness is based on previous studies reported in the literature. Such ultra-thin silver deposition has been previously studied in literature to achieve semi-transparent electrodes, with a silver thickness of 10 nm showing a good trade-off between high optical transmittance and a low sheet resistance[19,219,220].

The characterization of the devices is shown in **Figure 7.7**, where **Figure 7.7a**. shows the J-V characteristics of the devices. It depicts the currents in the dark and under illumination using an NIR LED (λ= 850 nm) with a maximum optical power of 15 mW cm^{-2}. The measurements show a dark current of $1.10x10^{-5}$ A cm^{-2}. This is a lower

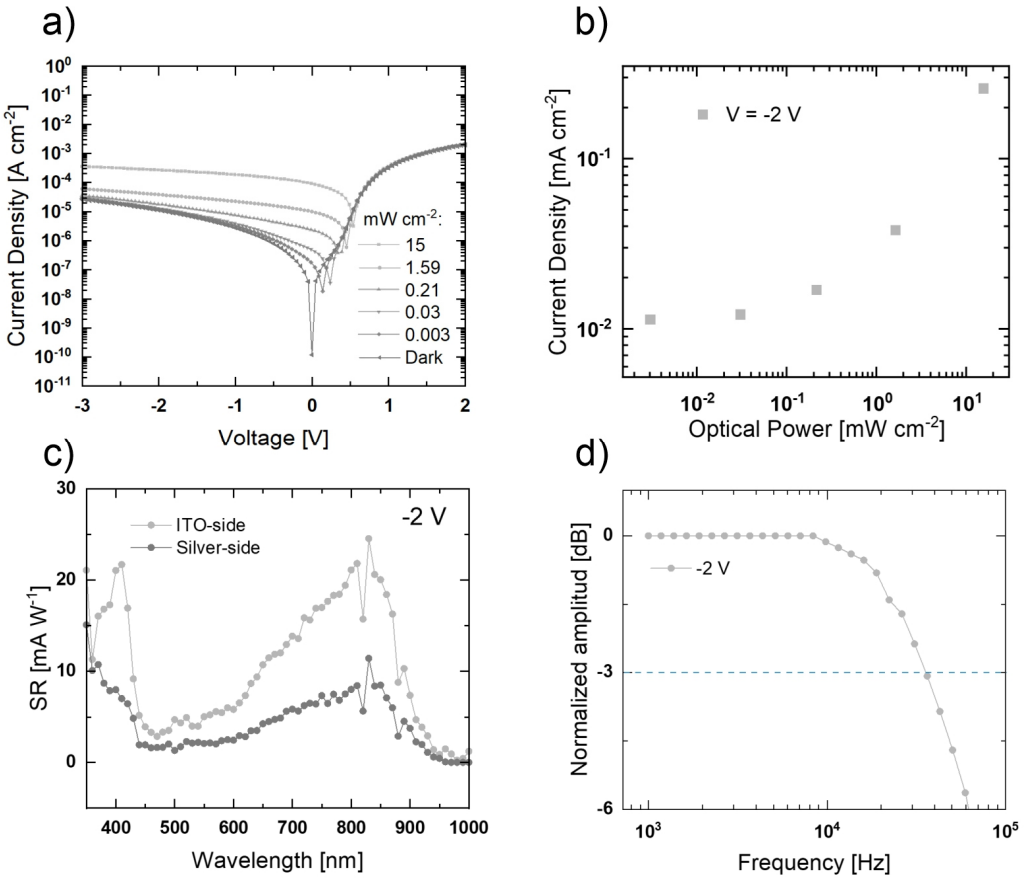

Figure 7.7 Semi-Transparent Devices with Ultra-Thin Silver Electrode
a) J-V curves measured in the dark and under illumination (λ= 850 nm). b) Current densities at different optical powers at -2 V. LDR= 27 dB. c) SR measurements at -2 V with incoming illumination from the ITO and ultra-thin silver electrodes. d) Band-width measurement at -2 V.

performance compared to both the reference devices deposited by spin-coating and to the printed active layer devices with opaque OPD stack. In this case, the absolute difference in dark current corresponds to 10.91 μA cm^{-2} and to 10.31 μA cm^{-2} when compared to the spin-coated and printed devices, respectively. Moreover, their LDR estimated from the currents under illumination is low, with a calculated value of 27 dB as compared to a value 56 dB for the opaque printed samples. The corresponding LDR plot can be seen in **Figure 7.7b**.

Figure 7.7c shows the SR performance of the devices. Since both electrodes in this OPD stack are semi-transparent, the SR was measured with the light incidence coming from the ITO electrode and then repeated with the light incidence coming from the silver electrode. In general, the SR measurements exhibit the expected profile based on their PIF8-

TAA:BTP-4Cl photoactive layer. However, in this case the response at 400 nm is enhanced when compared to the SR profile seen for the spin-coated and for the printed opaque samples. This enhancement could be caused by variations in light reflection and light-interference coming from the different optical paths. The rest of the SR range remains the same as with the profile of the reference samples. Moreover, the SR values are notably higher when the devices are measured with an incident light coming from the ITO side as compared to the silver side. This is not surprising considering the higher transmittance of the ITO electrode. Nevertheless, the devices remain functional when illuminated in either direction. At the representative voltage of -2 V the values at λ= 840 nm correspond to 21 mA W^{-1} and 8 mA W^{-1} for the ITO and silver side, respectively. Taking the measurements from the ITO-side, the comparison to the spin-coated and printed opaque samples yields an absolute difference of 26 mA W^{-1} and 37 mA W^{-1}, respectively.

Figure 7.7d shows the frequency response at -2 V measured with incident light at the ITO side. In this case the devices show a low detection speed with an f_{-3dB} value of ~35.80 kHz. When compared to the spin-coated and opaque printed samples, which have f_{-3dB} values in the MHz range, the difference in performance is significant. This drop in f_{-3dB} stems from the increased series resistance of the significantly thinner silver electrode.

In summary, the performance of the devices with ultra-thin silver electrode is significantly lower than the performance of the spin-coated and opaque printed active layer devices. In particular, they showed 2.8 times lower SR, two times lower LDR, and above 80 times lower f_{-3dB} performance than the opaque printed devices. While the drop in SR performance is expected due to an increased transparency, their LDR and f_{-3dB} are too low to justify further investigation of these devices. In the following subsection the investigation of a different architecture for semi-transparent OPDs is presented.

7.4.2 Semi-Transparent Devices with PEDOT Electrodes

The second approach to achieve semi-transparent devices consisted on introducing PEDOT:PSS as an inkjet-printed electrode. **Figure 7.8a** shows an schematic of the fabrication process followed to develop these semi-transparent devices. With respect to the process employed for the fabrication of the printed opaque devices in Section 7.3.2, the difference is the replacement of the evaporated layers, i.e. MoO_3 and silver, by an inkjet-printed

PEDOT:PSS layer. Namely, a glass substrate with pre-defined ITO electrodes was spin-coated with a layer of the hole-blocking material SnO_2. The active layer material formed by PIF8-TAA and BTP-4Cl was prepared as described in Section 7.3.1 and inkjet-printed on top. Finally, the PEDOT:PSS electrode was inkjet-printed on top. The final active area of all the OPD devices studied corresponds to 1 mm^2.

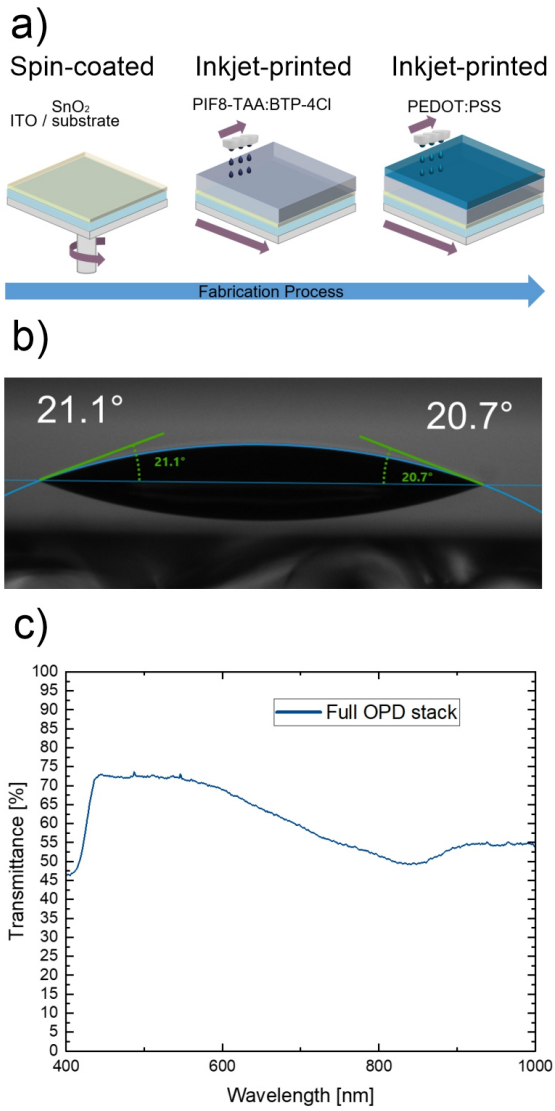

Figure 7.8 Semi-Transparent Devices with PEDOT Electrode
a) Fabrication process of the semi-transparent samples containing PEDOT electrodes. b) Contact angle measurements for the PEDOT:PSS ink over the active layer PIF8-TAA:BTP-4Cl. c) Transmittance measurement for the full OPD stack composed of PEDOT:PSS/PIF8-TAA:BTP-4Cl/SnO_2/ITO.

The PEDOT:PSS ink employed here corresponds to the commercially available FHC solar ink that was also introduced in Chapter 5. Contact angle measurements for the PEDOT:PSS ink over the active layer PIF8-TAA:BTP-4Cl are shown in **Figure 7.8b**. The contact angle measurements corroborate that the PEDOT:PSS ink is also well suited for the OPD architecture employed here, showing a good wetting behavior when deposited on top of a glass substrate covered with the active layer PIF8-TAA:BTP-4Cl.

Figure 7.8c depicts the transmittance of the full OPD stack composed by ITO, SnO_2, PIF8-TAA:BTP-4Cl and PEDOT:PSS. As it can be seen, the presented OPD stack has a high transmittance in the visible range. The plot shows transmittance values nearing 70% in the range of 435 to 600 nm, with a lowest value of 59% at 700 nm. Additionally, a further decay in transmittance towards the NIR range, where the devices can be operated, is also evident. In the plot, the transmittance of the active layer PIF8-TAA:BTP-4Cl alone is also shown for comparison. Finally, **Figure 7.9** compares the optical appearance of the semi-transparent devices (**Figure 7.9a**) against the opaque devices (**Figure 7.9b**).

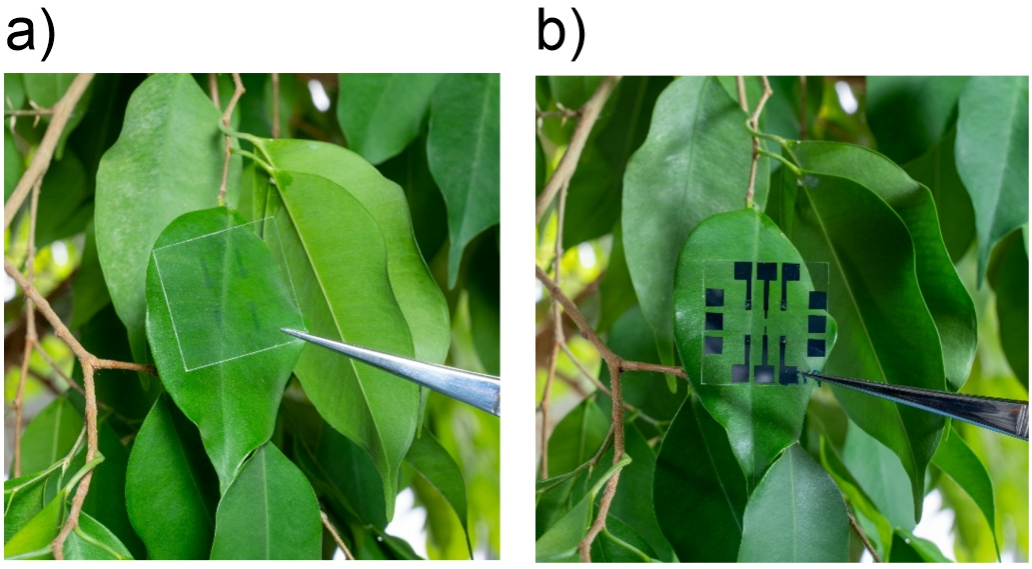

Figure 7.9 Semi-Transparent and Opaque Devices
a) Photograph of semi-transparent device with OPD stack composed by PEDOT:PSS/ PIF8-TAA:BTP-4Cl/SnO_2/ITO. b) Photograph of opaque device with OPD stack composed by Ag/MoO_3/PIF8-TAA:BTP-4Cl/SnO_2/ITO.

The photographs highlight the see-through capabilities of the semi-transparent devices as compared to the opaque samples, which could represent an important advantage in terms of their potential for innovative applications.

7.4.3 Performance of the Semi-Transparent Devices with PEDOT Electrodes

In the following, the characterization of the semi-transparent devices with PEDOT electrodes is presented. Additionally, their performance is compared to that of the semi-transparent devices using ultra-thin silver as well as to the performance of reference spin-coated devices and printed devices with opaque architecture. Finally, a practical application of the devices is presented.

The characterization of the devices is shown in **Figure 7.10**. The J-V curves of the devices are presented in **Figure 7.10a**. During illumination a NIR LED (λ= 850 nm) was used, where the maximum optical power corresponds to 15 mW cm^{-2}. At the representative voltage of -2 V, the devices show a dark current of $4.19x10^{-6}$ A cm^{-2}. This is an improvement in performance compared to the semi-transparent devices using an ultra-thin silver electrode, with an absolute difference in dark current of 6.80 μA cm^{-2}. When compared to the reference devices deposited by spin-coating and to the printed active layer devices with opaque OPD stack the absolute difference in dark current corresponds to 4.12 μA cm^{-2} and to 3.52 μA cm^{-2}, respectively. Concerning the dynamic range of the devices, the LDR value estimated from the currents under illumination yields a value of 66 dB. This also represents an improvement in performance when compared to the value of 27 dB for the semi-transparent devices using an ultra-thin silver electrode, and to the value of 56 dB for the opaque printed samples. The corresponding LDR plot can be found in Figure A.7 of the appendix.

Figure 7.10b shows the SR performance of the devices. Since both electrodes in this OPD stack are semi-transparent, the SR was measured with the light incidence coming from the ITO electrode and then repeated with the light incidence coming from the PEDOT electrode. In this case, the SR measurements also retain their expected profile based on the PIF8-TAA:BTP-4Cl active layer. When the devices are illuminated from the ITO side, the same increase in response at 400 nm is observed as in the case of the semi-transparent devices of ultra-thin silver electrode. Specifically, the response at 400 nm is enhanced when compared to the SR profile seen for the spin-coated and for the printed opaque samples. The response in the remaining of the visible and NIR range remains the same as with the profile of the reference samples. On the other hand, when the devices are illuminated from the PEDOT side, there is no enhancement of response at 400 nm.

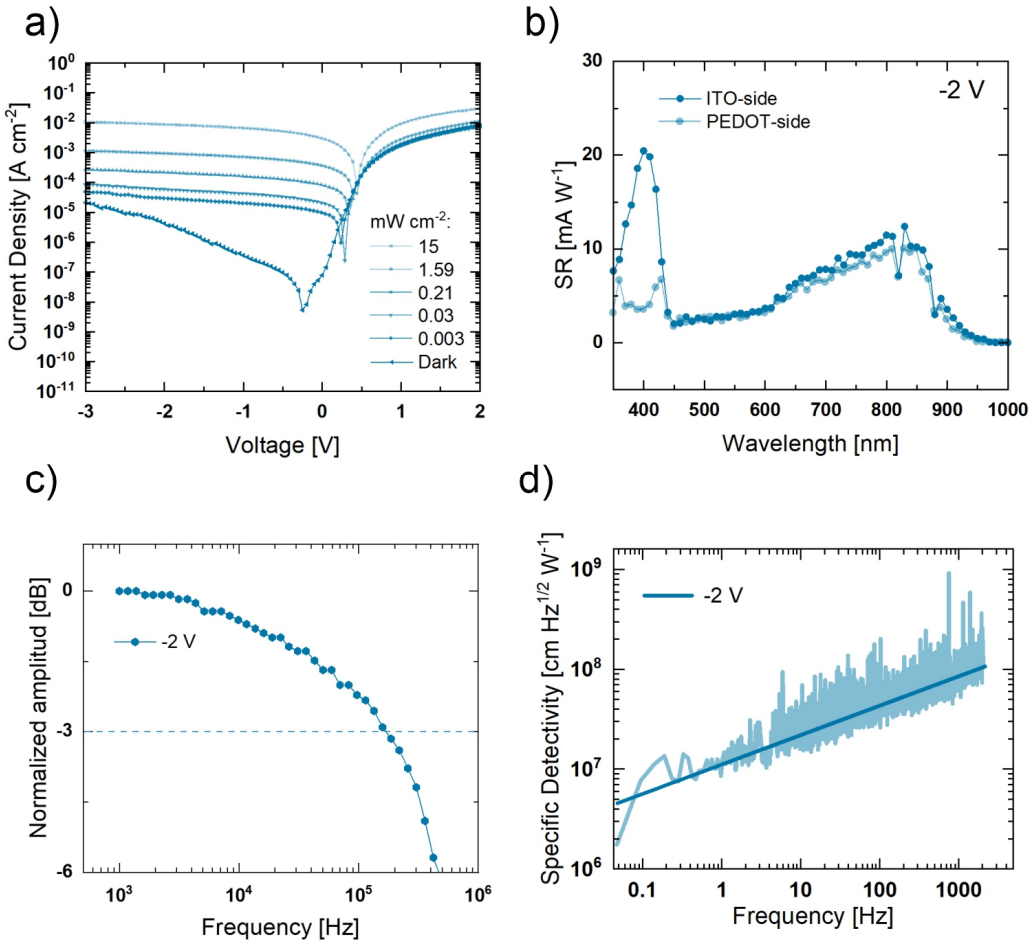

Figure 7.10 Characteristics of Semi-Transparent Devices with PEDOT Electrode
a) J-V curves measured in the dark and under illumination (λ= 850 nm). b) SR measurements at -2 V with incoming illumination from the ITO and PEDOT electrodes. c) Bandwidth measurements at -2 V. d) Specific detectivity at -2 V. A python module developed by Dr. Mervin Seiberlich was used to process the data of the spectral noise density and the specific detectivity.

This difference can be caused by variations in light reflection and light-interference due to the different optical paths. More broadly, the results show similar SR values when the devices are measured with an incident light coming from the ITO side as compared to the PEDOT side. At the representative voltage of -2 V the peak values correspond to 10.29 mA W^{-1} and 9.59 mA W^{-1} for the ITO and PEDOT side, respectively. From here, the measurements from the ITO side are taken for comparison to the other technologies. Compared to the semi-transparent devices using an ultra-thin silver electrode, this corresponds to an absolute difference of 10.31 mA W^{-1}. When compared to the spin-coated and printed

opaque samples this corresponds to an absolute difference of 36.58 mA W^{-1} and 47.53 mA W^{-1}, respectively.

Figure 7.10c depicts the frequency response at -2 V measured with incident light at the ITO side. In this case the devices show a moderate detection speed with a f_{-3dB} value of ~174 kHz. When compared to the spin-coated and opaque printed samples, which have f_{-3dB} values in the MHz range, the difference in performance is still significant, however, it represents a more than fourfold improvement when compared to the semi-transparent devices using the ultra-thin silver electrode, which showed f_{-3dB} values of ~35.80 kHz.

The specific detectivity D^* is shown in **Figure 7.10d**. A python module developed by Dr. Mervin Seiberlich was used to process the data of the spectral noise density and the specific detectivity. The calculated D^* corresponds to up to 5.08×10^{07} Jones at –2 V. The corresponding noise spectral density (Sn) measurement used for the calculation can be found in Figure A.8 of the appendix.

Overall, the performance of the semi-transparent devices with PEDOT electrode is significantly higher than the performance of the semi-transparent devices with ultra-thin silver electrode. In particular, they show a more than fourfold increase in cut-off frequency, and above a twofold increase in LDR.

In comparison to the reference samples with opaque stack, the performance of the PEDOT-based semi-transparent devices remains lower. In particular, the opaque samples, deposited either by spin-coating or inkjet printing, show SR values that are at least four times higher, and remarkable f_{-3dB} values in the MHz range, compared to the useful yet comparatively modest response in the kHz range for the semi-transparent devices. However, the semi-transparent devices benefit from a higher transmittance in the visible range while remaining competitive in their figures of merit, especially in the NIR range, making them suitable for see-through and NIR applications that could not be accomplished with the opaque samples.

Figure 7.11 shows an example of a potential application. As it can be seen in **Figure 7.11a**, the experiment consists of a photoplethsmography (PPG) measurement performed in transmission mode. More specifically, the OPD device receives part of the LED-emitted light that is transmitted through a finger. Then, based on this, it generates a dynamic response that is influenced by the varying blood-flow and from which a pulse can be estimated. Additionally, semi-transparent devices could be used to detect signals in a discrete and non-invasive manner facilitating the potential design and development of innovative health-monitoring devices. This is exemplified in **Figure 7.11b**, where, due to the see-

through capability of the devices, the finger remains visible behind the sample. The response versus time of the PPG measurement can be seen in **Figure 7.11c**. From here, a pulse of 71 bpm was estimated. The transparency of the sensors is expected to enable new designs for health-monitoring devices which are particularly advantageous for wearable and on-body sensors.

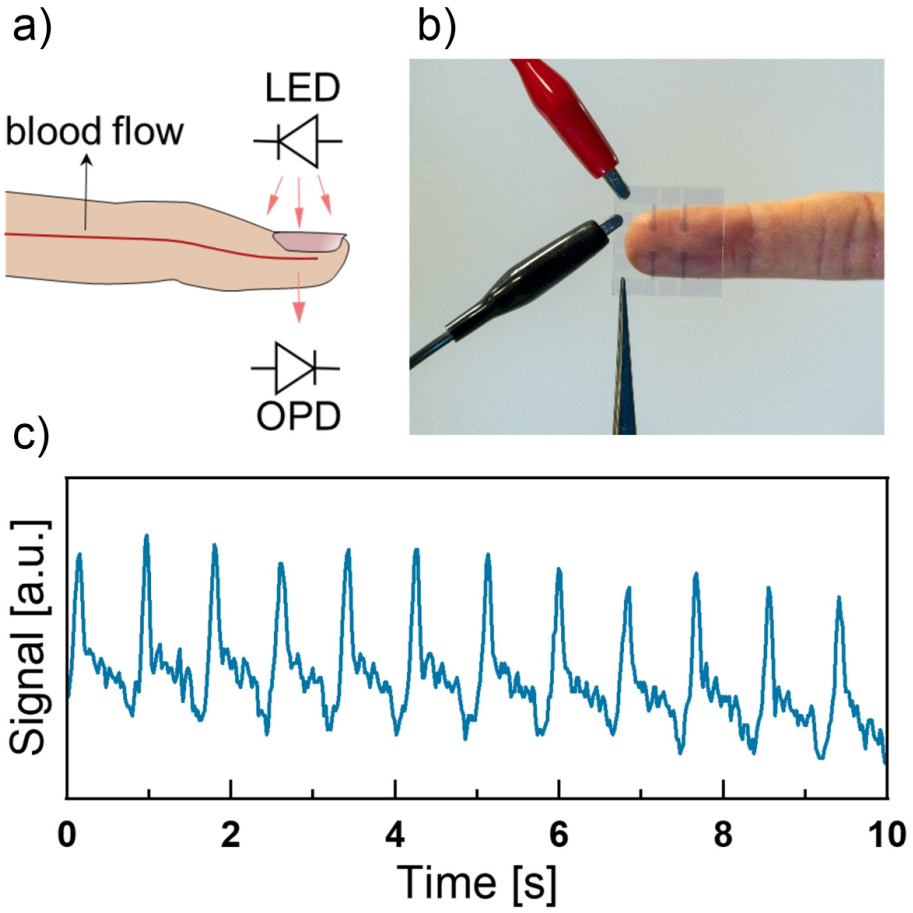

Figure 7.11 PPG Measurement
a) Schematic representation of PPG measurement in transmittance mode. b) Photograph of real sample in front of a finger. Due to the see-through capability of the devices, the finger remains visible behind the sample. c) Signal of pulse measurement against time.

7.5 Summary

In this chapter, a new BHJ system that focuses in the NIR part of the spectrum was investigated. The new BHJ system was based on the NFA known as BTP-4Cl which has NIR absorption; in combination with the donor and transparent polymer known as PIF8-TAA. The result was a semi-transparent active layer exhibiting high transmittance in the visible range with an effective photoresponse focused in the NIR part of the spectrum.

At first, the capability of the new BHJ system was determined by analyzing samples fabricated with spin-coated active layers. This allowed for an efficient screening of the material system before undergoing its adaptation into an inkjet-printed process. In specific, the results from the analysis of spin-coated samples proved the suitability of the new BHJ for OPD devices by yielding OPDs with high performance showing a f_{-3dB} of up to 5 MHz and a responsivity of up to 56 mA W^{-1} at -2 V. It also enabled the selection of an optimal donor to acceptor blend ratio, and allowed to set a quantified benchmark for future devices.

Subsequently, the ink formulation and characterization of the active layer was presented in terms of its suitability for inkjet printing. As part of this analysis, the inkjet printed active layer was employed to fabricate OPD devices with the same device stack used in the spin-coated references. Moreover, the devices containing the inkjet printed active layer were optimized in terms of their printing resolution with optimal conditions achieved at a dpi of 725.71, and yielding OPDs with a similar performance to their spin-coated counterparts.

Thereafter, the design and fabrication of two new device architectures was introduced aiming to expand the application of the new BHJ from opaque to semi-transparent devices. The architectures for semi-transparent devices yielded functional devices formed by OPD stacks where all layers show a high transmittance in the visible range. Their performance was significantly lower when compared to the opaque reference samples showing a f_{-3dB} of up to 174 kHz and a responsivity of up to 10 mA W^{-1} at -2 V. However, they benefit from a higher transmittance in the visible range while remaining competitive in the NIR range, making them suitable for see-through and NIR applications that could not be accomplished with the opaque samples. During this chapter, the different ink formulations, device architectures and fabrication processes of each technology were described. Moreover, the characterization of the different device architectures for OPDs were presented in terms of their figures of merit and the comparison between each technology was dis-

cussed. Finally, the promising features of the developed devices were presented by performing PPG measurements as a practical demonstration.

The results presented in this chapter demonstrate the successful development of a new ink formulation suitable for inkjet printing as well as the successful implementation of the new BHJ system PIF8-TAA:BTP-4Cl as an active layer in OPD devices. Due to the use of a digital printing technique, the findings from this chapter are expected to be able to undergo a faster adaptation into industrial applications. In particular, the OPDs with opaque architecture offer a high performance that features devices for NIR applications and high detection speeds. Additionally, the semi-transparent devices developed in this chapter are expected to enable new designs for health-monitoring devices which are particularly advantageous for wearable and on-body sensors and could be used to detect signals in a discrete and non-invasive manner.

8 Conclusion and Outlook

This thesis focuses on enabling the integration of organic photodiodes in multi-device systems in order to achieve novel functionalities as well as to facilitate their implementation in next-generation optoelectronic applications such as flexible photosensor matrices and light communication systems. This was carried out by developing new device architectures, exploring new ink formulations and seeking an optimal device performance, all while employing inkjet printing as the main fabrication method. This methodology aims to harness all the advantages of OPDs and allows to address different shortcomings. The challenge of developing high-performing OPDs with design flexibility and with the use of an industrially-relevant fabrication process is addressed by a novel and fully inkjet-printed OPD stack that is able to adapt to varied substrates, has a scalable fabrication process and which can be integrated in pre-defined systems while maintaining a high device performance. The joint operation of multiple OPDs with other electronic devices is approached by integrating OPDs with two different technologies of organic transistors to form all-organic photosensor matrices, including the first example of an OPD-OTFT photosensor matrix based on the technique of inkjet printing and without requiring patterning via optical or shadow masks. The development of more material systems aimed at NIR detection and developing new ink formulations suitable for inkjet-printed active layers is tackled simultaneously in terms of a novel material system which is successfully used to fabricate various OPD architectures. In addition to these major challenges, the work presented in this thesis also includes contributions to other relevant topics such as OPDs for optical wireless communication systems, semi-transparent OPDs and the use of mechanically flexible substrates.

In specific, in Chapter 5 the novel OPD stack composed by silver, SnO_2, P3HT:IDTBR, and PEDOT:PSS was developed in the mechanically flexible PEN substrate and yielded high-performing OPDs. The presented design features promising advantages such as high processing versatility, mechanical flexibility and high performance that makes them promising candidates to be implemented in sensor networks and other interconnected systems such as IoT and wearable electronics. The characterization of the devices showed high-performing OPDs with characteristics comparable to other advanced OPDs, and with a

particularly high competence in terms of responsivity and detection speed attaining SR values of 376 mA W^{-1} at -2 V as well as f_{-3dB} values of 2.1 MHz at -2 V. The fully-printed OPDs were also applied as receivers in a VLC system, in collaboration with the group of Prof. Stanislav Zvánovec from CTU in Prague, in order to assess their capabilities for practical applications in communication systems where the devices reached data rates of up to 20 Mb s^{-1}, and thus, demonstrated a performance suitable for practical applications such as data transfer from wearable sensors for health monitoring. Moreover, the comparison of the fully-printed devices to other OPDs containing the same active layer but based on spin-coated and partially-printed architectures demonstrated an equivalent performance that further corroborated their suitability in systems using wireless data exchange. In this regard, the findings obtained also represent a valuable contribution to the field of light communication where studies of VLC systems using high-performing OPDs as receivers is still uncommon.

Chapter 6 put into use the versatility of the OPD stack designed in Chapter 5 by investigating the integration of the fully inkjet-printed OPDs with two different matrices of organic transistors provided by two different project partners, the group of Prof. Sungjune Jung from POSTECH in South Korea, and InnovationLab GmbH in Germany. In each case the layout design, the substrate compatibility and the optimization of the printing process were addressed resulting in uniform and high-quality layers as well as high-performing devices. The analysis and optimization of different integrated devices showed that the tuning of the OPD size towards smaller active areas lowered the power consumption below the µW-range and directed the sensitivity of integrated devices towards higher values, achieving one of the largest values of sensitivity found in the literature for all-organic OPD-OTFT pairs. In addition to this, the potential suitability of the devices for real-life wearable applications was presented based on dynamic current measurements under alternating bending radiuses and varied illuminations, including PPG measurements using individual integrated devices as well as static and dynamic light sensing employing complete, 10×10, flexible matrices. Overall, Chapter 6 presents a process capable to integrate stacks of up to 10 functional layers and up to 1024 OPD-OTFT pairs based on the inkjet printing of OPDs. Additionally, both OPDs and OTFTs showed a high performance that remained unchanged despite undergoing the integration process.

Chapter 7 focuses on the development of a new BHJ system for NIR OPDs and its adaptation into an inkjet-printed process. The new BHJ system is developed using of the NFA known as BTP-4Cl which has NIR absorption; in combination with the donor and transparent polymer known as PIF8-TAA. This design combination yields a semi-transparent active layer that exhibits a high transmittance in the visible range together with an effective photoresponse focused in the NIR part of the spectrum. The chapter presents the successful development of the new ink formulation and its suitability for inkjet printing as well as the successful implementation of PIF8-TAA:BTP-4Cl as an active layer in OPD devices. Optimized devices containing inkjet-printed active layers yielded OPDs of high performance with an f_{-3dB} of up to 3 MHz and a responsivity of up to 58 mA W^{-1} at -2 V. Moreover, the design of new device architectures for semi-transparent devices yielded functional OPDs where all layers show a high transmittance in the visible range. In this case their performance was significantly lower when compared to the opaque reference samples showing a f_{-3dB} of up to 174 kHz and a responsivity of up to 10 mA W^{-1} at -2 V. However, the semi-transparent OPDs benefit from a higher transmittance in the visible range that makes them suitable for see-through and NIR applications that could not be accomplished with the opaque samples. Overall, the OPDs with opaque architecture offer a higher performance that features devices for NIR applications and high detection speeds while the semi-transparent devices possess specific features that have the potential to enable new designs for health-monitoring devices and which are particularly advantageous for wearable and on-body sensors where they could be used to detect signals in a discrete and non-invasive manner.

The common aim across the three presented chapters is the use of inkjet printing as the main fabrication technique while simultaneously seeking to maintain a high device performance. The premise is that by using an industrially-relevant and scalable deposition process, the findings achieved at a laboratory scale could be potentially transferred into mass-production levels without significant losses in performance and with a minimal adaptation of processing conditions. Therefore, this approach for OPD fabrication is also expected to allow a faster adaptation of laboratory findings to real-life applications as compared to non-scalable techniques that require a re-definition of their processing parameters in order to transfer the findings of OPD development into mass-production processes. At the same time, the work presented in this thesis demonstrates that, by exploiting the specific advantages of inkjet printing, this approach can enable invaluable

features such as fast device prototyping, increased substrate compatibility, customized designs, and a facilitated implementation of OPDs in real-life applications, particularly if a criterion of high-performing devices is maintained, as intended in this work.

Looking ahead, the concepts developed in this thesis can be expanded by a combination of the different areas and materials studied. The great potential and versatility of the OPDs introduced in Chapter 5 can be exploited further by its integration into more sophisticated applications like the combination of wearable health-monitoring devices and data transfer, and would also benefit from developing new encapsulation methods with higher mechanical flexibility. Additionally, the new material system presented in Chapter 7 could be used to develop matrices of photosensors such as those presented in Chapter 6 but formed by semi-transparent devices, in order to achieve spatial and multichannel detection of light with the advantages of see-through components. Similarly, such OPDs could be implemented into light communication systems for data exchange using NIR detection.

To conclude, it can be said with certainty, that based on the presented results in terms of OPD design, processability, performance and implementation in potential applications, the findings across all chapters of this thesis have the potential to facilitate the implementation of OPDs in the envisaged domains of IoT and wearable electronics and to inspire the development of new design methodologies and device architectures for innovative applications and which I hope can ultimately be of benefit for our society.

Appendix

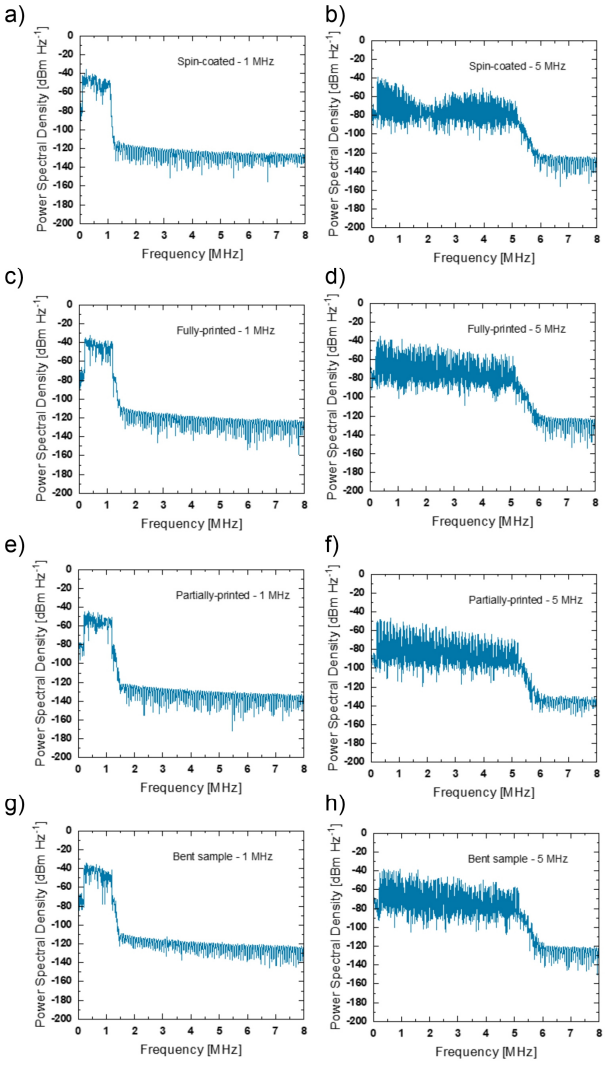

Figure A.1 Individual Spectrums Received During VLC Measurements.
Individual spectrums for the case of a) Spin-coated at 1MHz. b) Spin-coated at 5MHz. c) Fully-printed at 1MHz. d) Fully-printed at 5 MHz. e) Partially-printed at 1MHz. f) Partially-printed at 5MHz. g) Fully-printed bent sample at 1MHz. h) Fully-printed bent sample at 5MHz. The assembling of the VLC measurement setup and the processing of the VLC signals for data transmission was done by Dr. Petr Pešek and M.Sc. Carlos Guerra Yánez. The measurement of the individual spectrums shown here was done by M.Sc. Carlos Guerra Yánez. Figure adapted from[32], CC-BY.

Table A.1 Overview of contributions to experimental work. This overview of contributions relates to Sanghoon Baek (S.B.) and Luis Arturo Ruiz Preciado (L.A.R.P.) and corresponds to the experimental work presented in Section 6.2 of Chapter 6. Additional contributions by other authors are mentioned at the appropriate locations throughout the text.

Contribution by	Category	Details and comments
L.A.R.P. and S.B.	Methodology of integration	L.A.R.P. and S.B. discussed and worked together in the design of the integration layout used for the OPD-OTFT integration.
S.B.	OTFT devices	S.B. was in charge of the fabrication and characterization of the OTFT devices.
L.A.R.P.	OPD devices	L.A.R.P. was in charge of the fabrication and characterization of OPD devices.
L.A.R.P. and S.B.	Integrated devices	L.A.R.P. and S.B. characterized the integrated devices and performed the different demonstrations working together.

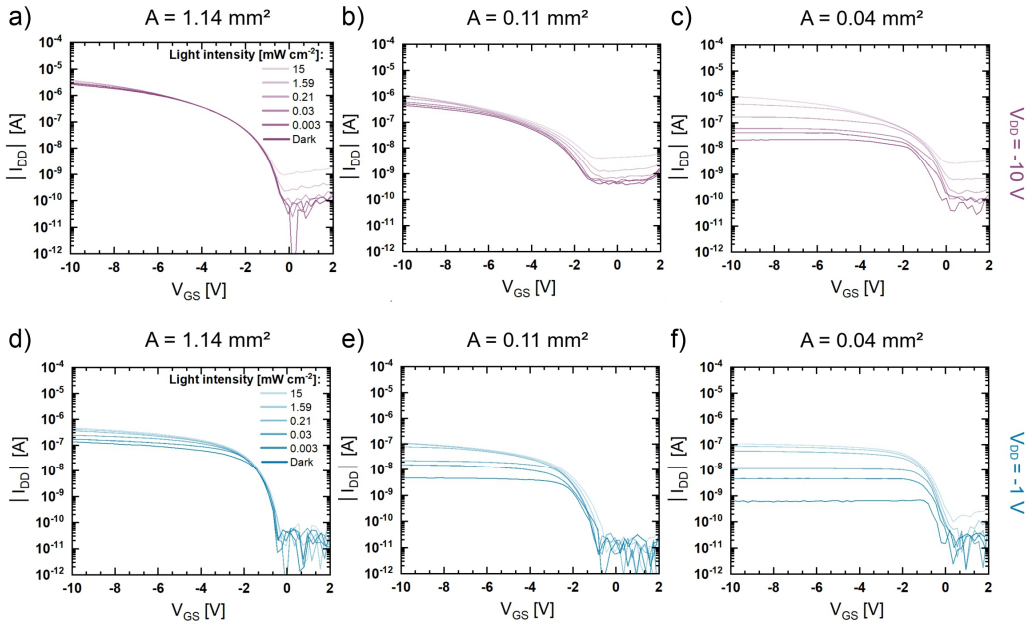

Figure A.2 Transfer Characteristics of OPD-OTFT Pairs with OPDs of Different Sizes.
Transfer characteristics of the integrated devices with a) OPD size= 1.14 mm² and V_{DD}= -10 V. b) OPD size= 0.11 mm² and V_{DD}= -10 V. c) OPD size= 0.04 mm² and V_{DD}= -10 V. d) OPD size= 1.14 mm² and V_{DD}= -1 V. e) OPD size= 0.11 mm² and V_{DD}= -1 V. f) OPD size= 0.04 mm² and V_{DD}= -1 V. Figure adapted from[13], CC-BY.

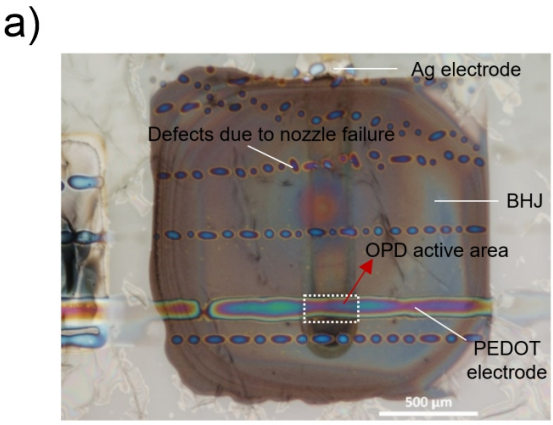

Figure A.3 Formation Issues in Small Electrodes.
a) Formation issues due to inhomogeneous wetting and defects caused by failure of nozzles. Inhomogeneous wetting during the printing deposition tended to have a more significant impact on the quality of the smaller electrodes resulting in formation issues. Figure taken from[13], CC-BY.

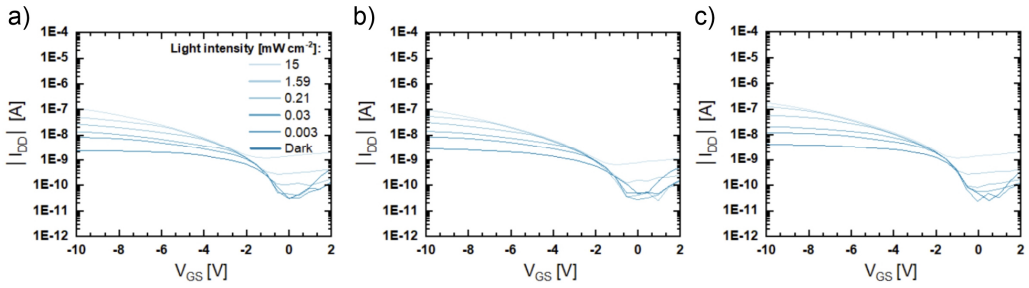

Figure A.4 Transfer Characteristics from Stability Tests.
Three different OPD-OTFT pairs with an OPD size of 0.11 mm² measured after one year and one month of storage in a glovebox environment. a) Pixel1. b) Pixel2. c) Pixel3. Figure adapted from[13], CC-BY.

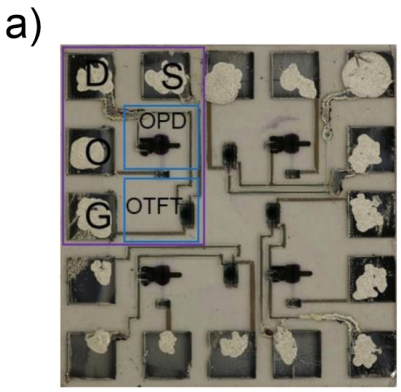

Figure A.5 Layout Design for OPD Characterization After OPD-OTFT Integration.
a) Photograph of sample with special layout design. The contact pads of the sample were designed based on the specifications of the sample-holder used in the required probe stations. Figure taken from[13], CC-BY.

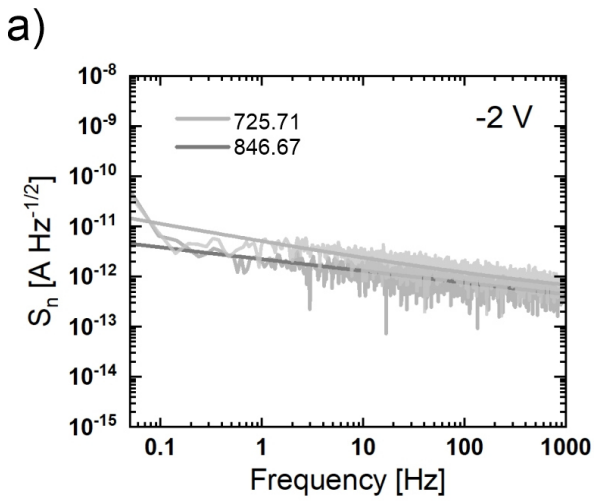

Figure A.6 Noise Measurements of OPDs with Inkjet-Printed PIF8-TAA:BTP-4Cl Active Layer at Different Printing Resolutions.
a) Spectral noise density at -2 V for samples with active layers deposited using a dpi of 725.71 and 846.67. A python module developed by Dr. Mervin Seiberlich was used to process the data of the spectral noise density and the specific detectivity.

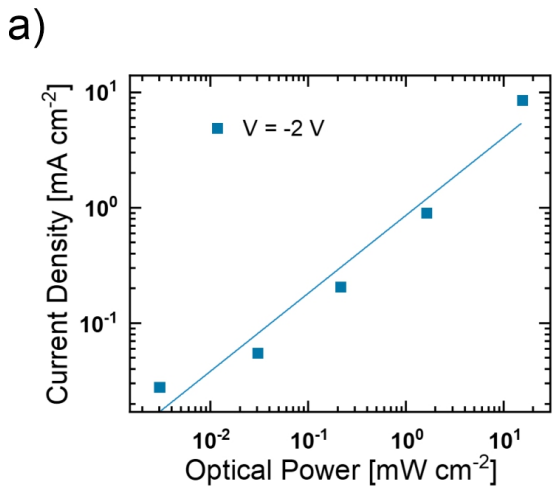

Figure A.7 LDR Measurement of Semi-Transparent Devices with PEDOT Electrode.
a) Current densities at different optical powers at -2 V. LDR= 66 dB.

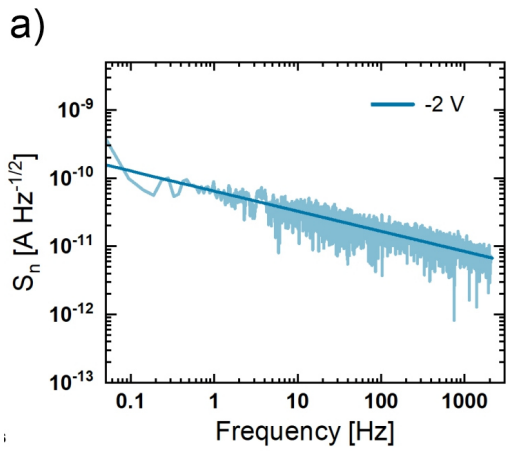

Figure A.8 Noise Measurements of Semi-Transparent Devices with PEDOT Electrode.
a) Spectral noise density at -2. A python module developed by Dr. Mervin Seiberlich was used to process the data of the spectral noise density and the specific detectivity.

References

1. Veendrick, H. *Bits on Chips*. (2018).
2. Yun, I. *Photodiodes - From Fundamentals to Applications*. (InTechOpen, 2012).
3. Nabet, B. *Photodetectors: Material, Devices and Applications*. (Elsevier-Woodhead, 2016).
4. Grand View Research. *Optical Sensors Market Size, Share & Trends Analysis Report 2024 - 2030*. https://www.grandviewresearch.com/industry-analysis/optical-sensors-market-report (accessed 2024).
5. Sekitani, T. & Someya, T. Stretchable, Large-area Organic Electronics. *Adv. Mater.* **22**, 2228–2246 (2010).
6. Khan, S., Lorenzelli, L. & Dahiya, R. S. Technologies for Printing Sensors and Electronics Over Large Flexible Substrates: A Review. *IEEE Sens. J.* **15**, 3164–3185 (2015).
7. Vega-Colado, C. *et al.* An All-Organic Flexible Visible Light Communication System. *Sensors* **18**, 3045 (2018).
8. Inzelberg, L. *et al.* Printed facial skin electrodes as sensors of emotional affect. *Flex. Print. Electron.* **3**, 045001 (2018).
9. Forrest, S. R. The path to ubiquitous and low-cost organic electronic appliances on plastic. *Nature* **428**, 911–918 (2004).
10. Xu, C., Liu, P., Feng, C., He, Z. & Cao, Y. Organic photodetectors with high detectivity for broadband detection covering UV-vis-NIR. *J. Mater. Chem. C* **10**, 5787–5796 (2022).
11. Lee, S.-H., Yusoff, A. R. B. M., Lee, C., Yoon, S. C. & Noh, Y.-Y. Toward color-selective printed organic photodetectors for high-resolution image sensors: From fundamentals to potential commercialization. *Mater. Sci. Eng. R Rep.* **147**, 100660 (2022).
12. Fuentes-Hernandez, C. *et al.* Large-area low-noise flexible organic photodiodes for detecting faint visible light. *Science* **370**, 698–701 (2020).
13. Ruiz-Preciado, L. A. *et al.* Monolithically printed all-organic flexible photosensor active matrix. *Npj Flex. Electron.* **7**, 6 (2023).
14. Strobel, N. *et al.* Color-Selective Printed Organic Photodiodes for Filterless Multichannel Visible Light Communication. *Adv. Mater.* **32**, 1908258 (2020).
15. Cho, S. *et al.* Small Molecule Based Organic Photo Signal Receiver for High-Speed Optical Wireless Communications. *Adv. Sci.* **9**, 2203715 (2022).
16. Shan, T., Hou, X., Yin, X. & Guo, X. Organic photodiodes: device engineering and applications. *Front. Optoelectron.* **15**, 49 (2022).

17. Wang, Y. *et al.* Narrowband organic photodetectors – towards miniaturized, spectroscopic sensing. *Mater. Horiz.* **9**, 220–251 (2022).

18. Tordera, D. *et al.* A High-Resolution Thin-Film Fingerprint Sensor Using a Printed Organic Photodetector. *Adv. Mater. Technol.* **4**, 1900651 (2019).

19. Simone, G. *et al.* High-Accuracy Photoplethysmography Array Using Near-Infrared Organic Photodiodes with Ultralow Dark Current. *Adv. Opt. Mater.* **8**, 1901989 (2020).

20. van Breemen, A. J. J. M. *et al.* Curved digital X-ray detectors. *Npj Flex. Electron.* **4**, 22 (2020).

21. Strobel, N., Seiberlich, M., Eckstein, R., Lemmer, U. & Hernandez-Sosa, G. Organic photodiodes: printing, coating, benchmarks, and applications. *Flex. Print. Electron.* **4**, 043001 (2019).

22. Salaoru, I., Maswoud, S. & Paul, S. Inkjet Printing of Functional Electronic Memory Cells: A Step Forward to Green Electronics. *Micromachines* **10**, (2019).

23. Lee, Y. *et al.* Reliable inkjet contact metallization on printed polymer semiconductors for fabricating staggered TFTs. *Appl. Phys. Lett.* **116**, 153301 (2020).

24. Kwon, J., Baek, S., Lee, Y., Tokito, S. & Jung, S. Layout-to-Bitmap Conversion and Design Rules for Inkjet-Printed Large-Scale Integrated Circuits. *Langmuir* **37**, 10692–10701 (2021).

25. Schlisske, S. *et al.* Surface energy patterning for ink-independent process optimization of inkjet-printed electronics. *Flex. Print. Electron.* **6**, 015002 (2021).

26. Olivier, S., Ishow, E., Della-Gatta, S. M. & Maindron, T. Inkjet deposition of a hole-transporting small molecule to realize a hybrid solution-evaporation green top-emitting OLED. *Org. Electron.* **49**, 24–32 (2017).

27. Merklein, L. *et al.* Comparative Study of Printed Multilayer OLED Fabrication through Slot Die Coating, Gravure and Inkjet Printing, and Their Combination. *Colloids Interfaces* **3**, 32 (2019).

28. Verma, A. *et al.* Efficient, inkjet-printed TADF-OLEDs with an ultra-soluble NHetPHOS complex. *Appl. Phys. A* **122**, 191 (2016).

29. Lindh, E. M., Sandström, A. & Edman, L. Printed Electronics: Inkjet Printed Bilayer Light-Emitting Electrochemical Cells for Display and Lighting Applications (Small 20/2014). *Small* **10**, 4147–4147 (2014).

30. Stolz, S. *et al.* Investigation of Solution-Processed Ultrathin Electron Injection Layers for Organic Light-Emitting Diodes. *ACS Appl. Mater. Interfaces* **6**, 6616–6622 (2014).

31. Zhou, L. *et al.* Inkjet-Printed Small-Molecule Organic Light-Emitting Diodes: Halogen-Free Inks, Printing Optimization, and Large-Area Patterning. *ACS Appl. Mater. Interfaces* **9**, 40533–40540 (2017).

32. Ruiz-Preciado, L. A. *et al.* Inkjet-printed high-performance and mechanically flexible organic photodiodes for optical wireless communication. *Sci. Rep.* **14**, 3296 (2024).
33. Gasparini, N. *et al.* Visible and Near-Infrared Imaging with Nonfullerene-Based Photodetectors. *Adv. Mater. Technol.* **3**, 1800104 (2018).
34. Strobel, N., Seiberlich, M., Rödlmeier, T., Lemmer, U. & Hernandez-Sosa, G. Non-Fullerene-Based Printed Organic Photodiodes with High Responsivity and Megahertz Detection Speed. *ACS Appl. Mater. Interfaces* **10**, 42733–42739 (2018).
35. Cesarini, M., Brigante, B., Caironi, M. & Natali, D. Reproducible, High Performance Fully Printed Photodiodes on Flexible Substrates through the Use of a Polyethylenimine Interlayer. *ACS Appl. Mater. Interfaces* **10**, 32380–32386 (2018).
36. Lilliu, S. *et al.* Inkjet-printed organic photodiodes. *Thin Solid Films* **520**, 610–615 (2011).
37. Grimoldi, A. *et al.* Inkjet printed polymeric electron blocking and surface energy modifying layer for low dark current organic photodetectors. *Org. Electron.* **36**, 29–34 (2016).
38. Azzellino, G. *et al.* Fully Inkjet-Printed Organic Photodetectors with High Quantum Yield. *Adv. Mater.* **25**, 6829–6833 (2013).
39. Saracco, E. *et al.* Work Function Tuning for High-Performance Solution-Processed Organic Photodetectors with Inverted Structure. *Adv. Mater.* **25**, 6534–6538 (2013).
40. Pace, G. *et al.* All-Organic and Fully-Printed Semitransparent Photodetectors Based on Narrow Bandgap Conjugated Molecules. *Adv. Mater.* **26**, 6773–6777 (2014).
41. Maiellaro, G. *et al.* Ambient Light Organic Sensor in a Printed Complementary Organic TFT Technology on Flexible Plastic Foil. *IEEE Trans. Circuits Syst. Regul. Pap.* **61**, 1036–1043 (2014).
42. Shu, Z., Kemper, F., Beckert, E., Eberhardt, R. & Tünnermann, A. Highly sensitive on-chip fluorescence sensor with integrated fully solution processed organic light sources and detectors. *RSC Adv.* **7**, 26384–26391 (2017).
43. Aga, R. S., Lombardi, J. P., Bartsch, C. M. & Heckman, E. M. Performance of a Printed Photodetector on a Paper Substrate. *IEEE Photonics Technol. Lett.* **26**, 305–308 (2014).
44. Falco, A., Salmerón, J., Loghin, F., Lugli, P. & Rivadeneyra, A. Fully Printed Flexible Single-Chip RFID Tag with Light Detection Capabilities. *Sensors* **17**, 534 (2017).
45. Wojciechowski, J. R. *et al.* Organic Photodiodes for Biosensor Miniaturization. *Anal. Chem.* **81**, 3455–3461 (2009).
46. Vanderspikken, J., Maes, W. & Vandewal, K. Wavelength-Selective Organic Photodetectors. *Adv. Funct. Mater.* **31**, 2104060 (2021).
47. Winkler, L. C., Kublitski, J., Benduhn, J. & Leo, K. Photomultiplication Enabling High-Performance Narrowband Near-Infrared Organic Photodetectors. *Adv. Electron. Mater.* **9**, 2201350 (2023).

48. Zhang, X., Jiang, J., Feng, B., Song, H. & Shen, L. Organic photodetectors: materials, device, and challenges. *J. Mater. Chem. C* **11**, 12453–12465 (2023).

49. Lan, Z., Lee, M.-H. & Zhu, F. Recent Advances in Solution-Processable Organic Photodetectors and Applications in Flexible Electronics. *Adv. Intell. Syst.* **4**, 2100167 (2022).

50. Ren, H., Chen, J., Li, Y. & Tang, J. Recent Progress in Organic Photodetectors and their Applications. *Adv. Sci.* **8**, 2002418 (2021).

51. Simone, G., Dyson, M. J., Meskers, S. C. J., Janssen, R. A. J. & Gelinck, G. H. Organic Photodetectors and their Application in Large Area and Flexible Image Sensors: The Role of Dark Current. *Adv. Funct. Mater.* **30**, 1904205 (2020).

52. Ma, X., Janssen, R. A. J. & Gelinck, G. H. Trap-Assisted Charge Generation and Recombination in State-of-the-Art Organic Photodetectors. *Adv. Mater. Technol.* **8**, 2300234 (2023).

53. Kublitski, J. *et al.* Reverse dark current in organic photodetectors and the major role of traps as source of noise. *Nat. Commun.* **12**, 551 (2021).

54. Armin, A. *et al.* Thick junction broadband organic photodiodes: Thick junction broadband organic photodiodes with extremely low dark current. *Laser Photonics Rev.* **8**, 924–932 (2014).

55. Biele, M. *et al.* Spray-Coated Organic Photodetectors and Image Sensors with Silicon-Like Performance. *Adv. Mater. Technol.* **4**, 1800158 (2019).

56. Simone, G. *et al.* On the Origin of Dark Current in Organic Photodiodes. *Adv. Opt. Mater.* **8**, 1901568 (2020).

57. Gielen, S. *et al.* Intrinsic Detectivity Limits of Organic Near-Infrared Photodetectors. *Adv. Mater.* **32**, 2003818 (2020).

58. Labanti, C. *et al.* Light-intensity-dependent photoresponse time of organic photodetectors and its molecular origin. *Nat. Commun.* **13**, 3745 (2022).

59. Pierre, A. & Arias, A. C. Solution-processed image sensors on flexible substrates. *Flex. Print. Electron.* **1**, 043001 (2016).

60. Haigh, P. A. *et al.* Organic visible light communications: Methods to achieve 10 Mb/s. in *2017 IEEE Photonics Conference (IPC)* vol. Orlando, FL, USA, 2017 553–554 (IEEE, Orlando, FL, USA, 2017).

61. Holliday, S. *et al.* High-efficiency and air-stable P3HT-based polymer solar cells with a new non-fullerene acceptor. *Nat. Commun.* **7**, 11585 (2016).

62. Baran, D. *et al.* Reducing the efficiency–stability–cost gap of organic photovoltaics with highly efficient and stable small molecule acceptor ternary solar cells. *Nat. Mater.* **16**, 363–369 (2017).

63. Gasparini, N. *et al.* Burn-in Free Nonfullerene-Based Organic Solar Cells. *Adv. Energy Mater.* **7**, 1700770 (2017).

64. Eynaud, Q. *et al.* Towards efficient NFA-based selective near-infrared organic photodetectors: impact of thermal annealing of polymer blends. *J Mater Chem C* **11**, 9657–9669 (2023).

65. Huang, Y.-C. *et al.* A promising non-fullerene acceptor for near-infrared organic photodetectors operating with low dark current and high response speed. *Chem. Eng. J.* **464**, 142633 (2023).

66. Zhang, Y., Lang, Y. & Li, G. Recent advances of non-fullerene organic solar cells: From materials and morphology to devices and applications. *EcoMat* **5**, e12281 (2023).

67. Köhler, A. & Bässler, H. *Electronic Processes in Organic Semiconductors.* (Wiley-VCH Verlag GmbH & Co. KGaA, 2015).

68. Nguyen, T.-P. *Defects in Organic Semiconductors and Devices*. (John Wiley & Sons, Inc, 2023).

69. Höher, P. A. *Visible Light Communications : Theoretical and Practical Foundations*. (Hanser, 2019).

70. Ghassemlooy, Z., Nero Alves, L., Zvanovec, S. & Khalighi, M. A. *Visible Light Communications: Theory and Applications*. (CRC Press, 2017).

71. Yang, D. & Ma, D. Development of Organic Semiconductor Photodetectors: From Mechanism to Applications. *Adv. Opt. Mater.* **7**, 1800522 (2019).

72. Strobel, N. Printed Organic Photodiodes with Enhanced Performance and Simplified Processing. (Karlsruher Institut für Technologie (KIT), 2020).

73. Ruiz Preciado, L. A. Power loss analysis and minimization of III-V PV cells via validated network simulation. (KU Leuven, 2019).

74. Wu, S. *et al.* High Sensitivity Polymer Visible-Near Infrared Photodetectors via an Inverted Device Structure and Manipulation of Injection Barrier Height. *Small* **12**, 3374–3380 (2016).

75. Seiberlich, M. *et al.* Aerosol-Jet-Printed Donor-Blocking Layer for Organic Photodiodes. *Adv. Electron. Mater.* **7**, 2000811 (2021).

76. Fang, Y., Armin, A., Meredith, P. & Huang, J. Accurate characterization of next-generation thin-film photodetectors. *Nat. Photonics* **13**, 1–4 (2019).

77. Maturová, K., van Bavel, S. S., Wienk, M. M., Janssen, R. A. J. & Kemerink, M. Description of the Morphology Dependent Charge Transport and Performance of Polymer:Fullerene Bulk Heterojunction Solar Cells. *Adv. Funct. Mater.* **21**, 261–269 (2011).

78. Street, R. A., Schoendorf, M., Roy, A. & Lee, J. H. Interface state recombination in organic solar cells. *Phys. Rev. B* **81**, 205307 (2010).

79. Yoon, S., Sim, K. M. & Chung, D. S. Prospects of colour selective organic photodiodes. *J Mater Chem C* **6**, 13084–13100 (2018).

80. Kato, K., Hata, S., Yoshida, J. & Kozen, A. Design of high-speed and high-sensitivity photodiode with an input optical waveguide on semi-insulating InP

substrate. in *LEOS 1992 Summer Topical Meeting Digest on Broadband Analog and Digital Optoelectronics, Optical Multiple Access Networks, Integrated Optoelectronics, and Smart Pixels* 254–257 (IEEE, Newport, RI, USA, 1992). doi:10.1109/ICIPRM.1992.235591.

81. Zaumseil, J. & Sirringhaus, H. Electron and Ambipolar Transport in Organic Field-Effect Transistors. *Chem. Rev.* **107**, 1296–1323 (2007).
82. Xu, Y. *et al.* Precise Extraction of Charge Carrier Mobility for Organic Transistors. *Adv. Funct. Mater.* **30**, 1904508 (2020).
83. Haigh, P. A. *et al.* Multi-band carrier-less amplitude and phase modulation for bandlimited visible light communications systems. *IEEE Wirel. Commun.* **22**, 46–53 (2015).
84. Pešek, P. *et al.* Experimental multi-user VLC system using non-orthogonal multi-band CAP modulation. *Opt. Express* **28**, 18241 (2020).
85. Derby, B. Inkjet Printing of Functional and Structural Materials: Fluid Property Requirements, Feature Stability, and Resolution. *Annual Review of Materials Research* vol. 40 395–414 (2010).
86. FUJIFILM Dimatix, Inc. Frequently Asked Questions Dimatix Materials Printer and Cartridge https://asset.fujifilm.com/www/de/files/2020-03/11aadfba9335c2dbd98041b0cb836cdf/FAQs_DMP-2800_Series_Printer_DMC-11600-Series-Cartriadge.pdf (accessed 2024). (2019).
87. Parvate, S., Dixit, P. & Chattopadhyay, S. Superhydrophobic Surfaces: Insights from Theory and Experiment. *J. Phys. Chem. B* **124**, 1323–1360 (2020).
88. Żenkiewicz, M. Methods for the calculation of surface free energy of solids. *J. Achiev. Mater. Manuf. Eng.* **24**, (2007).
89. CR. So You Want to Measure Surface Energy? Technical Note KRÜSS https://www.rheosense.com/hs-fs/hub/296746/file-2438655427-pdf/Application_Notes/VROC_-_Principle.pdf (accessed 2024). (1999).
90. Schlißke, S. Substratfunktionalisierungen zur Optimierung tintenstrahlgedruckter opto-elektronischer Bauteile. (Karlsruher Instituts für Technologie (KIT), 2021).
91. Rheosense. How VROC Works https://www.rheosense.com/hs-fs/hub/296746/file-2438655427-pdf/Application_Notes/VROC_-_Principle.pdf (accessed 2024).
92. Agilent. The Basics of UV-Vis Spectrophotometry https://www.agilent.com/cs/library/primers/public/primer-uv-vis-basics-5980-1397en-agilent.pdf (accessed 2024).
93. Yan, X., Wang, X., Gao, S. & Qiao, W. High-Performance Organic Photodetectors Using SnO_2 as Interfacial Layer with Optimal Thickness. *Phys. Status Solidi A* **220**, 2200667 (2023).
94. Krebsbach, P. *et al.* Inkjet-Printed Tin Oxide Hole-Blocking Layers for Organic Photodiodes. *ACS Appl. Electron. Mater.* **3**, 4959–4966 (2021).

95. Huang, J. *et al.* Understanding and Countering Illumination-Sensitive Dark Current: Toward Organic Photodetectors with Reliable High Detectivity. *ACS Nano* **15**, 1753–1763 (2021).

96. Clarke, A. J. *et al.* Non-fullerene acceptor photostability and its impact on organic solar cell lifetime. *Cell Rep. Phys. Sci.* **2**, 100498 (2021).

97. Li, W., Liu, D. & Wang, T. Stability Of Non-Fullerene Electron Acceptors and Their Photovoltaic Devices. *Adv. Funct. Mater.* **31**, 2104552 (2021).

98. Wang, Y. *et al.* Recent Progress and Challenges toward Highly Stable Nonfullerene Acceptor-Based Organic Solar Cells. *Adv. Energy Mater.* **11**, 2003002 (2021).

99. Lee, J. H. *et al.* Highly Conductive, Stretchable, and Transparent PEDOT:PSS Electrodes Fabricated with Triblock Copolymer Additives and Acid Treatment. *ACS Appl. Mater. Interfaces* **10**, 28027–28035 (2018).

100. Alemu, D., Wei, H.-Y., Ho, K.-C. & Chu, C.-W. Highly conductive PEDOT:PSS electrode by simple film treatment with methanol for ITO-free polymer solar cells. *Energy Env. Sci* **5**, 9662–9671 (2012).

101. Chakraborty, A. *et al.* Conductive organic electrodes for flexible electronic devices. *Sci. Rep.* **13**, 4125 (2023).

102. Dauzon, E. *et al.* Conducting and Stretchable PEDOT:PSS Electrodes: Role of Additives on Self-Assembly, Morphology, and Transport. *ACS Appl. Mater. Interfaces* **11**, 17570–17582 (2019).

103. Nie, S. *et al.* High Conductivity, Semiconducting, and Metallic PEDOT:PSS Electrode for All-Plastic Solar Cells. *Molecules* **28**, (2023).

104. Fan, X. *et al.* PEDOT:PSS for Flexible and Stretchable Electronics: Modifications, Strategies, and Applications. *Adv. Sci.* **6**, 1900813 (2019).

105. Cheng, T., Zhang, Y.-Z., Zhang, J.-D., Lai, W.-Y. & Huang, W. High-performance free-standing PEDOT:PSS electrodes for flexible and transparent all-solid-state supercapacitors. *J Mater Chem A* **4**, 10493–10499 (2016).

106. Li, Y., Chen, H. & Zhang, J. Carrier Blocking Layer Materials and Application in Organic Photodetectors. *Nanomaterials* **11**, (2021).

107. Pu, K. *et al.* A Flexible Sensitive Visible-NIR Organic Photodetector with High Durability. *Adv. Mater. Technol.* **8**, 2300207 (2023).

108. Huang, J. *et al.* Green-Solvent-Processed High-Performance Broadband Organic Photodetectors. *ACS Appl. Mater. Interfaces* **15**, 37748–37755 (2023).

109. Sung, M. J., Yoon, S., Kwon, S.-K., Kim, Y.-H. & Chung, D. S. Synthesis of Phenanthro[1,10,9,8- *cdefg*]carbazole-Based Conjugated Polymers for Green-Selective Organic Photodiodes. *ACS Appl. Mater. Interfaces* **8**, 31172–31178 (2016).

110. Byeon, H. *et al.* Flexible Organic Photodetectors with Mechanically Robust Zinc Oxide Nanoparticle Thin Films. *ACS Appl. Mater. Interfaces* **15**, 10926–10935 (2023).

111. Liess, A. *et al.* Ultranarrow Bandwidth Organic Photodiodes by Exchange Narrowing in Merocyanine H- and J-Aggregate Excitonic Systems. *Adv. Funct. Mater.* **29**, 1805058 (2019).

112. Shafian, S. & Kim, K. Panchromatically Responsive Organic Photodiodes utilizing a Noninvasive Narrowband Color Electrode. *ACS Appl. Mater. Interfaces* **12**, 53012–53020 (2020).

113. Lan, Z. *et al.* Filter-Free Band-Selective Organic Photodetectors. *Adv. Opt. Mater.* **8**, 2001388 (2020).

114. García De Arquer, F. P., Armin, A., Meredith, P. & Sargent, E. H. Solution-processed semiconductors for next-generation photodetectors. *Nat. Rev. Mater.* **2**, 16100 (2017).

115. Armin, A. *et al.* Quantum Efficiency of Organic Solar Cells: Electro-Optical Cavity Considerations. *ACS Photonics* **1**, 173–181 (2014).

116. Armin, A., Jansen-van Vuuren, R. D., Kopidakis, N., Burn, P. L. & Meredith, P. Narrowband light detection via internal quantum efficiency manipulation of organic photodiodes. *Nat. Commun.* **6**, 6343 (2015).

117. Nickel, F. *et al.* Spatial mapping of photocurrents in organic solar cells comprising wedge-shaped absorber layers for an efficient material screening. *Sol. Energy Mater. Sol. Cells* **104**, 18–22 (2012).

118. Kadem, B. Y., Hassan, A. K. & Cranton, W. The effects of organic solvents and their co-solvents on the optical, structural, morphological of P3HT:PCBM organic solar cells. in *AIP Conference Proceedings* vol. 1758 020006-1-020006–9 (Beirut, Lebanon, 2016).

119. Yusli, M. N., Way Yun, T. & Sulaiman, K. Solvent effect on the thin film formation of polymeric solar cells. *Mater. Lett.* **63**, 2691–2694 (2009).

120. Liu, J., Zeng, S., Jing, P., Zhao, K. & Liang, Q. Investigating the effect of cosolvents on P3HT/O-IDTBR film-forming kinetics and film morphology. *J. Energy Chem.* **51**, 333–341 (2020).

121. Ghassemlooy, Z. *et al.* Visible light communications: 3.75 Mbits/s data rate with a 160 kHz bandwidth organic photodetector and artificial neural network equalization [Invited]. *Photonics Res.* **1**, 65 (2013).

122. Haigh, P. A. *et al.* A 1-Mb/s Visible Light Communications Link With Low Bandwidth Organic Components. *IEEE Photonics Technol. Lett.* **26**, 1295–1298 (2014).

123. Arredondo, B. *et al.* Visible Light Communication System Using an Organic Bulk Heterojunction Photodetector. *Sensors* **13**, 12266–12276 (2013).

124. Salamandra, L. *et al.* A comparative study of organic photodetectors based on P3HT and PTB7 polymers for visible light communication. *Org. Electron.* **81**, 105666 (2020).

125. Chow, C.-W. *et al.* Pre-Distortion Scheme to Enhance the Transmission Performance of Organic Photo-Detector (OPD) Based Visible Light Communication (VLC). *IEEE Access* **6**, 7625–7630 (2018).

126. Chen, H. *et al.* A 1.9Mbps OFDM-based all-organic visible light communication system. in *2016 IEEE International Conference on Communication Systems (ICCS)* vol. Shenzhen, China, 2016 1–6 (IEEE, Shenzhen, China, 2016).

127. Gardašević, G., Katzis, K., Bajić, D. & Berbakov, L. Emerging Wireless Sensor Networks and Internet of Things Technologies—Foundations of Smart Healthcare. *Sensors* **20**, 3619 (2020).

128. Nguyen, D. T., Park, S., Chae, Y. & Park, Y. VLC/OCC Hybrid Optical Wireless Systems for Versatile Indoor Applications. *IEEE Access* **7**, 22371–22376 (2019).

129. Aksu, H., Babun, L., Conti, M., Tolomei, G. & Uluagac, A. S. Advertising in the IoT Era: Vision and Challenges. *IEEE Commun. Mag.* **56**, 138–144 (2018).

130. Eynaud, Q. *et al.* Toward Air Stability of Efficient Filter-Free Band-Selective Organic Photodetectors Based on Bulk Heterojunction: Avoiding Environmental Degradation with Atomic Layer Deposition Encapsulation. *Adv. Energy Sustain. Res.* **5**, 2300262 (2024).

131. Tavakkolnia, I. *et al.* Organic photovoltaics for simultaneous energy harvesting and high-speed MIMO optical wireless communications. *Light Sci. Appl.* **10**, 41 (2021).

132. Haigh, P. A., Ghassemlooy, Z. & Papakonstantinou, I. 1.4-Mb/s White Organic LED Transmission System Using Discrete Multitone Modulation. *IEEE Photonics Technol. Lett.* **25**, 615–618 (2013).

133. Chaleshtori, Z. N., Zvanovec, S., Ghassemlooy, Z., Eldeeb, H. B. & Uysal, M. Coverage of a shopping mall with flexible OLED-based visible light communications. *Opt. Express* **28**, 10015 (2020).

134. Haigh, P. A., Ghassemlooy, Z., Rajbhandari, S. & Papakonstantinou, I. Visible light communications using organic light emitting diodes. *IEEE Commun. Mag.* **51**, 148–154 (2013).

135. Sajjad, M. T. *et al.* Fluorescent Red-Emitting BODIPY Oligofluorene Star-Shaped Molecules as a Color Converter Material for Visible Light Communications. *Adv. Opt. Mater.* **3**, 536–540 (2015).

136. Haigh, P. A., Ghassemlooy, Z., Papakonstantinou, I. & Le Minh, H. 2.7 Mb/s With a 93-kHz White Organic Light Emitting Diode and Real Time ANN Equalizer. *IEEE Photonics Technol. Lett.* **25**, 1687–1690 (2013).

137. Nazari Chaleshtori, Z., Burton, A., Zvanovec, S., Ghassemlooy, Z. & Chvojka, P. Comprehensive optical and electrical characterization and evaluation of organic light-emitting diodes for visible light communication. *Opt. Eng.* **59**, 1 (2020).

138. Eckstein, R. *et al.* Fully Digitally Printed Image Sensor Based on Organic Photodiodes. *Adv. Opt. Mater.* **6**, 1701108 (2018).

139. Takahashi, T. *et al.* Carbon Nanotube Active-Matrix Backplanes for Mechanically Flexible Visible Light and X-ray Imagers. *Nano Lett.* **13**, 5425–5430 (2013).

140. Lee, K. H. *et al.* An Almost Transparent Image Pixel with a Pentacene/ZnO Photodiode, a Pentacene Thin-Film Transistor, and a 6,13-Pentacenequinone Phosphor Layer. *Adv. Mater.* **23**, 1231–1236 (2011).

141. Someya, T. *et al.* Integration of organic FETs with organic photodiodes for a large area, flexible, and lightweight sheet image scanners. *IEEE Trans. Electron Devices* **52**, 2502–2511 (2005).

142. Gelinck, G. H. *et al.* X-ray imager using solution processed organic transistor arrays and bulk heterojunction photodiodes on thin, flexible plastic substrate. *Org. Electron.* **14**, 2602–2609 (2013).

143. Jia, X., Fuentes-Hernandez, C., Chou, W.-F. & Kippelen, B. Organic photodetector with built-in amplification for the detection of visible light with low optical power. *Org. Electron.* **90**, 106064 (2021).

144. Wang, H. *et al.* A Retina-Like Dual Band Organic Photosensor Array for Filter-Free Near-Infrared-to-Memory Operations. *Adv. Mater.* **29**, 1701772 (2017).

145. Nausieda, I. *et al.* An Organic Active-Matrix Imager. *IEEE Trans. Electron Devices* **55**, 527–532 (2008).

146. Jiang, Z. *et al.* Ultraflexible Integrated Organic Electronics for Ultrasensitive Photodetection. *Adv. Mater. Technol.* **6**, 2000956 (2021).

147. Park, J. H. *et al.* Photo-Stable Organic Thin-Film Transistor Utilizing a New Indolocarbazole Derivative for Image Pixel and Logic Applications. *Adv. Funct. Mater.* **24**, 1109–1116 (2014).

148. Lee, K. H. *et al.* Semi-transparent organic/inorganic hybrid photo-detector using pentacene/ZnO diode connected to pentacene transistor. *Org. Electron.* **12**, 1103–1107 (2011).

149. Wang, H. *et al.* Three-Component Integrated Ultrathin Organic Photosensors for Plastic Optoelectronics. *Adv. Mater.* **28**, 624–630 (2016).

150. Renshaw, C. K., Xu, X. & Forrest, S. R. A monolithically integrated organic photodetector and thin film transistor. *Org. Electron.* **11**, 175–178 (2010).

151. Tong, X. & Forrest, S. R. An integrated organic passive pixel sensor. *Org. Electron.* **12**, 1822–1825 (2011).

152. Prevot, P.-H., Alvares, D., Micolich, A., Lovell, N. & Ladouceur, F. An all-organic active pixel photosensor featuring ion-gel transistors. *J. Org. Semicond.* **3**, 8–13 (2015).

153. Jeong, S. W. *et al.* The vertically stacked organic sensor-transistor on a flexible substrate. *Appl. Phys. Lett.* **97**, 253309 (2010).

154. Swathi, K. & Narayan, K. S. Image pixel device using integrated organic electronic components. *Appl. Phys. Lett.* **109**, 193302 (2016).

155. Baek, S. *et al.* Spatiotemporal Measurement of Arterial Pulse Waves Enabled by Wearable Active-Matrix Pressure Sensor Arrays. *ACS Nano* **16**, 368–377 (2022).

156. Yoon, S., Ha, Y.-H., Kwon, S.-K., Kim, Y.-H. & Chung, D. S. Fabrication of High Performance, Narrowband Blue-Selective Polymer Photodiodes with Dialkoxynaphthalene-Based Conjugated Polymer. *ACS Photonics* **5**, 636–641 (2018).

157. Lyons, D. M. *et al.* Narrow band green organic photodiodes for imaging. *Org. Electron.* **15**, 2903–2911 (2014).

158. Meng, D. *et al.* Near-Infrared Materials: The Turning Point of Organic Photovoltaics. *Adv. Mater.* **34**, 2107330 (2022).

159. Yuan, J. *et al.* Enabling low voltage losses and high photocurrent in fullerene-free organic photovoltaics. *Nat. Commun.* **10**, 570 (2019).

160. Cui, Y. *et al.* Single-Junction Organic Photovoltaic Cell with 19% Efficiency. *Adv. Mater.* **33**, 2102420 (2021).

161. Cui, Y. *et al.* Single-Junction Organic Photovoltaic Cells with Approaching 18% Efficiency. *Adv. Mater.* **32**, 1908205 (2020).

162. Li, S., Li, C.-Z., Shi, M. & Chen, H. New Phase for Organic Solar Cell Research: Emergence of Y-Series Electron Acceptors and Their Perspectives. *ACS Energy Lett.* **5**, 1554–1567 (2020).

163. Liu, Q. *et al.* 18% Efficiency organic solar cells. *Sci. Bull.* **65**, 272–275 (2020).

164. Yuan, J. *et al.* Single-Junction Organic Solar Cell with over 15% Efficiency Using Fused-Ring Acceptor with Electron-Deficient Core. *Joule* **3**, 1140–1151 (2019).

165. Zhan, L. *et al.* Over 17% efficiency ternary organic solar cells enabled by two non-fullerene acceptors working in an alloy-like model. *Energy Env. Sci* **13**, 635–645 (2020).

166. Zhang, H. *et al.* Over 14% Efficiency in Organic Solar Cells Enabled by Chlorinated Nonfullerene Small-Molecule Acceptors. *Adv. Mater.* **30**, 1800613 (2018).

167. Wang, R. *et al.* Rational Tuning of Molecular Interaction and Energy Level Alignment Enables High-Performance Organic Photovoltaics. *Adv. Mater.* **31**, 1904215 (2019).

168. Cui, Y. *et al.* Over 16% efficiency organic photovoltaic cells enabled by a chlorinated acceptor with increased open-circuit voltages. *Nat. Commun.* **10**, 2515 (2019).

169. Pang, S. *et al.* Nonfused Nonfullerene Acceptors with an A–D–A′–D–A Framework and a Benzothiadiazole Core for High-Performance Organic Solar Cells. *ACS Appl. Mater. Interfaces* **12**, 16531–16540 (2020).

170. Yao, H. *et al.* Design, Synthesis, and Photovoltaic Characterization of a Small Molecular Acceptor with an Ultra-Narrow Band Gap. *Angew. Chem. Int. Ed.* **56**, 3045–3049 (2017).

171. Chen, Y., Zheng, Y., Jiang, Y., Fan, H. & Zhu, X. Carbon-Bridged 1,2-Bis(2-thienyl)ethylene: An Extremely Electron Rich Dithiophene Building Block Enabling Electron Acceptors with Absorption above 1000 nm for Highly Sensitive NIR Photodetectors. *J. Am. Chem. Soc.* **143**, 4281–4289 (2021).

172. Tang, Z. *et al.* Polymer:Fullerene Bimolecular Crystals for Near-Infrared Spectroscopic Photodetectors. *Adv. Mater.* **29**, 1702184 (2017).

173. Xing, S. *et al.* Miniaturized VIS-NIR Spectrometers Based on Narrowband and Tunable Transmission Cavity Organic Photodetectors with Ultrahigh Specific Detectivity above 1014 Jones. *Adv. Mater.* **33**, 2102967 (2021).

174. Yang, J. *et al.* Cavity-Enhanced Near-Infrared Organic Photodetectors Based on a Conjugated Polymer Containing [1,2,5]Selenadiazolo[3,4-c]Pyridine. *Chem. Mater.* **33**, 5147–5155 (2021).

175. Jiang, B.-H. *et al.* Highly Efficient Ternary Near-Infrared Organic Photodetectors for Biometric Monitoring. *ACS Appl. Mater. Interfaces* **15**, 10907–10917 (2023).

176. Simões, J., Dong, T. & Yang, Z. Non-Fullerene Acceptor Organic Photodetector for Skin-Conformable Photoplethysmography Applications. *Adv. Mater. Interfaces* **9**, 2101897 (2022).

177. Wei, Y. *et al.* Self-Powered Organic Photodetectors with High Detectivity for Near Infrared Light Detection Enabled by Dark Current Reduction. *Adv. Funct. Mater.* **31**, 2106326 (2021).

178. Huang, J. *et al.* A High-Performance Solution-Processed Organic Photodetector for Near-Infrared Sensing. *Adv. Mater.* **32**, 1906027 (2020).

179. Babics, M. *et al.* Non-fullerene-based organic photodetectors for infrared communication. *J Mater Chem C* **9**, 2375–2380 (2021).

180. Kim, D.-H. *et al.* A high performance semitransparent organic photodetector with green color selectivity. *Appl. Phys. Lett.* **105**, 213301 (2014).

181. Wang, X., Wang, H., Zhou, D., Jin, H. & Yu, J. Semitransparent indium-tin-oxide-free non-fullerene organic photodetectors with double-side ultraviolet selective responses. *Mater. Lett.* **230**, 289–292 (2018).

182. Hadiyanto, M. Y. *et al.* Transparent photodetectors with ultra-low dark current and high photoresponse for near-infrared detection. *Org. Electron.* **99**, 106356 (2021).

183. Yang, L. *et al.* Low-Cost Copper Electrode for High-Performance Panchromatic Multiplication-Type Organic Photodetectors with Optical Microcavity Effect. *Adv. Funct. Mater.* **32**, 2108839 (2022).

184. Zheng, L. *et al.* Ag Nanowires Embedded ZnO for Semitransparent Organic Solar Cells with 13.76% Efficiency and 19.09% Average Visible Transmittance. *J. Phys. Chem. C* **125**, 18623–18629 (2021).

185. Zhang, H. *et al.* Transparent Organic Photodetector using a Near-Infrared Absorbing Cyanine Dye. *Sci. Rep.* **5**, 9439 (2015).

186. Chang, S.-Y., Cheng, P., Li, G. & Yang, Y. Transparent Polymer Photovoltaics for Solar Energy Harvesting and Beyond. *Joule* **2**, 1039–1054 (2018).

187. Song, W. *et al.* Foldable Semitransparent Organic Solar Cells for Photovoltaic and Photosynthesis. *Adv. Energy Mater.* **10**, 2000136 (2020).

188. Simone, G. *et al.* Near-Infrared Tandem Organic Photodiodes for Future Application in Artificial Retinal Implants. *Adv. Mater.* **30**, 1804678 (2018).

189. Kamijo, T. *et al.* A touchless user interface based on a near-infrared-sensitive transparent optical imager. *Nat. Electron.* **6**, 451–461 (2023).

190. Pietsch, M. *et al.* Inkjet-printed polymer-based electrochromic and electrofluorochromic dual-mode displays. *J Mater Chem C* **7**, 7121–7127 (2019).

191. Zhang, W. *et al.* Systematic Improvement in Charge Carrier Mobility of Air Stable Triarylamine Copolymers. *J. Am. Chem. Soc.* **131**, 10814–10815 (2009).

192. Ryu, S. *et al.* Voltage output of efficient perovskite solar cells with high open-circuit voltage and fill factor. *Energy Env. Sci* **7**, 2614–2618 (2014).

193. Ding, N. *et al.* A novel approach for designing efficient broadband photodetectors expanding from deep ultraviolet to near infrared. *Light Sci. Appl.* **11**, 91 (2022).

194. Liu, L. *et al.* Chiral Non-Fullerene Acceptor Enriched Bulk Heterojunctions Enable High-Performance Near-Infrared Circularly Polarized Light Detection. *Small* **18**, 2202941 (2022).

195. Li, T. *et al.* Materials for Interfaces in Organic Solar Cells and Photodetectors. *ACS Appl. Mater. Interfaces* **12**, 3301–3326 (2020).

196. Meyer, J. *et al.* Transition Metal Oxides for Organic Electronics: Energetics, Device Physics and Applications. *Adv. Mater.* **24**, 5408–5427 (2012).

197. Greiner, M. T. *et al.* Universal energy-level alignment of molecules on metal oxides. *Nat. Mater.* **11**, 76–81 (2012).

198. Kotadiya, N. B. *et al.* Universal strategy for Ohmic hole injection into organic semiconductors with high ionization energies. *Nat. Mater.* **17**, 329–334 (2018).

199. Lu, J.-H. *et al.* High-Performance organic photodiodes for Blue-Light hazard detection. *Chem. Eng. J.* **437**, 135327 (2022).

200. Liu, G., Li, T., Zhan, X., Wu, H. & Cao, Y. High-Sensitivity Visible–Near Infrared Organic Photodetectors Based on Non-Fullerene Acceptors. *ACS Appl. Mater. Interfaces* **12**, 17769–17775 (2020).

201. Wang, Y. *et al.* Stacked Dual-Wavelength Near-Infrared Organic Photodetectors. *Adv. Opt. Mater.* **9**, 2001784 (2021).

202. Wang, B. *et al.* Molecular doping of near-infrared organic photodetectors for photoplethysmogram sensors. *J Mater Chem C* **9**, 3129–3135 (2021).

203. Eun, H. J. *et al.* Effective Dark Current Suppression for High-Detectivity Organic Near-Infrared Photodetectors Using a Non-Fullerene Acceptor. *ACS Appl. Mater. Interfaces* **13**, 11144–11150 (2021).

204. Wu, L. *et al.* Photomultiplication type near-infrared organic photodetectors with a mixed active layer. *Microw. Opt. Technol. Lett.* **63**, 714–718 (2021).

205. Xia, K., Li, Y., Wang, Y., Portilla, L. & Pecunia, V. Narrowband-Absorption-Type Organic Photodetectors for the Far-Red Range Based on Fullerene-Free Bulk Heterojunctions. *Adv. Opt. Mater.* **8**, 1902056 (2020).

206. Hassan, S. Z. *et al.* Molecular Engineering of a Donor–Acceptor Polymer To Realize Single Band Absorption toward a Red-Selective Thin-Film Organic Photodiode. *ACS Appl. Mater. Interfaces* **11**, 28106–28114 (2019).

207. Opoku, H. *et al.* Bis-Diketopyrrolopyrrole and Carbazole-Based Terpolymer for High Performance Organic Field-Effect Transistors and Infra-Red Photodiodes. *Macromol. Chem. Phys.* **220**, 1900287 (2019).

208. Kim, J. Y. *et al.* Versatile use of ZnO interlayer in hybrid solar cells for self-powered near infra-red photo-detecting application. *J. Alloys Compd.* **813**, 152202 (2020).

209. Kang, J. *et al.* High-Detectivity Green-Selective All-Polymer p–n Junction Photodetectors. *Adv. Opt. Mater.* **8**, 2001038 (2020).

210. Schembri, T. *et al.* Semitransparent Layers of Social Self-Sorting Merocyanine Dyes for Ultranarrow Bandwidth Organic Photodiodes. *Adv. Opt. Mater.* **9**, 2100213 (2021).

211. Kamijo, T., de Winter, S., Panditha, P. & Meulenkamp, E. Printed Copper Grid Transparent Conducting Electrodes for Organic Light-Emitting Diodes. *ACS Appl. Electron. Mater.* **4**, 698–706 (2022).

212. Song, M. *et al.* ITO-free highly bendable and efficient organic solar cells with Ag nanomesh/ZnO hybrid electrodes. *J Mater Chem A* **3**, 65–70 (2015).

213. Han, Y. *et al.* Efficiency above 12% for 1 cm2 Flexible Organic Solar Cells with Ag/Cu Grid Transparent Conducting Electrode. *Adv. Sci.* **6**, 1901490 (2019).

214. Mao, L. *et al.* Flexible silver grid/PEDOT:PSS hybrid electrodes for large area inverted polymer solar cells. *Nano Energy* **10**, 259–267 (2014).

215. Bellchambers, P., Varagnolo, S., Maltby, C. & Hatton, R. A. High-Performance Transparent Copper Grid Electrodes Fabricated by Microcontact Lithography for Organic Photovoltaics. *ACS Appl. Energy Mater.* **4**, 4150–4155 (2021).

216. van de Groep, J. *et al.* Large-area soft-imprinted nanowire networks as light trapping transparent conductors. *Sci. Rep.* **5**, 11414 (2015).

217. Jiang, Z. *et al.* Durable Ultraflexible Organic Photovoltaics with Novel Metal-Oxide-Free Cathode. *Adv. Funct. Mater.* **29**, 1808378 (2019).

218. Jiang, Z. *et al.* Reverse-Offset Printed Ultrathin Ag Mesh for Robust Conformal Transparent Electrodes for High-Performance Organic Photovoltaics. *Adv. Mater.* **30**, 1707526 (2018).

219. Shi, L. *et al.* High performance flexible organic photomultiplication photodetector based on an ultra-thin silver film transparent electrode. *Nanotechnology* **31**, 314001 (2020).

220. Kim, H., Lee, K.-T., Zhao, C., Guo, L. J. & Kanicki, J. Top illuminated organic photodetectors with dielectric/metal/dielectric transparent anode. *Org. Electron.* **20**, 103–111 (2015).

Acknowledgements

I would like to express my gratitude to everyone who has been part of this long journey and have contributed to my PhD experience.

First of all, I would like to thank my referees **Prof. Gerardo Hernandez-Sosa**, and **Prof. Martijn Kemerink** for evaluating my thesis.
A profound thank you to **Prof. Gerardo Hernandez-Sosa**, for the opportunity of pursuing my PhD in the first place; and above all, for the guidance, the feedback, for helping me to grow as a scientist, and for always being available for support in both scientific and personal matters.
I would also like to thank **Prof. Uli Lemmer** for his support to my enrollment as a PhD candidate, especially in the initial phase of my doctorate.

Thank you also to all my current and former colleagues from our research group: **Noah**, **Mervin**, **Martin**, **Marta**, **Manu**, **Stefan**, **Helge**, **Rainer, Nassima, Fabian**, **Sanghoon**, **Alex**, **Manuela, Frida**, **Gerardo**, **Irene**, **Johannes**, **Peter**, **Mikel**, **la Lía**, **Paria**, **Ozan**, **Ali**, **Srikanth**, **Kai**, and **Christian**, for the great working atmosphere, for the many scientific discussions and collaborative work, and for the many fun times we shared in the office, the laboratories as well as outside work. For the people that is still around, I would like to say thank you to **Ali** for the many baklavas that he brought and thanks to **Jana** as well for making them. Also thank you to **Kai** for always being in the mood for some nice photos. To **Mikel** for convincing me to not skip (most) gym days, and for the Basque/Castellano lessons. To **Lía** for keeping visiting us and for keeping Mikel sane. To **Peter** for the many lunch-lottery moments in Edeka and for always being willing to help. To **Srikanth** for the funny anecdotes and Indian food suggestions. To **Christian** for stopping recommending movies and for joining the Spanish-speaking group. To **Irene** and **Nassima** for the fun lunch conversations and the occasional Italian candies. To **Helge** for being an amazing office-mate. To **Ozan** for the nice basketball games that we definitely need to do more often and to **Gerardo** for the exchange of Mexican rocaletas and manguitos and for putting all these nice people together in the same lab.

Special thanks also go to **Noah** and **Mervin** for the great collaboration in the field of OPDs. I am truly thankful with both of you for your many teachings and patience at the beginning of my PhD. Another big thank you goes to **Stefan** for his insights into the world of inkjet printing. Similarly, I would like to thank **Sanghoon** and **Karl-Philipp** for our very fruitful collaboration during the OPD-OTFT matrix integration. I really enjoyed and I feel very fortunate for having worked with you. In this regard, I would also like to extend my gratitude to **the whole team in the 2HORISONS project** for the great collaboration and the many enriching project meetings, and particularly to those with whom I got to interact more often Sebastian Raths, Kai Exner, Robert Huber, Jasmin Aghassi, Palak Gupta, Nassima Amroun, Pariya Nazari, Rainer Bäuerle and Sebastian Stehlin. Similarly, I would also like to thank all **the colleagues from InnovationLab GmbH and FLEXOO GmbH** for their support in everyday work and for the enjoyable working atmosphere, particularly to Michael, Tanja, Janusz, and to those with whom I got to interact more often Thomas, Karl-Philipp, Jean-Nicolas, Florian, Yannick, Jenny, Benjamin, Manuel, Sebastian, Karsten, Thommy and Juliane.

I would like to thank **Prof. Sungjune Jung** from POSTECH for the fruitful collaborative work. I would also like to thank **Petr Pešek, Carlos Guerra-Yánez and Prof. Stanislav Zvánovec** from Czech Technical University as well as **Prof. Zabih Ghassemlooy** from Northumbria University for our fruitful collaborative work and the nice learning experience in Prague.

For their invaluable help with administrative procedures, I would like to thank **Nicole Klöfer, Astrid Henne, Claudia Holeisen, Christian Kayser, Julia Langhans, Jurana Hetterich, Anna Navickas**, and **Frank Urban** as well as the Karlsruhe House of Young Scientists (KHYS).

For financial support I would like to thank the German Academic Exchange Service (DAAD), the European Cooperation in Science & Technology (COST) as well as the Ministry of Education and Research (BMBF).

Thank you to **Kai, Mervin,** and **Peter** for proofreading sections of my thesis looking for inescapable grammar and format mistakes.

I would also like to thank my friends **Rohith, Mauricio, Kordy, Maike,** and **Nozomi**, for their friendship that goes long back before this PhD journey and for the many moments that we have shared. Also to **Leo** and **Irene** for the enjoyable pool matches and the Mexi-

can food expeditions, to **Masha** for the good laughs and for the very nice whatsapp updates, to **Andre** and **Catarina** for the nice wine and dinner evenings, and to **Juš** and **Petra** for all the fun and the nice new year celebrations. Thank you all for making the journey more enjoyable!

Of course a special thank you also to my family,

To **Endre**, **Eva**, **Balazs**, and **Matyas** for all the love that I have received from you. For the relaxing holiday times that were very helpful to turn-off the mind from work and for the many boardgame matches and all the good memories that we share.

También quiero darle las gracias de todo corazón a mi mamá, **Sandra** porque sin su apoyo y sacrificios simplemente no estaría aquí. También le doy las gracias a mis hermanos **Carlos, Marco, Gustavo,** y a **tía Beatriz** por su apoyo incondicional y su amor. Me gustaría que nos pudiesemos ver más seguido… y al mismo tiempo estoy agradecido porque a pesar de la larga distancia hemos logrado estar ahí en los momentos más duros y también en los más felices y siempre podemos contar el uno con el otro cuando más importa. Gracias por todo!

Last and certainly not least, my deepest and heartfelt thank you goes to my beloved wife, **Andrea**, who somehow has managed to be nothing but supportive during these years. During the heaviest periods, it was your love and encouragement that gave me the determination to keep going and I am not sure I would have made it without you.

Once again, thanks to all of you!